

# Quantification of Tissue Scattering Properties by Use of Fiber Optic Spectroscopy

Ute Alice Gamm

ISBN 978-90-8891-702-8

Cover design:	Proefschriftmaken.nl
Print and Lay Out by:	Proefschriftmaken.nl    Uitgeverij BOXPress
Published by:	Uitgeverij BOXPress, 's-Hertogenbosch

# Quantification of Tissue Scattering Properties by Use of Fiber Optic Spectroscopy

Kwantificatie van weefsel verstrooiingseigenschappen  
door gebruik van fiber optische spectroscopie

PROEFSCHRIFT

ter verkrijging van de graad van Doctor  
aan de Erasmus Universiteit Rotterdam,  
op gezag van de rector magnificus

Prof.dr. H.G. Schmidt

en volgens besluit van het College van Promoties.  
De openbare verdediging zal plaatsvinden  
op vrijdag 4 oktober 2013 om 9:30 uur

door

**Ute Alice Gamm**

geboren te Ludwigshafen, Duitsland



## PROMOTIECOMMISSIE

Promotor: Prof.dr.ir. H.J.M.C. Sterenborg

Overige leden: Prof.dr. W. Niessen

Prof.dr.ir. W. Steenbergen

Prof.dr. T.G. van Leeuwen

Copromotor: Dr. A. Amelink

The investigations presented in this thesis were performed at the Center for Optical Diagnostics and Therapy, Department of Radiation Oncology, Postgraduate School Molecular Medicine, Erasmus University Medical Center Rotterdam.

This research was sponsored by IOP Photonic Devices, project: HYMPACT.

The publication of this thesis was kindly sponsored by:

Erasmus MC, Ocean Optics, Avantes, Polysciences and Shimadzu.

## Contents

<b>Chapter 1</b>	Introduction	7
<b>Chapter 2</b>	Measurement of the reduced scattering coefficient of turbid media using single fiber reflectance spectroscopy	29
<b>Chapter 3</b>	Method to quantitatively estimate wavelength-dependent scattering properties from multi-diameter single fiber reflectance spectra measured in a turbid medium	53
<b>Chapter 4</b>	Measurement of tissue scattering properties using multi-diameter single fiber reflectance spectroscopy: <i>in silico</i> sensitivity analysis	63
<b>Chapter 5</b>	Quantification of the reduced scattering coefficient and phase function dependent parameter $\gamma$ of turbid media using multi-diameter single fiber reflectance (MDSFR) spectroscopy: experimental validation	87
<b>Chapter 6</b>	<i>In vivo</i> quantification of the scattering properties of tissue using multi-diameter single fiber reflectance spectroscopy	95
<b>Chapter 7</b>	Measurement of refractive index correlation function properties using fiber-optic reflectance spectroscopy: <i>in silico</i> proof of concept	113
<b>Chapter 8</b>	Discussion	127
<b>Chapter 9</b>	Summary	137
	Samenvatting	141
<b>Appendices</b>	Acknowledgements	144
	Curriculum vitae	146
	List of publications	147
	PhD Portfolio	149



# Chapter 1

## Introduction

## Optical Diagnostics for cancer detection

Globally, cancer is becoming a major health problem as advances in medicine continue to extend the life spans of our populations. In 2011 alone, there were an estimated 12.7 million new cancer cases diagnosed, 7.6 million cancer related deaths, and 28 million people living with cancer within 5 years of their initial diagnosis [1]. Cancer research is one of the main research topics in health sciences and EU funding alone amounts to 1.1 billion euro between 2007 and 2011 [2]. Survival rates are closely correlated with early diagnosis and research on the development and improvement of diagnostic methods is increasing. Common techniques to detect cancer are ultrasound (US), x-ray computed tomography (CT), magnetic resonant imaging (MRI), single-photon emission computed tomography (SPECT) and positron emission tomography (PET), which visualize areas inside the body with a detection threshold of approximately  $1 \text{ cm}^3$  for solid tumors [3].

Initial diagnosis is mostly followed by biopsy for histological confirmation. Biopsy can obviate the need for surgery in patients with benign lesions and staging of sentinel lymph nodes supports the decision on surgical procedures to be performed when a cancer is present. However, the procedure has limitations because only a finite amount of samples are taken and the percentage of nonconclusive or false negative samples is high. For example staging of sentinel lymph nodes in breast cancer [4] and lung cancer patients [5] showed false negative rates of up to 29% and 23%, respectively. US-guided biopsies of pancreas showed a false negative rate of 46% in the setting of pancreatitis [6] and 40% in the case of prostate cancer [7]. An incorporation of optical techniques into the biopsy procedures has the potential of improving these statistics. Optical methods allow localized measurements at the point of interest and deliver information about tissue physiology and morphology which can be used to evaluate the location where a biopsy is collected. Optical methods use light in the visible or near infrared (NIR) wavelength range which is harmless, they mostly do not require contrast agents which can cause discomfort or potential risk (e.g. radioactive tracers) to the patient and are very cost-efficient.

## Endogenous optical contrast

Optical contrast in tissue arises from a number of phenomena including fluorescence, scattering, absorption and vibrational and non-linear energy transfer; there are numerous methods that use these contrast methods to image and characterize tissue. One of the simplest and most fundamental ways to probe tissue optically is to illuminate the tissue with light and analyze the light that is reflected through imaging, spectroscopy, or both.



Contrast in the reflected light arises from light absorption and scattering, which are described below.

### ***Tissue absorption***

Light absorption is caused by an energy transfer to absorbing molecules, so called chromophores, and is dependent on the effective absorption cross section  $\sigma_a$  and the number density  $\rho_N$  of absorbing particles. Absorption is usually quantified through the absorption coefficient  $\mu_a$ :

$$\mu_a(\lambda) = \sigma_a(\lambda)\rho_N \quad [mm^{-1}]. \quad (1.1)$$

The attenuation of the intensity ( $I$ ) of light, traveling distance  $\langle L \rangle(\lambda)$  through an absorbing medium with the absorption coefficient  $\mu_a$  can be described by the Lambert-Beer law:

$$I(\lambda) = I_0(\lambda)e^{-\mu_a(\lambda)\langle L \rangle(\lambda)}, \quad (1.2)$$

where  $I_0$  is the intensity of the incident light. In the presence of more than one absorber, the contributions of the individual absorption coefficients  $\mu_a^i(\lambda)$  sum up to an effective absorption coefficient  $\mu_a^{eff}(\lambda) = \sum_i \mu_a^i(\lambda)$ . Spectroscopic methods, which probe a range of wavelengths, are able to quantify each individual absorber by separating the contributions of individual absorption coefficients over the wavelength range.

The main endogenous absorbers in biological tissue in the visible range are oxy- and deoxyhemoglobin, bilirubin, which is a breakdown product of hemoglobin, and  $\beta$ -carotene (Figure 1.1). In the NIR range, lipids and water provide additional absorption. In cancer, tumor growth is accompanied by neovascularization, resulting in a greater concentration of blood in these tissues. Additionally, the higher metabolic rate of tumor tissues results in a lower blood oxygen saturation [8, 9]. Therefore, optical methods that measure tissue absorption can quantify the concentration of tissue absorbers such as blood and detect the changes in tissue physiology that are associated with cancer [10, 11, 12, 13]. Contrast from optical absorption can also be useful in many other clinical applications, such as pulse oxymetry, quantification of bilirubin levels related to jaundice [14] or the detection of hypoxia in the bladder wall which contributes to bladder dysfunction [15].

### ***Light scattering in tissue***

Light scattering in tissue is caused by spatial fluctuations in the refractive index (RI) of the cellular components that occur on size scales ranging from a few nanometers to a few millimeters. Due to their higher molecular density, macromolecules like lipids,

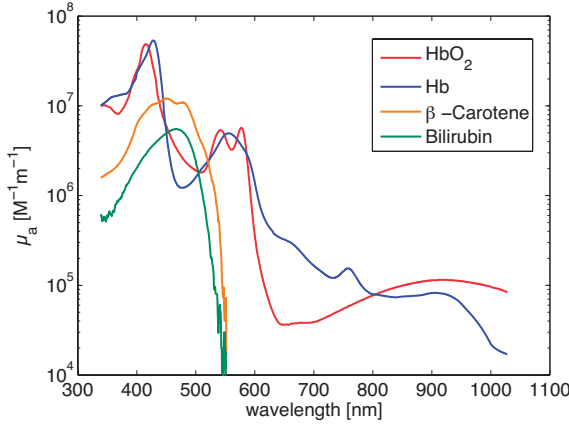


**Figure 1.1:** Absorption coefficients of the most important tissue chromophores: oxygenated hemoglobin, deoxygenated hemoglobin,  $\beta$ -carotene and bilirubin [5, 16, 17].

proteins and nucleic acids have a higher refractive index than the cytoplasm. Therefore, large organelles with folded bilipid membranes (*e.g.* mitochondria, Golgi apparatus and endoplasmic reticulum) and organelles with high protein content (*e.g.* peroxisomes and lysosomes) and the nucleus with its high concentration of nucleic acid, are highly scattering components of the cells [18, 19, 20]. The RI of a cell at position  $\mathbf{r}$  can be described by a simple relationship:

$$n(\mathbf{r}) = n_0 + \alpha\rho(\mathbf{r}), \quad (1.3)$$

where  $n_0$  is the refractive index of the surrounding medium (*e.g.* cytoplasm),  $\rho(\mathbf{r})$  is the fraction of solids and  $\alpha$  is the refractive index increment, which is dependent on the molecular density of the tissue components and has a typical value of  $\alpha \sim 0.17 - 0.2$  for tissue [31].

Similar to the absorption coefficient, light scattering can be described in an approximate way through the scattering coefficient, which is dependent on the number density of scattering particles  $\rho_N$  and the scattering cross section  $\sigma_s$ :

$$\mu_s(\lambda) = \sigma_s(\lambda)\rho_N \quad [mm^{-1}]. \quad (1.4)$$

Depending of the size of the scattering particles, scattering can fall into one of two regimes. Particles that are smaller than the wavelength of light can be characterized by Rayleigh scattering, which has no preferred direction of scattering and is therefore isotropic. Mie theory is capable of describing light scattering on spherical particles of all sizes [21, 22]; *i.e.* Mie theory is generally used for larger particles where the simpler Rayleigh theory is

no longer valid. The angular distribution of the scattered light is described by the phase function  $p(\theta, \phi)$ , which is the normalized form of the differential cross section  $d\sigma_s(\theta, \phi)/d\Omega$ .

$$p(\theta, \phi) = \frac{1}{\mu_s} \frac{d\sigma_s(\theta, \phi)}{d\Omega}. \quad (1.5)$$

Under the assumption that scattering is symmetric around the azimuthal angle,  $\phi$  can be neglected.

The phase function of media with a large distribution of different sized scattering particles can take complicated forms. The determination of the structural information encoded in the phase function would allow a complete characterization of the scattering properties of the medium. Unfortunately, reflectance spectroscopic measurements do not allow the determination of the complete phase function, because the collected light is scattered multiple times. However, as a simplification, the phase function can be expanded into a series of Legendre polynomials  $P_n(\theta)$ :

$$p(\cos(\theta)) = \sum_n (2n + 1) g_n P_n(\cos(\theta)). \quad (1.6)$$

In this expression,  $g_n$  is the  $n$ 'th moment of the phase function:

$$g_n = 2\pi \int_0^\pi P_n(\cos(\theta)) p(\cos(\theta)) d\cos(\theta). \quad (1.7)$$

The first moment  $g_1$  is called the anisotropy factor, and is a quantity that can be determined by reflectance spectroscopy. The anisotropy is the mean cosine of the scattering angle  $\langle \cos(\theta) \rangle$  and its value ranges from -1 to 1, where a value close to 1 indicates very forward directed scattering and a value of 0 means that there is no preferred scattering direction and scattering is therefore isotropic. Tissue scattering is predominantly forward directed and its anisotropy values are mostly found to be higher than 0.8 [23]. The anisotropy factor is also used to define the reduced scattering coefficient  $\mu'_s$  which combines the effect of the scattering coefficient and the average scattering angle to account for the longer effective distance between scattering events when scattering is in the forward direction:

$$\mu'_s = \mu_s (1 - g_1). \quad (1.8)$$

Similarly the second order moment can be used to define the phase function dependent parameter  $\gamma$  [24, 25]:

$$\gamma = \frac{1 - g_2}{1 - g_1}. \quad (1.9)$$

Similar to the anisotropy factor,  $\gamma$  is a metric of the scattering angle. It has been shown that for a fractal distribution of scattering particles  $\gamma$  is related to the fractal power of the size distribution of the scatterers [26]. Therefore,  $\gamma$  is hypothesized to contain information about tissue nanostructure, which is expected to change with the onset of cancer. The determination of  $\gamma$  could potentially be useful for optical diagnostics of early cancer.

### ***Types of scattering phase functions used for tissue***

Different models for the phase function for tissue have been suggested in the past and here we will briefly describe the most commonly used phase functions, which we also refer to in this thesis.

Tissue is often approximated by a distribution of spherical particles where its scattering properties as well as the scattering phase function can be calculated from Mie theory [21, 22]. A full description of its analytical formulation is beyond the scope of this thesis and can be found in the literature [21, 27]. Mie theory allows calculations of the optical properties of monodisperse sphere suspensions. For a suspension of different sized particles, a generalized form of the effective PF as a weighted sum of the individual phase functions from each sphere size was suggested by Gélébart *et al.* [28]:

$$P(\theta) = \frac{\sum_i \mu_{s,i} P(\theta)_i}{\sum_i \mu_{s,i}}. \quad (1.10)$$

Approximating tissue scattering properties with Mie theory, however, has to be treated cautiously because tissue contains more complicated structures than discrete individual spheres, which makes the utilization of Mie theory potentially inappropriate.

A commonly accepted model for a tissue phase function is the Henyey-Greenstein (HG) PF which was introduced by the two Astronomers L. G. Henyey and J. L. Greenstein in 1941 to describe the light scattering of interstellar dust particles [29]. It was found that this purely empirical PF describes light scattering in tissue reasonably well and also approximates angular scatter distributions calculated by Mie theory [30]. Due to its simple character, the HG phase function is one of the most frequently used phase functions:

$$p_{HG}(\theta) = \frac{1}{4\pi} \frac{1 - g_{HG}^2}{(1 + g_{HG}^2 - 2g_{HG} \cos(\theta))^{3/2}}. \quad (1.11)$$

Here, the  $n$ 'th moments of the phase function are pre-determined by  $g_n = g_{HG}^n$ . This, however, is a disadvantage because it has been shown that, for most tissues, higher order moments are different from those of the HG phase function [25, 31]. Also, the HG phase function is a monotonically decreasing function that lacks an increased probability for backscattering that has been reported for tissue [30]. Therefore a modified Henyey-

Greenstein phase function has been introduced by Bevilacqua and Depeursinge that incorporates an isotropic scattering term [24]:

$$p_{MHG}(\theta) = \alpha p_{HG}(\theta) + (1 - \alpha) \frac{3}{4\pi} \cos^2(\theta), \quad \alpha \in [0, 1]. \quad (1.12)$$

Where the weighing factor  $\alpha$  guarantees the normalization of  $p_{MHG}(\theta)$ .

Instead of treating tissue as a suspension of spherical particles, tissue can also be modeled as a continuous medium with random refractive index fluctuations. When tissue is considered as random continuous medium, analytical models can be derived to describe the angular distribution of scattered light [22, 32]. This interpretation of tissue scattering requires a model for the refractive index correlation function ( $B_n(r)$ ), which is then used to predict the scattering properties of the medium. Rogers *et al.* [33] introduced a very general model of the refractive index correlation function, which belongs to the family of Whittle-Matérn (WM) correlation functions:

$$B_n(r) = \Delta n^2 \frac{2^{5/2-m} \left(\frac{r}{l_c}\right)^{m-3/2}}{|\Gamma(m-3/2)|} K_{m-3/2} \left(\frac{r}{l_c}\right). \quad (1.13)$$

$l_c$  is the RI correlation length and the parameter  $m$  is a shape parameter. Dependent on the value of  $m$ , the function can take different shapes and therefore describes a broad variety of scattering theories, including the assumption of a fractal distribution of scattering sizes, which lead to a power law shape of the correlation function, and also to a tissue described by Henyey Greenstein phase function [33, 31]. The parameter  $m$  also defines the scattering form of the relation of the reduced scattering coefficient which is assumed to be  $\mu'_s = A\lambda^{2m-4}$ , for biologically relevant values of  $m > 1$ . The model assumes the Born approximation to be valid. In the Born approximation, the primary scattered wave created by the incident wave is the most prominent, and subsequent scattered waves can be neglected. This is the case when refractive index (RI) fluctuations are small, relative to the correlation length  $l_c$  [33]

$$\Delta n^2 (kl_c)^2 \ll 1 \quad (1.14)$$

where  $k$  is the wavenumber and  $\Delta n^2$  the variance in the refractive index. From the Whittle-Matérn correlation function, the WM-PF can be derived:

$$P(\theta) = \frac{k^6 l_c^6 (1 + 4k^2 l_c^2)^m (m-3)(m-2)m-1 (1 - 2k^2 l_c^2 (-1 + \cos(\theta)))^{-m} (3 + \cos(2\theta))}{((1 + 4k^2 l_c^2)^m (1 + 2k^2 l_c^2 (-1 + 2k^2 l_c^2 (m-2))(m-3))\pi - (1 + 4k^2 l_c^2)(1 + 2k^2 l_c^2 (1+m) + 4k^4 l_c^4 (4 + (m-3)m))\pi)}. \quad (1.15)$$

The WM model provides a link between optical properties like  $\mu'_s$  and the PF and the morphological features  $\Delta n$  and  $l_c$ , which enables spectroscopic measurements to provide information about tissue microstructure.

In early carcinogenesis, tissue undergoes nanoscale morphological and architectural changes that occur even before histological abnormalities become apparent. By characterizing the effects on light scattering, these changes may be detectable by optical methods [20, 34]. These changes may be present even away from the site of the lesion due to the field effect [35, 36], which could potentially enable the use of optical point measurements for screening [12].

### **Determination of optical properties by use of fiber optic reflectance spectroscopy**

The basic principle of steady-state reflectance spectroscopy is that light is delivered into a scattering and absorbing medium and the fraction of light that is reflected back is collected by a detector. Fiber optic reflectance spectroscopy uses optical fibers to deliver the light and detects the reflected spectrum which is then processed to extract the optical properties of the medium. Different approaches have been used to determine the optical properties and these methods highly depend on the geometry of the delivering and collecting fibers.

#### ***The radiative transport equation***

The propagation of an electromagnetic wave in a scattering medium can be described by the Boltzmann radiative transport equation, which describes the gradient of the radiance  $L$  at position  $\mathbf{r}$  in direction  $\hat{\mathbf{s}}$  [37]:

$$\frac{dL(\mathbf{r}, \hat{\mathbf{s}})}{ds} = -\mu_a L(\mathbf{r}, \hat{\mathbf{s}}) - \mu_s L(\mathbf{r}, \hat{\mathbf{s}}) + \mu_s \int_{4\pi} p(\mathbf{s}, \hat{\mathbf{s}}') L(\mathbf{r}, \hat{\mathbf{s}}') d\omega' + S(\mathbf{r}, \hat{\mathbf{s}}). \quad (1.16)$$

Losses caused by absorption and scattering are expressed in the first two terms. The third term, incorporating the tissue phase function  $p(\mathbf{s}, \hat{\mathbf{s}}')$  expresses a gain, caused by light that is scattered from all other directions  $\hat{\mathbf{s}}'$  into direction  $\hat{\mathbf{s}}$ . The term  $S(\mathbf{r}, \hat{\mathbf{s}})$  represents a source, *e.g.* fluorescent light generated within the tissue. The solution of the radiative transport equation (RTE) yields the tissue optical properties. Unfortunately, in many medical applications including fiber optic spectroscopy, the illumination and detection geometry induce boundary conditions that complicate or make the solution of the RTE impossible.

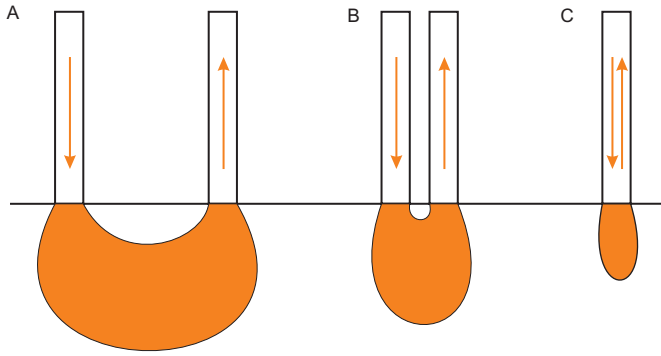


**Figure 1.2:** Probe design: A) large source-detector separation, B) small source-detector separation, C) single fiber probe

Generally there are three categories of fiber optic probe geometries: probes where there is a significant distance, usually a few millimeters up to a few centimeters, between the illumination fiber and the detection fiber, probes with a source-detector separation that is shorter than the transport mean free path (mfp), and single fiber probes that use the same optical fiber for illumination and detection (Figure 1.2).

#### ***Systems with large source-detector separation - Diffusion theory***

Systems with a large distance between illumination and detection fibers allow an approximate analytical solution of the RTE under certain boundary conditions. The diffusion approximation assumes that light propagation is insensitive to the tissue phase function and therefore does not have a preferential direction of travel but rather diffuses down a concentration gradient. The photon flux  $\mathbf{j}$  follows a relation similar to Fick's first law of diffusion [38, 39, 25, 40]

$$\mathbf{j}(\mathbf{r}, t) = -D\nabla\Phi(\mathbf{r}, t) \quad (1.17)$$

where  $D = (3[\mu_a + \mu'_s]^{-1})$  is the diffusion constant. Assuming that scattering dominates absorption, the fluence rate  $\Phi(\mathbf{r}, t)$  can be expressed by the diffusion equation [38]:

$$D\nabla^2\Phi(\mathbf{r}, t) - \mu_a\Phi(\mathbf{r}, t) = \frac{1}{c}\frac{\partial\Phi(\mathbf{r}, t)}{\partial t} - S(\mathbf{r}, t) \quad (1.18)$$

where  $S(\mathbf{r}, t)$  represents a source term.

Under specific, probe geometry dependent boundary conditions the diffusion equation yields solutions for the diffuse reflectance spectrum  $R(\rho, \mu'_s, \mu_a)$  as a function of the distance between source and detector fibers  $\rho$ , the reduced scattering coefficient  $\mu'_s$  and the absorption coefficient  $\mu_a$  and therefore allows the determination of these optical properties [41]. The diffusion approximation provides reasonable results down to source-

detector separations of one transport mean free path [42]. The optical properties are assumed to be homogeneous within the sampling volume. A disadvantage of systems with large source-detector separation is its insensitivity to the tissue phase function and therefore the inability to provide information about tissue structure. Also the size of the probe often only allows superficial measurements on skin or intraoperative measurements on exposed tissues [43, 44, 45, 46, 47]. These disadvantages can be avoided by using small source-detector separations.

### ***Systems with small source-detector separation -Methods to describe photon transport***

In systems where source and detector fibers are less than one transport mean free path apart, the majority of collected photons have undergone only few scattering events and light transport cannot exclusively be characterized by the reduced scattering coefficient  $\mu'_s$  but is also influenced by the scattering phase function [48, 30, 49, 42, 50]. The diffusion approximation as a solution of the RTE is not valid for such short source-detector separations and other approaches have to be used to solve the RTE and extract tissue optical properties. Those approaches can be computational or analytical.

#### ***Monte Carlo modeling of light transport***

Monte Carlo modeling is a computational method to obtain numerical results by repeated random sampling. One of the most widely used algorithms to describe photon propagation in turbid media is the MCML (Monte Carlo for multilayered media) code written by L. Wang [51]. In this algorithm, photon packets of unity weight are repeatedly launched and the likelihood of photon-medium interactions is determined by the user-specified optical properties of the medium and geometry of the measurement device. Step sizes are calculated based on a probability distribution related to the photon mean free path and the scattering angle is similarly calculated from the phase function of the medium. The weight of the packet is decreased by absorption events or by hitting a boundary where Fresnel's equations are used to calculate the loss of photon weight due to refractive index mismatch. Photons are terminated when they are scattered out of the medium or when the photon weight drops below a threshold. The MCML code tracks all interaction between photon packets and the medium, allowing a complete analysis of photon paths and therefore the reflectance signal collected by a specific probe geometry. From the reflectance signals for different optical properties an empirical model or a lookup-table can be created to enable correlation between measured reflectance and tissue optical properties.



### *Monte Carlo based approaches to determine tissue optical properties*

Reif *et al.* used Monte Carlo simulations to develop a simple analytical model to describe the reflectance of a scattering and absorbing medium for short source-detector separations for a tilted fiber geometry [52]. Experimental measurements were calibrated by use of a calibration phantom with known reflectance and the tissue optical properties  $\mu_a$  and  $\mu'_s$  could be determined from optical phantoms. However, the influence of the PF on the reflectance signal was acknowledged but not accounted for.

Bevilacqua *et al.* analyzed how the first two moments of the phase function, incorporated into the parameter  $\gamma = (1 - g_2)/(1 - g_1)$ , influence the Monte Carlo-simulated reflectance for source-detector separations close to one transport mean free path [24]. They showed that in order to predict the reflectance only four parameters are necessary: the refractive index, the absorption coefficient, the reduced scattering coefficient and  $\gamma$  and they suggested ways to determine the optical properties from empirical properties of the reflectance. The method was validated experimentally by taking measurements of several small source-detector separations (0.3 – 1 mm) on scattering phantoms and compared the results with frequency domain photon migration spectroscopy [53]. Alternatively Thueller *et al.* [26] created a lookup-table to extract tissue optical properties based on the findings from Bevilacqua *et al.* and *in vivo* measurements were performed on human brain and skull and in the gastrointestinal tract. Use of the two closest fibers with a distance of 0.3 mm, however, caused a systematic error and it is assumed here that even higher order moments of the phase function are required to match the theoretical and experimental results [53, 26]. Palmer *et al.* have developed a Monte Carlo-based forward and inverse model which performed well in the extraction of  $\mu_a$  and  $\mu'_s$  of phantoms containing absorbers and polystyrene spheres as scatterers [54]. Here Mie theory was used to inform the Monte Carlo simulations and it has not been elucidated how the model changes when different phase functions are used and how it performs on tissue where the phase function is more complicated.

Another approach was developed by Amelink *et al.* where the reflectance signal was sampled through the illuminating fiber as well as the adjacent collection fiber [55, 56]. By subtracting the signal of the collection fiber from the illuminating and collecting fiber, the photon pathlength becomes insensitive to the tissue optical properties [57]. The method, which is called differential pathlength spectroscopy (DPS), allows for reliable estimation of tissue absorption and has been used *in vivo* measurements frequently [58, 59, 60, 61]. However the method does not estimate scattering properties.

### *Analytical approaches to determine tissue optical properties*

A few analytical approaches have been introduced to describe reflectance close to the source. For example, Hull and Foster introduced the  $P_3$  approximation [25], which

is an analytical solution of the Boltzman transport equation similar to the diffusion approximation. Contrary to the diffusion approximation, the  $P_3$  approximation is valid for short source-detector separations because it incorporates the first three moments of the phase function. Expressions for the reflectance intensity were derived that allow the quantification of  $\mu_a$  and  $\mu'_s$ . However, this method uses assumptions for the higher order moments of the HG phase function which might have an impact on the estimation of the optical properties when a different phase function is present. Furthermore, the error in  $\mu_a$  increased for source-detector separations below 1 mm.

One recent publication compared six different models, including the  $P_n$  approximation and hybrid diffusion and  $P_3$  approximations for the determination of the optical properties close to the source and developed a joint derivation method of all models to overcome the limitations of the individual methods [62]. One limitation of this method is that initial guesses of the optical properties have to be made, which leads to the choice of forward model. This is a potential source of error, when the real optical properties lie in a range that the forward model is not suitable for.

A phase function-corrected diffusion approximation to describe spatially dependent diffuse reflectance close to the source was introduced by Vitkin *et al.* [63]. A two part expression was derived, which combines the diffusion approximation for a pencil beam with an approximation of the changes in reflectance due to the specific form of the phase function. Modeled reflectance intensities showed good agreement in comparison to MC simulations using HG and Mie PFs. However, in order to determine tissue optical properties an assumption of the PF has to be made.

Liemert *et al.* have solved the three dimensional RTE in an anisotropically scattering semi-infinite medium by applying a two-dimensional Fourier transform and the modified spherical harmonics method [64]. The reflectance signal obtained from the analytical solution showed good agreement with Monte Carlo simulated reflectance using the HG phase function for source-detector separations between 0 and 3 mm. It would be interesting to investigate how well the analytical solution correlates with MC simulations of different phase functions.

### ***Single fiber reflectance spectroscopy***

Single fiber geometries, where the same fiber is used for both illumination and detection of the reflected spectrum, offer the advantage of a simplistic setup and the most compact probe design possible. Small fiber diameters of 200  $\mu\text{m}$  even fit through the lumen of FNA needles, allowing interstitial measurements in a minimally invasive way [65, 5]. Additionally, a single fiber probes a very small volume; this has two advantages. One of the main drawbacks of diffuse reflectance spectroscopy is the large sampling volume, which

is assumed to be homogeneous. A small sampling volume, as probed by a single fiber, is more likely to be homogeneous. Furthermore, in some applications it is more suitable to probe only shallow depths in tissue. For example, 85% of premalignant lesions arise in the epithelium, which has a thickness of only a few hundred micrometers. As a result, probes that measure larger volumes are less sensitive to changes in these tissues [66]. As phase function sensitivity increases with decreasing source-detector separation, a single fiber geometry is likely to be most sensitive to the phase function and has an increased potential to probe microstructural features of tissue.

Single fiber reflectance spectroscopy, however, has not been investigated as extensively as reflectance methods with separate fibers for illumination and detection. Single fiber geometries have mainly been used for fluorescence measurements in tissue and fluorescent phantoms [67, 68, 69] and for particle size analysis [70, 71]. Bargo *et al.* investigated technical aspects of single fiber measurements and found that not only the numerical aperture (NA), but also the optical properties of the medium in contact with the fiber have an influence on the collection efficiency of a single fiber [72]. Another publication investigates specular reflections on the probe-medium interface and the sensitivity of the collected spectrum to misplacement of the fiber [73]. A sized fiber approach to determine  $\mu'_s$  by two single fiber measurements was proposed by Moffit and Prahl [74]. Here  $\mu'_s$  can be determined by mapping the reflectances for both fibers. However, the method was only tested on Monte Carlo simulated data and not validated experimentally. But most importantly, the study did not investigate the influence of the scattering phase function on the reflectance intensities and therefore the estimation of  $\mu'_s$ .

Given the limited amount of literature there is a clear need to further investigate the possibility for a quantitative determination of tissue optical properties by the use of single fiber reflectance spectroscopy. Our group has recently studied the effect of optical properties on the propagation of photons that are collected by a single fiber measurement. Based on Monte Carlo simulations an empirical model for the single fiber pathlength has been found which shows excellent agreement with experimental data. The pathlength model contains information of the optical properties in the form of  $\mu_a$  and  $\mu'_s$  and sensitivity to the phase function has been reported [75, 76]. The potential of this method has been shown by probing lymph node physiology *in vivo* during endoscopic ultrasound-guided fine needle aspiration [65, 5, 77] and as a complementary tool to diagnose cervical premalignancies [78].

## Objective

The objective of this thesis is to further improve single fiber reflectance spectroscopy towards a full quantification of all tissue optical properties, including scattering. This involves the investigation of the phase function dependence on the single fiber reflectance intensity and the development of an approach to quantitatively determine the tissue scattering properties  $\mu'_s$  and  $\gamma$ , which are directly related to tissue microstructure and may have diagnostic value.

## Outline of this Thesis

**Chapter 2** studies the relationship between the single fiber reflectance intensity and the fiber diameter, the reduced scattering coefficient and the phase function through the use of Monte Carlo simulations. An empirical model for the single fiber reflectance is presented as well as the design of a calibration method that scales the single fiber reflectance intensity onto an absolute scale. A method to quantify  $\mu'_s$  and the phase function dependent parameter  $\gamma$  from measurements in turbid media is discussed in **Chapter 3**. The method is based on multiple single fiber reflectance measurements (MDSFR) that inform the reflectance model found in **Chapter 2** to estimate  $\mu'_s$  and  $\gamma$ . **Chapter 4** assesses the limitations of the MDSFR method by investigating the sensitivity of the fitting procedure to the choice and range of fiber diameters used. In **Chapter 5** the MDSFR method is then experimentally validated on scattering phantoms containing a fractal distribution of polystyrene spheres as scatterers and Evans Blue as absorber. A fractal dimension of the sphere distribution is chosen such that the resulting Mie phase function matches a modified Henyey-Greenstein phase function. **Chapter 6** presents the first *in vivo* MDSFR measurements on superficially located tumors on the tongues of mice. In **Chapter 7** tissue is considered to be a random continuous medium and the feasibility of the MDSFR method is tested on an alternative set of MC simulation that use a Whittle-Matérn phase function. Using the Whittle-Matérn model, we investigate the potential to extract not only  $\mu'_s$  and  $\gamma$  but also the shape parameter of the refractive index correlation function  $m$  and the correlation length  $l_c$  from MDSFR measurements. **Chapter 8** discusses the current status of MDSFR and presents an outlook on future research.

## References

- [1] P Berzinec. Cancer epidemiology in Central and South Eastern European countries. *Croatian Medical Journal*, 52:478–487, 2011.
- [2] R Draghia-Akli. Coordination of Translational Cancer Research in Europe: Towards Evidence-Based Therapies and Care. Brussels, Belgium, 2012. Presentation at the Research Forum, EPAAC, ECCO.
- [3] J V Frangioni. New technologies for human cancer imaging. *Journal of Clinical Oncology*, 26(24):4012, 2008.
- [4] T Kim, A E Giuliano, and G H Lyman. Lymphatic mapping and sentinel lymph node biopsy in early-stage breast carcinoma: a metaanalysis. *Cancer*, 106(1):4–16, January 2006.
- [5] S C Kanick, C der Leest, J.G.J.V. Aerts, H C Hoogsteden, S Kaščáková, H J C M Sterenborg, and A Amelink. Integration of single-fiber reflectance spectroscopy into ultrasound-guided endoscopic lung cancer staging of mediastinal lymph nodes. *Journal of Biomedical Optics*, 15:17004, 2010.
- [6] R H Wilson, M Chandra, J Scheiman, D Simeone, B McKenna, J Purdy, and M-A Mycek. Optical spectroscopy detects histological hallmarks of pancreatic cancer. *Optics Express*, 17(20):17502–16, September 2009.
- [7] N Hata, M Jinzaki, D Kacher, R Cormak, D Gering, a Nabavi, S G Silverman, a V D’Amico, R Kikinis, F a Jolesz, and C M Tempany. MR imaging-guided prostate biopsy with surgical navigation software: device validation and feasibility. *Radiology*, 220(1):263–8, July 2001.
- [8] G Fontanini, S Vignati, L Boldrini, S Chiné, V Silvestri, M Lucchi, a Mussi, C a Angeletti, and G Bevilacqua. Vascular endothelial growth factor is associated with neovascularization and influences progression of non-small cell lung carcinoma. *Clinical cancer research : an official journal of the American Association for Cancer Research*, 3(6):861–5, June 1997.
- [9] J Pouysségur, F Dayan, and N M Mazure. Hypoxia signalling in cancer and approaches to enforce tumour regression. *Nature*, 441(7092):437–43, May 2006.
- [10] J Q Brown, L G Wilke, J Geradts, S A Kennedy, G M Palmer, and N Ramanujam. Quantitative optical spectroscopy: a robust tool for direct measurement of breast cancer vascular oxygenation and total hemoglobin content *in vivo*. *Cancer Research*, 69(7):2919–26, April 2009.
- [11] R X Xu and S P Pivoski. Diffuse optical imaging and spectroscopy for cancer. *Expert review of medical devices*, 4(1):83–95, January 2007.
- [12] V Backman and H K Roy. Light-scattering technologies for field carcinogenesis detection: a modality for endoscopic prescreening. *Gastroenterology*, 140(1):35–41, January 2011.
- [13] H K Roy, A Gomes, V Turzhitsky, M J Goldberg, J Rogers, S Ruderman, Ki L Young, A Kromine, R E Brand, M Jameel, P Vakil, N Hasabou, and V Backman. Spectroscopic microvascular blood detection from the endoscopically normal colonic mucosa: biomarker for neoplasia risk. *Gastroenterology*, 135(4):1069–78, October 2008.
- [14] N Bosschaart, J H Kok, A M Newsum, D M Ouweneel, R Mentink, T G van Leeuwen, and M C G Aalders. Limitations and opportunities of transcutaneous bilirubin measurements. *Pediatrics*, 129(4):689–94, April 2012.

- [15] J R Scheepe, A Amelink, B W D de Jong, K P Wolffenbuttel, and D J Kok. Changes in bladder wall blood oxygen saturation in the overactive obstructed bladder. *The Journal of urology*, 186(3):1128–33, September 2011.
- [16] A Amelink, T Christiaanse, and H J C M Sterenborg. Effect of hemoglobin extinction spectra on optical spectroscopic measurements of blood oxygen saturation. *Optics Letters*, 34(10):1525–1527, 2009.
- [17] S W van der Poll. Raman spectroscopy of atherosclerosis. PhD Thesis, University of Leiden, 2003.
- [18] A Wax and V Backman. *Biomedical Applications of Light Scattering*. McGraw-Hill Professional, 2009.
- [19] S Johnsen, E A Widder, and Others. The physical basis of transparency in biological tissue: ultrastructure and the minimization of light scattering. *Journal of Theoretical Biology*, 199(2):181–198, 1999.
- [20] P Pradhan, D Damania, H M Joshi, V Turzhitsky, H Subramanian, Hemant K Roy, A Taflove, V P Dravid, and V Backman. Quantification of nanoscale density fluctuations by electron microscopy: probing cellular alterations in early carcinogenesis. *Physical Biology*, 8(2):026012, April 2011.
- [21] G Mie. Contributions to the optics of turbid media, particularly of colloidal metal solutions.
- [22] A Wax and V Backman. *Biomedical Applications of Light Scattering*. McGraw-Hill Companies, Inc., 2010.
- [23] S L Jacques. Optical properties of biological tissues: a review. *Physics in Medicine and Biology*, 58(11):R37–61, June 2013.
- [24] F Bevilacqua and C Depeursinge. Monte Carlo study of diffuse reflectance at source–detector separations close to one transport mean free path. *Journal of the Optical Society of America A*, 16(12):2935–2945, 1999.
- [25] E L Hull and T H Foster. Steady-state reflectance spectroscopy in the P3 approximation. *Journal of the Optical Society of America A*, 18(3):584–599, 2001.
- [26] P Thueller, I Charvet, F Bevilacqua, M S Ghislain, G Ory, P Marquet, P Meda, B Vermeulen, and C Depeursinge. *In vivo* endoscopic tissue diagnostics based on spectroscopic absorption, scattering, and phase function properties. *Journal of Biomedical Optics*, 8:495, 2003.
- [27] C Mätzler. *MATLAB Functions for Mie Scattering and Absorption*, 2002.
- [28] B Gélébart, E Tinet, J M Tualle, and S Avrillier. Phase function simulation in tissue phantoms: a fractal approach. *Pure and Applied Optics: Journal of the European Optical Society Part A*, 5:377–388, 1996.
- [29] L G Henyey and J L Greenstein. Diffuse radiation in the Galaxy. *Astrophysical Journal*, 93:70–83, 1941.
- [30] J R Mourant, J Boyer, A H Hielscher, and I J Bigio. Influence of the scattering phase function on light transport measurements in turbid media performed with small source-detector separations. *Optics Letters*, 21(7):546–548, 1996.
- [31] V Turzhitsky, A J Radosevich, J D Rogers, N N Mutyal, and V Backman. Measurement of optical scattering properties with low-coherence enhanced backscattering spectroscopy. *Journal of Biomedical Optics*, 16:67007, 2011.
- [32] A Ishimaru. *Wave Propagation and Scattering in Random Media Vol. 2*. Academic Press, Inc., New York, 1978.

- [33] J D Rogers, I R Capolu, and V Backman. Nonscalar elastic light scattering from continuous random media in the Born approximation. *Optics Letters*, 34(12):1891–3, June 2009.
- [34] H Subramanian, P Pradhan, Y Liu, I R Capoglu, X Li, J D Rogers, A Heifetz, D Kunte, H K Roy, A Taflove, and V Backman. Optical methodology for detecting histologically unapparent nanoscale consequences of genetic alterations in biological cells. *Proceedings of the National Academy of Sciences of the United States of America*, 105(51):20118–23, December 2008.
- [35] H K Roy, V Turzhitsky, Y Kim, M J Goldberg, P Watson, J D Rogers, A J Gomes, A Kromine, R E Brand, M Jameel, A Bogovejic, P Pradhan, and V Backman. Association between rectal optical signatures and colonic neoplasia: potential applications for screening. *Cancer Research*, 69(10):4476–83, May 2009.
- [36] H K Roy, H Subramanian, D Damania, T A Hensing, W N Rom, H I Pass, D Ray, J D Rogers, A Bogojevic, M Shah, and Others. Optical Detection of Buccal Epithelial Nanoarchitectural Alterations in Patients Harboring Lung Cancer: Implications for Screening. *Cancer Research*, 2010.
- [37] A. J. Welch and M. J. C. van Gemert. *Optical-Thermal Response of Laser Irradiated Tissue*. Plenum press, New York, 1995.
- [38] R C Haskell, L O Svaasand, T T Tsay, T C Feng, M S McAdams, and B J Tromberg. Boundary conditions for the diffusion equation in radiative transfer. *Journal of the Optical Society of America A, Optics, image science, and vision*, 11(10):2727–41, October 1994.
- [39] S L Jacques and B W Pogue. Tutorial on diffuse light transport. *Journal of Biomedical Optics*, 13:41302, 2008.
- [40] T J Farrell, M S Patterson, and B Wilson. A diffusion theory model of spatially resolved, steady-state diffuse reflectance for the noninvasive determination of tissue optical properties *in vivo*. *Medical Physics*, 19(4):879–888, 1992.
- [41] A Kienle and M S Patterson. Improved solutions of the steady-state and the time-resolved diffusion equations for reflectance from a semi-infinite turbid medium. *Journal of the Optical Society of America A*, 14(1):246–254, 1997.
- [42] S. C. Kanick, V. Krishnaswamy, U. A. Gamm, H. J. C. M. Sterenborg, D. J. Robinson, A. Amelink, and B. W. Pogue. Scattering phase function spectrum makes reflectance spectrum measured from Intralipid phantoms and tissue sensitive to the device detection geometry. *Biomedical Optics Express*, 3(5):1086–100, May 2012.
- [43] R L P Van Veen, H J C M Sterenborg, A Marinelli, and M Menke-Pluymers. Intraoperatively assessed optical properties of malignant and healthy breast tissue used to determine the optimum wavelength of contrast for optical mammography. *Journal of Biomedical Optics*, 9:1129, 2004.
- [44] S H Chung, A E Cerussi, C Klifa, H M Baek, O Birgul, G Gulsen, S I Merritt, D Hsiang, and B J Tromberg. *In vivo* water state measurements in breast cancer using broadband diffuse optical spectroscopy. *Physics in Medicine and Biology*, 53:6713, 2008.
- [45] S-H Tseng, A Grant, and A J Durkin. *In vivo* determination of skin near-infrared optical properties using diffuse optical spectroscopy. *Journal of Biomedical Optics*, 13(1):014016, 2010.
- [46] G Zonios, J Bykowski, and N Kollias. Skin melanin, hemoglobin, and light scattering properties can be quantitatively assessed *in vivo* using diffuse reflectance spectroscopy. *Journal of Investigative Dermatology*, 117(6):1452–1457, 2001.

- [47] A Kim, M Roy, F Dadani, and B C Wilson. A fiberoptic reflectance probe with multiple source-collector separations to increase the dynamic range of derived tissue optical absorption and scattering coefficients. *Optics Express*, 18:5580–5594, 2010.
- [48] M Canpolat and J R Mourant. High-angle scattering events strongly affect light collection in clinically relevant measurement geometries for light transport through tissue. *Physics in Medicine and Biology*, 45:1127, 2000.
- [49] A Kienle, F K Forster, and R Hibst. Influence of the phase function on determination of the optical properties of biological tissue by spatially resolved reflectance. *Optics Letters*, 26(20):1571–1573, 2001.
- [50] H Tian, Y Liu, and L Wang. Influence of the third-order parameter on diffuse reflectance at small source-detector separations. *Optics Letters*, 31(7):933–935, 2006.
- [51] L Wang, S L Jacques, and L Zheng. MCML–Monte Carlo modeling of light transport in multi-layered tissues. *Computer Methods and Programs in Biomedicine*, 47(2):131–146, 1995.
- [52] R Reif, O A'Amar, and I J Bigio. Analytical model of light reflectance for extraction of the optical properties in small volumes of turbid media. *Applied Optics*, 46(29):7317–7328, 2007.
- [53] F Bevilacqua, D Piguet, P Marquet, J D Gross, B J Tromberg, and C Depeursinge. *In vivo* local determination of tissue optical properties: applications to human brain. *Applied Optics*, 38(22):4939–4950, 1999.
- [54] G M Palmer and N Ramanujam. Monte Carlo-based inverse model for calculating tissue optical properties. Part I: Theory and validation on synthetic phantoms. *Applied Optics*, 45(5):1062–1071, 2006.
- [55] A Amelink and H J C M Sterenborg. Measurement of the local optical properties of turbid media by differential path-length spectroscopy. *Applied Optics*, 43(15):3048–3054, 2004.
- [56] A Amelink, D J Robinson, and H J C M Sterenborg. Confidence intervals on fit parameters derived from optical reflectance spectroscopy measurements. *Journal of Biomedical Optics*, 13:54044, 2008.
- [57] S C Kanick, H J C M Sterenborg, and A Amelink. Empirical model description of photon path length for differential path length spectroscopy: combined effect of scattering and absorption. *Journal of Biomedical Optics*, 13(6):064042, 2008.
- [58] R L P van Veen, A Amelink, M Menke-Pluymers, C van der Pol, and H J C M Sterenborg. Optical biopsy of breast tissue using differential pathlength spectroscopy. *Physics in Medicine and Biology*, 50:2573–2581, 2005.
- [59] T A Middelburg, S C Kanick, E R M de Haas, H.J.C.M. Sterenborg, A Amelink, M.H.A.M. Neumann, and D J Robinson. Monitoring blood volume and saturation using superficial fibre optic reflectance spectroscopy during PDT of actinic keratosis. *Journal of Biophotonics*, 2011.
- [60] A Amelink, J Haringsma, and H J C M Sterenborg. Differential path-length spectroscopy: a tool for quantitative assessment of blood oxygen saturation in microvessels. *Gastrointestinal endoscopy*, 71(6):1100, May 2010.
- [61] A Amelink, J Haringsma, and H J C M Sterenborg. Noninvasive measurement of oxygen saturation of the microvascular blood in Barrett's dysplasia by use of optical spectroscopy. *Gastrointestinal endoscopy*, 70(1):1–6, July 2009.
- [62] Z Shi, Y Fan, H Zhao, and K Xu. Joint derivation method for determining optical properties based on steady-state spatially resolved diffuse reflectance measurement at small source-



- detector separations and large reduced albedo range: theory and simulation. *Journal of Biomedical Optics*, 17(6):067004, June 2012.
- [63] E Vitkin, V Turzhitsky, L Qiu, Li Guo, I Itzkan, E B Hanlon, and L T Perelman. Photon diffusion near the point-of-entry in anisotropically scattering turbid media. *Nature Communications*, 2:587, January 2011.
  - [64] A Liemert and A Kienle. Light transport in three-dimensional semi-infinite scattering media. *Journal of the Optical Society of America. A, Optics, image science, and vision*, 29(7):1475–81, July 2012.
  - [65] S C Kanick, C van der Leest, J Aerts, H J C M Sterenberg, and A Amelink. Incorporation of Single Fiber Reflectance Spectroscopy into Ultrasound-Guided Endoscopy (EUS-FNA) of Mediastinal Lymph Nodes. *Biomedical Optics*, 2010.
  - [66] K Sokolov, M Follen, and R Richards-Kortum. Optical spectroscopy for detection of neoplasia. *Current Opinion in Chemical Biology*, 6(5):651–8, October 2002.
  - [67] T J Pfefer, K T Schomacker, M N Ediger, and N S Nishioka. Light propagation in tissue during fluorescence spectroscopy with single-fiber probes. *IEEE Journal of Selected Topics in Quantum Electronics*, 7(6):1004–1012, 2001.
  - [68] K R Diamond, M S Patterson, and T J Farrell. Quantification of fluorophore concentration in tissue-simulating media by fluorescence measurements with a single optical fiber. *Applied Optics*, 42:2436–2442, 2003.
  - [69] H Stepp, T Beck, W Beyer, C Pfaller, M Schuppler, R Sroka, and R Baumgartner. Measurement of fluorophore concentration in turbid media by a single optical fiber. *Medical Laser Application*, 22(1):23–34, June 2007.
  - [70] A Amelink, M P L Bard, S A Burgers, and H J C M Sterenberg. Singlescattering spectroscopy for the endoscopic analysis of particle size in superficial layers of turbid media. *Applied Optics*, 42(19):4095–4101, 2003.
  - [71] M Canpolat and J R Mourant. Particle size analysis of turbid media with a single optical fiber in contact with the medium to deliver and detect white light. *Applied Optics*, 40(22):3792–3799, 2001.
  - [72] P R Bargo, S A Prahl, and S L Jacques. Collection efficiency of a single optical fiber in turbid media. *Applied Optics*, 42(16):3187–3197, 2003.
  - [73] T P Moffitt and S A Prahl. The specular reflection problem with a single fiber for emission and collection. In *Proc. SPIE: Saratov Fall Meeting*, 2002.
  - [74] T P Moffitt and S A Prahl. Determining the reduced scattering of skin *in vivo* using sized-fiber reflectometry. In *Society of Photo-Optical Instrumentation Engineers (SPIE) Conference Series*, volume 4613, pages 254–263, 2002.
  - [75] S C Kanick, H J C M Sterenberg, and A Amelink. Empirical model of the photon path length for a single fiber reflectance spectroscopy device. *Optics Express*, 17:860–871, 2009.
  - [76] S C Kanick, D J Robinson, H J C M Sterenberg, and A Amelink. Monte Carlo analysis of single fiber reflectance spectroscopy. *Physics in Medicine and Biology*, 54:6991–7008, 2009.
  - [77] S C Kanick, C van der Leest, R S Djamin, A M Janssens, H C Hoogsteden, H J C M Sterenberg, A Amelink, J G J V Aerts, and P D Md. Characterization of Mediastinal Lymph Node Physiology *In Vivo* by Optical Spectroscopy during Endoscopic Ultrasound-Guided Fine Needle Aspiration. *Journal of Thoracic Oncology*, 5(7):981–987, 2010.

- [78] S Hariri Tabrizi, S Mahmoud Reza Aghamiri, F Farzaneh, A Amelink, and H J C M Sterenborg. Single fiber reflectance spectroscopy on cervical premalignancies: the potential for reduction of the number of unnecessary biopsies. *Journal of Biomedical Optics*, 18(1):17002, January 2013.





# Chapter 2

## Measurement of the reduced scattering coefficient of turbid media using single fiber reflectance spectroscopy<sup>1</sup>

### Abstract

This paper presents a relationship between the intensity collected by a single fiber reflectance device ( $R_{SF}$ ) and the fiber diameter ( $d_{fib}$ ) and the reduced scattering coefficient ( $\mu'_s$ ) and phase function ( $p(\theta)$ ) of a turbid medium. Monte Carlo simulations are used to identify and model a relationship between  $R_{SF}$  and dimensionless scattering ( $\mu'_s d_{fib}$ ). For  $\mu'_s d_{fib} > 10$  we find that  $R_{SF}$  is insensitive to  $p(\theta)$ . A solid optical phantom is constructed with  $\mu'_s \approx 220 \text{ mm}^{-1}$  and is used to convert  $R_{SF}$  of any turbid medium to an absolute scale. This calibrated technique provides accurate estimates of  $\mu'_s$  over a wide range ( $[0.05-8] \text{ mm}^{-1}$ ) for a range of  $d_{fib}$  ( $[0.2-1] \text{ mm}$ ).

---

1 U. A. Gamm\*, S. C. Kanick\*, H. J. C. M. Sterenborg, D. J. Robinson, A. Amelink. **Measurement of the reduced scattering coefficient of turbid media using single fiber reflectance spectroscopy: fiber diameter and phase function dependence.** Biomed Opt Exp. 2:1687-1702 (2011) \* indicates both authors contributed equally.

## Introduction

Reflectance spectroscopy is widely used for noninvasive measurement of the tissue absorption and scattering coefficients, which can provide diagnostic information about tissue function and structure, respectively [1-9]. Scattering in tissue originates from spatial heterogeneities of the optical refractive index that occur on size scales ranging from a few nanometers to a few millimetres [9]. Scattering properties of tissue include the scattering coefficient ( $\mu_s$ ), which describes the mean free path between scattering events, and the scattering phase function ( $p(\theta)$ ), which describes the angular distribution of scattering events. These properties are often described in terms of the scattering anisotropy  $g$ , which is the expectation value for the cosine of the scattering angle  $g = \langle \cos(\theta) \rangle$ , and the reduced scattering coefficient  $\mu'_s = \mu_s (1 - g)$ , which is a description of the combined effect of scattering coefficient and average scattering angle. Reflectance spectroscopy measurements with large source-detector separations ( $\approx 10$  mean free paths [10]) can be modeled using diffusion theory, which utilizes  $\mu'_s$  to characterize the effect of scattering of reflectance. Diffuse measurements return information about bulk tissue properties, which is a limitation because many clinical diagnostic applications require more localized measurements [11-13]. Quantitative extraction of the absorption and reduced scattering coefficients from reflectance measurements with small source-detector separations is complicated because light transport in this non-diffuse regime, where collected photons may undergo few scattering events, is no longer dependent exclusively on  $\mu'_s$ , but is also sensitive to large angle back scattering events, a characteristic of the scattering phase function.

The influence of phase function on reflectance intensity measured close to the source has been described in the literature. For example, Mourant *et al.* [14] reported significant differences in the Monte Carlo simulated reflectance intensities for a small source-detector probe for different phase functions (Henyey- Greenstein vs. Mie) but with the same anisotropy. Kienle *et al.* [15] also reported large deviations in the calculation of  $\mu_a$  and  $\mu'_s$  after simulating the reflectances for a source-detector separation of  $< 1$  mm for multiple phase functions by applying a standard solution for the diffusion equation [10] to extract the optical properties. Bevilacqua and Depeursinge [16, 17] systematically investigated the influence of higher order moments of the phase functions for several source-detector separations on the reflectance intensities. They introduced a phase function dependent coefficient  $\gamma$  which, together with  $\mu_a$  and  $\mu'_s$  and refractive index  $n$ , would give a complete description of the reflectance for systems with measurements from multiple short source-detector separations. Hull and Foster later developed an analytical description of light transport termed the  $P_3$  approximation, which models both diffuse and non-diffuse light scattering by including the first three

moments of the phase function [18]; this approach has been shown to be valid for source-detector separations as low as  $\approx 0.5$  mm [13], but not directly applicable for devices with overlapping source and detector locations. Other empirical investigations of the relationship between reflectance intensity with small source-detector separations and  $\mu'_s$  [19-21] did not fully characterize the effect of phase function on the collected signal.

Recently, our group reported on the use of experimentally validated Monte Carlo (MC) simulations to investigate the effect that optical properties have on the propagation of photons that are collected during a single fiber reflectance (SFR) measurement [22]. SFR spectroscopy uses a single fiber for the delivery and detection of light; a schematic of the device setup is shown in Figure 2.1. The advantages of an SFR device are the simplicity of the setup machinery and the small dimensions of the fiber-optic probes, which allows *e.g.* measurement through the lumen of FNA-needles [23, 24]. In the past, single fiber geometries have been used for the investigation of fluorescence in tissue and tissue simulation phantoms [25-28] and for particle size analysis [29,30]. The relationship between single fiber reflectance intensity and optical properties was studied by Moffit and Prahl [31]; however, their analysis did not yield quantitative estimates of  $\mu'_s$  or characterize phase-function dependence of the signal. Further studies have focused on technical aspects of single fiber reflectance, such as the need to remove internal specular reflections from the collected signal [32] and the dependence of the collection efficiency of a single fiber on the optical properties of the sampled medium [33]. Our previous work has focused on utilizing SFR spectroscopy to quantitate the absorption coefficient ( $\mu_a$ ), and the corresponding chromophore concentrations, in turbid media. These studies introduced an empirical function that describes the dependence of the effective photon path length [22,34] on the optical properties of the sampled medium. A limitation of our method is that the path length relation requires knowledge of  $\mu'_s$ , a parameter that is currently not quantitatively extracted from the measured spectra. The current spectral analysis algorithm uses estimated values for the wavelength-dependent  $\mu'_s$  and the uncertainty introduced has been documented [23]. A quantitative measurement of  $\mu'_s$  would improve the accuracy of our chromophore concentration estimates. Moreover, quantitative measurement of  $\mu'_s$  using an SFR device is inherently useful, because it may provide information about the tissue microarchitecture [9]; information that is complementary to the physiological information extracted from  $\mu_a$ , and may have diagnostic value. Additionally, quantitative knowledge of  $\mu'_s$  and  $\mu_a$  extracted from SFR measurements may be used to correct for the effect of optical properties on single fiber fluorescence measurements [25-28].

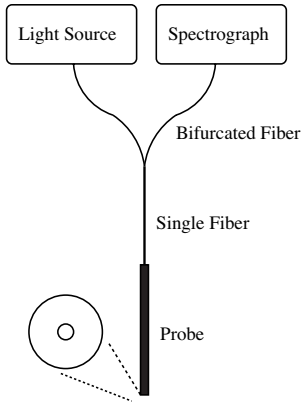


**Figure 2.1:** Schematic of single fiber reflectance probe machinery.

There are two challenges associated with quantitative extraction of  $\mu'_s$  from an SFR measurement. First, a calibration procedure must be designed that allows absolute measurement of the reflectance ( $R_{SF}$ ) of a turbid medium from an SFR measurement. Second,  $R_{SF}$  must be related to  $\mu'_s$ . The first challenge will be addressed by designing a calibration phantom that returns a known percentage of incident light during measurement. This measurement allows the scaling of reflectance intensity measured on a turbid medium to a percentage of the absolute amount of incident measurement light. Although the concept of using calibration phantoms to scale the reflectance is not novel, for an SFR device (or any other small source-detector separation device) the scattering phase function of the calibration phantom is a critical factor that needs to be accounted for in the design of the phantom; the present study considers phase function effects in detail. The second challenge is addressed by investigating the relationship between  $R_{SF}$  and the scattering properties of the medium, and the influence of scattering phase function using an extensive set of Monte Carlo simulations. The simulations are experimentally validated using highly scattering ( $\mu'_s \approx 20 - 200 \text{ mm}^{-1}$ ) solid phantoms consisting of titanium dioxide ( $\text{TiO}_2$ ) suspended in silicone, as well as low and medium scattering ( $0.05 < \mu'_s < 8 \text{ mm}^{-1}$ ) liquid phantoms consisting of a range of dilutions of Intralipid. An empirical model is introduced that describes the relation between  $R_{SF}$  and dimensionless scattering ( $\mu'_s d_{fib}$ ) for a wide range of phase functions.

Our methodology to experimentally extract  $\mu'_s$  of a turbid medium from SFR spectra, using a calibration phantom and an empirical model of  $R_{SF} = f(\mu'_s d_{fib})$ , is validated using SFR measurements on Intralipid phantoms. We show that with knowledge of the wavelength-dependent phase function, the empirical model function can be used to accurately extract  $\mu'_s$  from SFR measurements for a wide range of reduced scattering coefficients ( $\mu'_s = [0.05 - 8] \text{ mm}^{-1}$ ) and fiber diameters ( $d_{fib} = [0.2, 0.4, 0.6, 0.8, 1] \text{ mm}$ ).



## Materials and methods

### Monte Carlo simulation

The Monte Carlo (MC) code used to simulate single fiber reflectance spectroscopy in this study has been described in detail previously [22]. In short, our MC code is based on the MCML code [35] that stochastically simulates photon propagation within a turbid medium. During photon propagation, each photon step size was selected from an exponential distribution weighted by the scattering coefficient, and each scattering angle was selected from a user-specified phase function. Reflection and refraction due to the index of refraction mismatch at the medium/fiber and medium/air interface were calculated using the Fresnel equations and Snell's law. The index of refraction ( $n$ ) of the medium and fiber were specified at 1.37 and 1.5, respectively. The numerical aperture (NA) of the fiber was set as 0.22. Photons were initialized by selecting a location from a uniform distribution on the single fiber face in contact with the turbid medium ( $z = 0$ ), and the launch direction was selected from a uniform distribution of angles within the fiber cone of acceptance, where the acceptance angle was given as  $\Theta_a = \text{asin}(\frac{NA}{n_{\text{medium}}})$ . For photons propagating within the turbid medium that cross the medium interfacial boundary at  $z = 0$ , it was checked if they hit the fiber face; those in contact with the fiber face and traveling at an angle within the fiber cone of acceptance were collected, the rest were terminated. Photons propagating within the medium far from the fiber face do not contribute to the collected reflectance intensity and were terminated at a hemispherical limit from the fiber face of  $10 \frac{d_{fb}}{\mu'_s}$ ; a limit that was confirmed to not influence model outputs for the range of optical properties investigated in this study. For each simulation, the MC code outputted the reflectance intensity as the ratio of the total number of photons collected (TPC) to the total number of photons launched (TPL) during the MC simulation, calculated as:

$$R_{SF}^{MC} = \frac{TPC}{TPL}. \quad (2.1)$$

MC simulations were run over a broad range of reduced scattering coefficient values ( $\mu'_s = [0.1, 0.3, 1, 3, 10, 30, 100, 300] \text{ mm}^{-1}$ ) and 5 different fiber diameters [0.2, 0.4, 0.6, 0.8, 1.0] mm. To investigate the dependence of the collected signal on phase function, sets of simulations were run that investigated variations in both phase function and anisotropy values. Figure 2.2 shows the the angular scattering probability of selected phase functions. The Henyey-Greenstein-phase function (HG), commonly used to describe photon scattering in tissue, was simulated for g-values of [0.5, 0.7, 0.8, 0.9].

The Modified Henyey-Greenstein phase function (MHG), which contains a pronounced backscattering feature, was simulated with an effective anisotropy value of  $g = 0.9$  as in [20,22]. In order to compare simulations with experimental measurements in Intralipid 20%, simulations were performed with the wavelength-dependent phase functions of Intralipid as given by Michels *et al.* [36]. Simulations were run for wavelengths from 400 to 900 nm in steps of 50 nm; corresponding anisotropy values for these phase functions were in the range of  $[0.47 - 0.82]$ . At least 2 million photons were launched for each MC simulation.

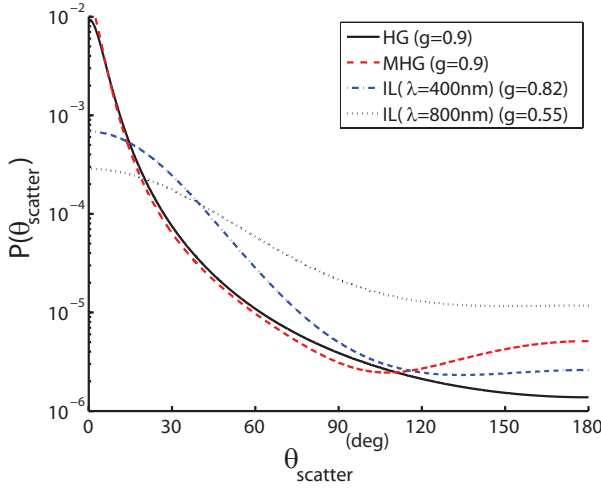


**Figure 2.2:** Angular distribution of scattering events for selected scattering phase functions.

### *Semi-empirical model of the single fiber reflectance intensity*

Inspection of the range of simulated scattering properties yielded an empirical relationship between  $(R_{SF}^{MC})$  and the product  $\mu'_s d_{fib}$ ; this product is referred to throughout this paper as dimensionless scattering. The empirical model is given by the following set of equations,

$$R_{SF}^{Model} = \frac{TPC}{TPL} = \eta_c \Phi, \quad (2.2)$$

$$\Phi = \frac{TPH}{TPL} = \left[ \frac{(\mu'_s d_{fib})^{\rho_2}}{\rho_1 + (\mu'_s d_{fib})^{\rho_2}} \right], \quad (2.3)$$

$$\eta_c = \frac{TPC}{TPH} = \eta_{limit} (1 + \rho_3 e^{-\rho_1 (\mu'_s d_{fib})}). \quad (2.4)$$

The collected reflectance intensity ( $R_{SF}^{Model}$ ) is calculated as the ratio of the total number of photons collected ( $TPC$ ) to the total number of photons launched ( $TPL$ ) during the MC simulation, as given in Eq. 2.2. This ratio can be described by the the product of the fraction of photons remitted from the medium that contact the fiber face ( $\Phi$ ), and the collection efficiency ( $\eta_c$ ) of the fiber. Eq. 2.3 presents  $\Phi$  as the ratio of photons that are remitted from the medium and contact the fiber face ( $TPH$ ) at all angles vs. the  $TPL$ . The right hand side of Eq. 2.3 introduces a mathematical expression that captures a saturating relationship [37] between  $\Phi$  and dimensionless scattering that was observed in the MC outputs. The collection efficiency ( $\eta_c$ ) is given in Eq. 2.4 as the ratio of the photons of  $TPC/TPH$ , which represents the fraction of all photons remitted from the tissue that contact the fiber face within the cone of acceptance of the fiber. The concept of  $\eta_c$  has been described in detail previously by Bargo *et al.* [33]; in brief,  $\eta_c$  is dependent on optical properties but for high scattering coefficients it collapses to an approximate lower limit of  $\eta_{limit} \approx \sin^2(\Theta_a)$ . The observed dependence of both  $\Phi$  and  $\eta_c$  on dimensionless scattering is presented in Figures 2.4B and C.

The parameters  $[\rho_1, \rho_2, \rho_3]$  were fitted by minimizing the weighted residual error between the simulated ( $R_{SF}^{MC}$ ) and model-estimated ( $R_{SF}^{Model}$ ) reflectance intensities, with each point weighted by the inverse of the simulated data point. It is important to note that neither  $\Phi$  nor  $\eta_c$  are observable from our experiments, and while they were estimated by the MC model, the fitted parameter values  $[\rho_1, \rho_2, \rho_3]$  were only fitted to reflectance intensity data using Eq. 2.2; *i.e.* we did not separately fit Eqs. 2.3 and 2.4 which represent unobservable quantities. Parameters were estimated using a Levenberg-Marquardt algorithm [38] written into Matlab code (version R2009a, MathWorks). Confidence intervals of the parameter estimates were calculated from the square root of the diagonal of the covariance matrix, as described in detail elsewhere [39].

### **Experimental setup for single fiber reflectance spectroscopy**

Figure 2.1 shows a schematic of the single fiber reflectance spectroscopy device setup, which consists of a halogen light source (HL-2000-FHSA, Ocean Optics, Duiven, Netherlands), a spectrometer (SD2000, Ocean Optics, Duiven, Netherlands) and a solid core single fiber probe. The single fiber ( $d_{fiber}=[0.2, 0.4, 0.6, 0.8, 1]$  mm) is connected to the light source and the spectrometer via a bifurcated fiber. During measurements, light travels from the light source through the fiber and exit into the probe tip that is in contact with the sampled medium. Photons that backscatter to the fiber face at an incident angle that is within the cone of acceptance enter the fiber core and travel to the spectrometer. To remove specular reflections within the collected reflectance intensity due to index of refraction mismatch at the probe/medium interface tip, the

probe tip is polished at an angle of 15 degrees [24]. Variations in the output of the lamp, transmission characteristics of the fiber, and sensitivity of the spectrometer, as well as remaining specular reflectance and other internal reflections are being accounted for by performing a calibration procedure that we have described previously [34]. The calibration includes measurements of white and black spectralon standards (Labsphere SRS-99 and SRS-02, spectrally flat, with 99% and 2% reflectance, respectively) and a measurement of water in a black container. The single fiber reflectance signal can be calculated as

$$R_{SF}^{meas-rel} = \left[ \frac{I - I_{water}}{I_{white} - I_{black}} \right]. \quad (2.5)$$

Here  $I_{water}$ ,  $I_{white}$ , and  $I_{black}$  are the measured intensities of water, and black and white spectralon respectively and  $I$  stands for the measured intensity of the sample. Because the signals  $I_{white}$  and  $I_{black}$  depend on the distance of the fiber probe to the spectralon during calibration measurement,  $R_{SF}^{meas-rel}$  calculated in Eq. 2.5 is relative to the spectralon distance.

### ***Solid phantom preparation***

Solid phantoms were prepared according to the recipe reported by de Bruin *et al.* [40]. Silicone [Sylgard 184 Silicone Elastomer Kit (Dow Corning Europe SA, Seneffe, Belgium)] served as a stable matrix and Titanium dioxide ( $TiO_2$ ) (Sigma Aldrich, Zwijndrecht, Netherlands) was used as a scatterer. All solid phantoms were prepared with a weight of 20 g, including different amounts of  $TiO_2$  to create a series of different highly scattering phantoms ( $TiO_2$  weight percentage = [0, 2.5, 5, 10, 20, 30] %). The silicone kit consisted of the silicone compound and a curing agent which was always mixed in a ratio of 9:1. To prepare the phantoms the silicone compound and  $TiO_2$  were weighed, mixed with a Dremel 300 (Dremel, Leinfelden-Echterdingen, Germany) and placed into an ultrasound bath for 10 min, to assure that the  $TiO_2$  particles were homogeneously distributed within the silicone. Then the curing agent was added and the composition was mixed again until the agent was completely mixed into the compound. The mass was poured into the mold and placed in a vacuum desiccator (Duran Group GmbH, Mainz, Germany) and held under vacuum until remaining air bubbles were removed from the phantom (1 – 3 hours). The phantoms were cured after approximately 12 hours at room temperature.

During the single fiber reflectance measurements the single fiber probe tip was brought into contact with the phantom surface, with no gap between fiber face and phantom surface. Three spectra were recorded at 3 different locations on the phantom surface and averaged. Each phantom was measured with the 5 different fiber probes

with diameters of [0.2, 0.4, 0.6, 0.8, 1.0] mm. To test the homogeneity of the phantoms and the reproducibility of the preparation, 6 solid phantoms with a weight percentage of 30%  $\text{TiO}_2$  were prepared and single fiber spectra were measured at 10 different locations on each phantom surface. The maximum relative deviation between measurements on two phantoms was 0.66 %, while the intra-phantom variability was even lower.

### ***Liquid phantom preparation***

The liquid phantoms were prepared by mixing 0.9% NaCl (Baxter, Utrecht, Netherlands) with different amounts of Intralipid 20% (Fresenius Kabi, s-Hertogenbosch, Netherlands). The reduced scattering coefficient of the Intralipid stock solution was determined to be  $\mu'_s(800\text{nm}) = 18.1 \text{ mm}^{-1}$  by using the formula given by Michels *et al.* [36]. The dependence of  $\mu'_s$  on the intralipid concentration was assumed to be linear and phantoms with  $\mu'_s(800\text{nm}) = [0.072, 0.144, 0.24, 0.36, 0.48, 0.72, 0.96, 1.2, 2.4, 3.6] \text{ mm}^{-1}$  were prepared to a volume of 20 ml. Reflectance measurements were performed by submerging the probe tip a few millimeters into the phantom and suspending it multiple centimeters from the container bottom or sides, such that the probe would not collect reflections from container surfaces. The measurement was repeated 3 times for each phantom, with these spectra averaged for each phantom. All measurements were performed with 5 fiber probes varying in diameter: [0.2, 0.4, 0.6, 0.8, 1] mm. The phantom was gently agitated before collecting each spectrum to ensure homogeneity.

### ***Absolute calibration of experimental single fiber reflectance spectra***

Measurement of single fiber reflectance intensity from the set of solid  $\text{TiO}_2$  phantoms yielded  $R_{SF}^{meas-rel}$  vs.  $\text{TiO}_2$  weight percentage (wt %) for a range of  $\text{TiO}_2$  wt % and fiber diameters.  $\text{TiO}_2$  wt % was converted to  $\mu'_s$  by estimating a linear conversion factor. In order to do this, measurements on the set of solid phantoms from all fibers were interpolated onto a curve that was normalized to the highest measured intensity in the set; this conversion is corrected for different probe-spectralon distances. Then a linear conversion factor ( $\mu'_s/\text{TiO}_2$  wt %) was estimated by scaling the normalized reflectance vs.  $\text{TiO}_2$  wt % data to fit the reflectance predicted by the mathematical model, presented in Eq. 2.2. This calculation yields a  $\mu'_s$  for each  $\text{TiO}_2$  phantom.

Measurements of liquid Intralipid phantoms were converted from a value relative to spectralon distance,  $R_{SF}^{meas-rel}(IL)$ , to an absolute percentage scale,  $R_{SF}^{meas-abs}(IL)$ , by,

$$R_{SF}^{meas-abs}(IL) = R_{SF}^{meas-rel}(IL) \left[ \frac{R_{SF}^{meas-abs}(phantom)}{R_{SF}^{meas-rel}(phantom)} \right], \quad (2.6)$$

where  $R_{SF}^{meas-rel}$  (*phantom*) is the relative reflectance intensity measured from a solid  $TiO_2$  phantom after the calibration procedure given in Eq. 2.5 and  $R_{SF}^{meas-abs}$  (*phantom*) is the absolute reflectance of that phantom expressed as a percentage of incident photons, which is calculated from the known  $\mu'_s$  of the phantom and the empirical model of reflectance given in Eq.2.2 (using values for  $[\rho_1, \rho_2, \rho_3]$  specified in the Results section).

## Results

### *Mathematical characterization of $R_{SF}^{MC}$ dependence on scattering properties*

#### *Influence of phase function on $R_{SF}^{MC}$ vs. dimensionless scattering*

Figure 2.3 shows the MC simulated reflectance intensity ( $R_{SF}^{MC}$ ) vs. dimensionless scattering ( $\mu'_s d_{fib}$ ) with combinations of a wide range of  $\mu'_s$  [0.1 – 300]  $mm^{-1}$  and  $d_{fib}$  [0.2 – 1.0] mm. Here,  $R_{SF}^{MC}$  is expressed as a percentage of the incident photons. In Figure 2.3, symbols differentiate the specified phase function, including  $R_{SF}^{MC}$  data from the HG ( $g$  values in the range of [0.5–0.9]) and MHG (effective  $g = 0.9$ ) phase functions (see legend). Inspection of the data for each investigated phase function, shows that  $R_{SF}^{MC}$  increases monotonically vs.  $\mu'_s d_{fib}$  until approaching an asymptotic limit for high dimensionless scattering values. For all phase functions investigated, the  $R_{SF}^{MC}$  data show a transition from a phase-function dependent regime at low  $\mu'_s d_{fib}$  to a region insensitive to phase function at higher  $\mu'_s d_{fib}$ , with the transition point between the two regimes occurring for all phase functions at approximately  $\mu'_s d_{fib} > 10$ . In the low dimensionless scattering region, there is a clear stratification between reflectance intensities measured from different phase functions, with increased reflectance attributable to an increase in the backscattering component of the phase function. Therefore, for the same effective  $g$ ,  $R_{SF}^{MC}$  is greater for the MHG than for the HG phase function; the difference is attributable to more high angle backscatter events in the MHG phase function, which is evident from the plot of the phase functions displayed in Figure 2.2. Moreover, the  $R_{SF}^{MC}$  from HG simulations stratifies in order of decreasing backscatter component, with greater reflectance collected from phase functions containing a higher percentage of large angle back scatter events (e.g.  $g = 0.5$  resulted in a higher reflectance than  $g = 0.9$ ). Conversely, in the region of high dimensionless scattering ( $\mu'_s d_{fib} > 10$ ) the  $R_{SF}^{MC}$  shows an insensitivity to backscattering features of the phase function, as data from all phase functions converge until they overlap and then asymptotically approach a limiting reflectance value. These results indicate that  $R_{SF}^{MC}$  is dependent on the phase function in a region of low-mid dimensionless scattering but approaches phase function independent behavior in a region of very high values of  $\mu'_s d_{fib}$ .

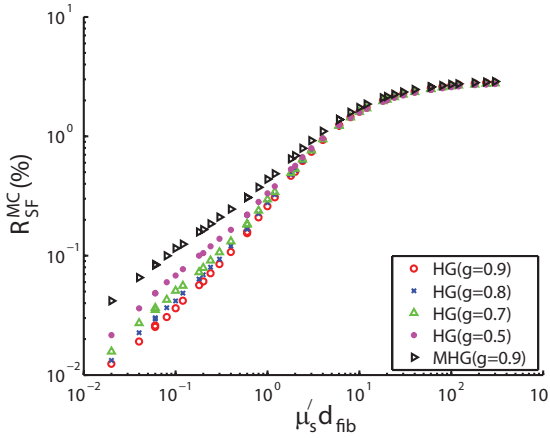


**Figure 2.3:** Single fiber reflectance vs. dimensionless scattering for HG phase function ( $g=[0.5,0.7,0.8,0.9]$ ) and MHG phase function ( $g=0.9$ ).

#### *Empirical model of $R_{SF}^{MC}$ vs. dimensionless scattering*

The observed relationship between  $R_{SF}^{MC}$  and  $\mu'_s d_{fib}$  was described using an empirical model introduced (Eq. 2.2 - 2.4). Figure 2.4 A shows  $R_{SF}^{MC}$  for the HG phase function with  $g = 0.8$  for  $\mu'_s = [0.1 - 300] \text{ mm}^{-1}$  and  $d_{fib} = [0.2 - 1.0] \text{ mm}$  (cross marks), and the corresponding model predicted reflectance ( $R_{SF}^{Model}$ ) estimated from Equation (2.2) (black line). The estimated parameter values, given in Table 1, result in predictions of  $R_{SF}^{Model}$  that are highly correlated with simulated reflectance intensities over the full dimensionless scattering range, as evidenced by a Pearson Correlation Coefficient of  $R = 0.999$  and a mean residual error of  $< 3\%$ .

Eq. 2.2 expresses  $R_{SF}^{Model}$  as the product of  $\Phi$ , the fraction of incident photons that are remitted from the medium in contact with the probe face, and  $\eta_c$ , the fraction of photons that contact the fiber face within the cone of acceptance and are collected. Figure 2.4 B and 2.4 C show the MC model estimates (squares and diamonds) and mathematical model predictions (black lines) of  $\Phi$  and  $\eta_c$ , respectively, expressed as percentages, as calculated from Eq. 2.3 and 2.4. Figure 2.4B shows that  $\Phi$  increases with  $\mu'_s d_{fib}$  and exhibits a saturating behavior as it approaches the 100% upper limit, a feature well described by the model. Figure 2.4C shows that  $\eta_c$  shows a decreasing trend vs. dimensionless scattering, until approximately  $\mu'_s d_{fib} < 1$ , at which point it approximates a limit linked to the fiber opening angle of acceptance; this behavior is consistent with a previous theoretical analysis [33] and is discussed in detail in the discussion section. It is important to note that the estimated model parameters in Eq. 2.2 were not informed by MC estimates of  $\Phi$  and  $\eta_c$ , as they are not observable experimentally. Instead  $\Phi$  and  $\eta_c$  were calculated from the parameters resulting from the fit of  $R_{SF}^{Model}$  from Eq. 2.2 to the data, as shown in Figure 2.4 A. The results presented in Figures 2.4 B and 2.4 C suggest that the mathematical expressions

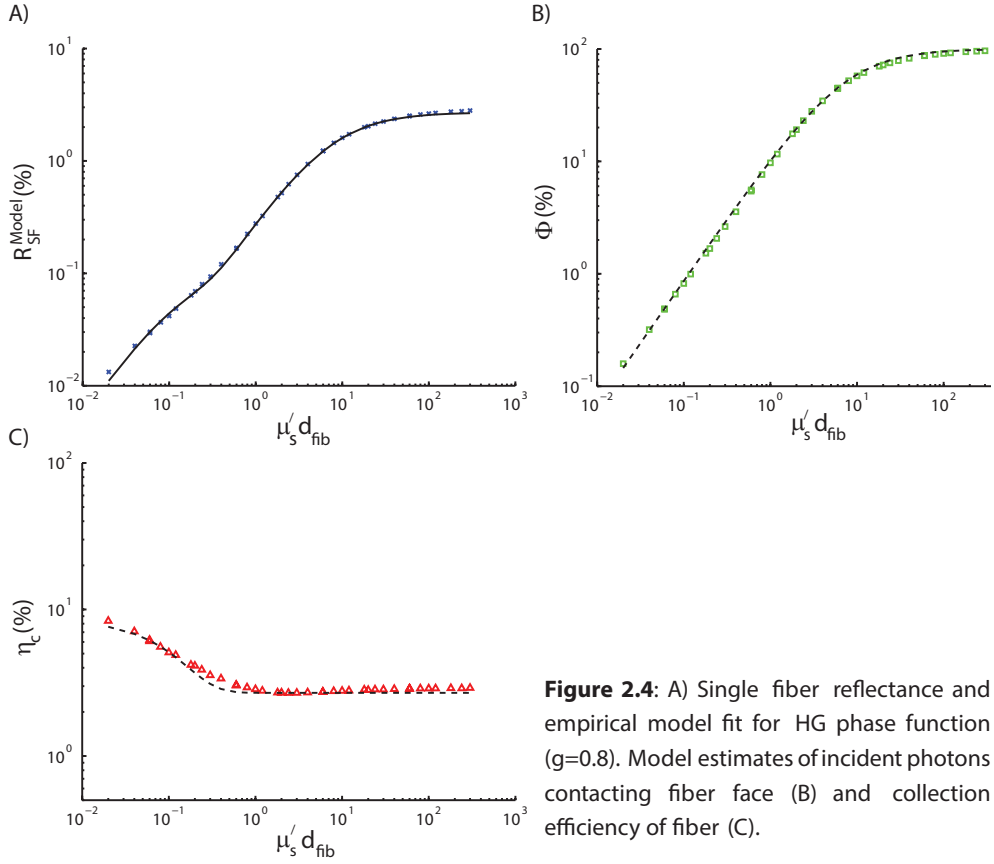


**Figure 2.4:** A) Single fiber reflectance and empirical model fit for HG phase function ( $g=0.8$ ). Model estimates of incident photons contacting fiber face (B) and collection efficiency of fiber (C).

used to represent  $\Phi$  and  $\eta_c$  as components of  $R_{SF}^{Model}$  are, in fact, representative of the true underlying factors contributing to collected reflectance.

Figure 2.5 shows  $R_{SF}^{Model}$  vs.  $R_{SF}^{MC}$  for  $\mu'_s = [0.1 - 300] \text{ mm}^{-1}$  and  $d_{fib} = [0.2 - 1.0] \text{ mm}$ , with symbols distinguishing each phase function, including HG ( $g = [0.5 - 0.9]$ ) and MHG ( $g = [0.9]$ ). Model parameters for  $R_{SF}^{Model}$  were fit for each simulated phase function; estimated parameter values for each fit are shown in Table 2.1 (top). Model predictions show an excellent agreement with simulated reflectance intensities over the range of phase functions investigated, with all R values above 0.998; additionally, the mean residual between all model estimated and MC simulated data points was  $< 3\%$ . These data indicate that the dependence of  $R_{SF}^{Model}$  on dimensionless scattering can be accurately estimated for a given phase function.



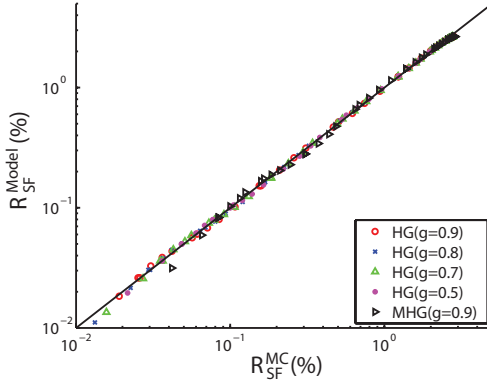


**Figure 2.5:** MC simulated single fiber reflectance vs. model estimate.

## Experimental determination of $\mu'_s$ from $R_{SF}$

### $R_{SF}^{meas-abs}$ measured from solid $\text{TiO}_2$ phantoms

Reflectance measurements on  $\text{TiO}_2$  phantoms yielded  $R_{SF}^{meas-rel}$  vs.  $\text{TiO}_2$  wt % data in the range [2.5–30] wt %. As outlined in the methods section, these data were scaled to  $R_{SF}^{meas-abs}$  using the empirical reflectance model. Because the exact phase function of the  $\text{TiO}_2$  phantoms is unknown, we used the averages of the fitted parameter values:  $\rho_1 = 7.9, \rho_2 = 1.08, \rho_3 = 2.4$ . Using these parameter values, a linear conversion factor of  $\mu'_s / \text{TiO}_2 \text{ wt \%} = 7.42 \pm 0.35$  was found. Figure 2.6 shows the  $R_{SF}^{meas-abs}$  (800nm) from all measurements on  $\text{TiO}_2$  phantoms vs.  $\mu'_s d_{fib}$  as measured with 5 probes with diameters in the range [0.2–1.0] mm, using the 7.42 ( $\mu'_s / \text{TiO}_2 \text{ wt \%}$ ) ratio. Also displayed on the plot are  $R_{SF}^{MC}$  vs  $\mu'_s d_{fib}$  from simulations of an HG phase function with  $g = 0.8$ , which shows good agreement between experimental and simulated data. Note that due to the high reduced scattering coefficients of the phantoms, these measurements are in the high dimensionless scattering region ( $\mu'_s d_{fib} > 10$ ), which showed an insensitivity to phase function. Varying the parameters  $\rho_1 - \rho_3$  in Eq. 2.2 to be representative of HG ( $g = [0.5 - 0.9]$ ) and MHG ( $g = [0.9]$ ) phase functions (see Table 2.1) induced only a 2.2% mean residual error between  $R_{SF}^{meas-abs}$  (based on the average  $\rho_1 - \rho_3$ ) and  $R_{SF}^{Model}$  (based on the different  $\rho_1 - \rho_3$  combinations listed in Table 2.1). These results led to the selection of the 30%  $\text{TiO}_2$  phantom (which equated to  $\mu'_s = 222.6 \pm 10.5 \text{ mm}^{-1}$ ) as the calibration phantom for subsequent measurements on Intralipid.

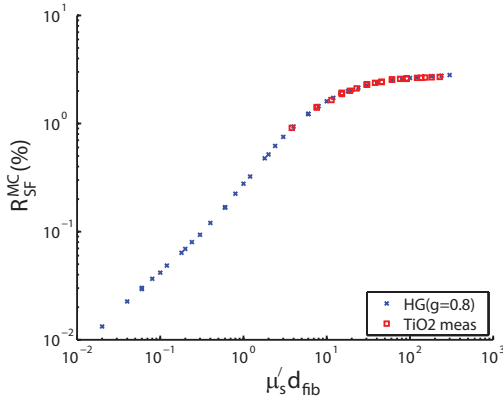


**Figure 2.6:** Single fiber reflectance measured on TiO<sub>2</sub> phantoms and simulated by MC model (HG phase function with  $g = 0.8$ ).

### $R_{SF}^{meas-abs}$ measured from Intralipid phantoms

Figure 2.7A shows  $R_{SF}^{meas-abs}$  from measurements of Intralipid at multiple wavelengths ( $\lambda = [400 - 900]$  nm in steps of 100 nm) vs. dimensionless scattering. Here the  $R_{SF}^{meas-abs}$  values represent the raw intensities scaled by measurements on the solid calibration phantom, allowing the conversion to an absolute scale. This calibration technique allows reflectance intensities from measurements with 5 fibers with different diameters to fall onto the same curve. Figure 2.7B shows  $R_{SF}^{MC}$  vs.  $\mu'_s d_{fib}$  from MC simulations of the reflectance measurements in Intralipid over the same range of wavelengths. Here, the phase function for each wavelength was specified using an empirical model (as in [36]), and the corresponding anisotropy values were in the range  $g = [0.477 - 0.818]$ . For both measurements and simulations, the  $R_{SF}$  values measured at different wavelengths (and therefore different phase functions) show stratification at low dimensionless scattering values, and gradually collapse towards a limiting value; these features are similar to the data shown in Figure 2.3 for HG and MHG phase functions. Figure 2.8A displays the corresponding simulated  $R_{SF}^{MC}$  vs. measured  $R_{SF}^{meas-abs}$  values. These data are highly correlated ( $R = 0.998$ ) and show good agreement (with a mean residual of  $< 8\%$ ) over a range of measured reflectance values that span 2 orders of magnitude (range =  $[0.0158 - 1.57]\%$ ). It should be noted that relative deviation between simulation and experimental data increases for decreasing measured reflectance, and in turn for decreasing dimensionless scattering. After accounting for the index of refraction mismatch between experimental and simulated phantoms (1.33 vs. 1.37, respectively), a linear fit of these data through the origin gives a slope of 1.04.

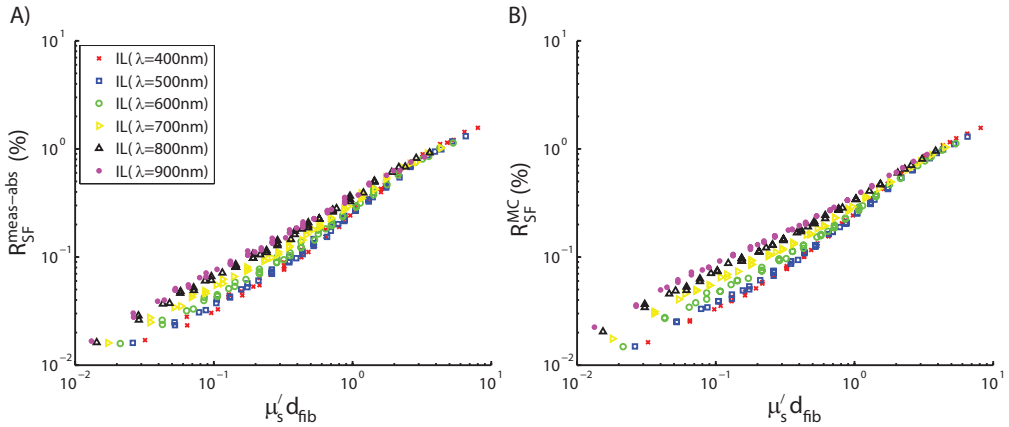


**Figure 2.7:** Single fiber reflectance measured (A) and simulated (B) from Intralipid optical phantoms at multiple wavelengths  $\lambda = [400, 500, 600, 800, 900]$  nm; other wavelengths measured in this range not shown to improve clarity.

### Experimental estimation of $\mu'_s$ from $R_{SF}^{meas-abs}$

The empirical reflectance model given in Eq. 2.2 was fitted to  $R_{SF}^{MC}$  simulated in Intralipid for each wavelength-dependent phase function. Table 2.1 (bottom) lists detailed data for each simulation, including the anisotropy, estimated parameters values, and Pearson correlation coefficients for each fit. These empirical model fits were then used to analyze  $R_{SF}^{meas-abs}$  measured experimentally from Intralipid phantoms and estimate  $\mu'_s$ . Prior to this calculation, the  $R_{SF}^{meas-abs}$  data are corrected for slight offset with MC simulations.

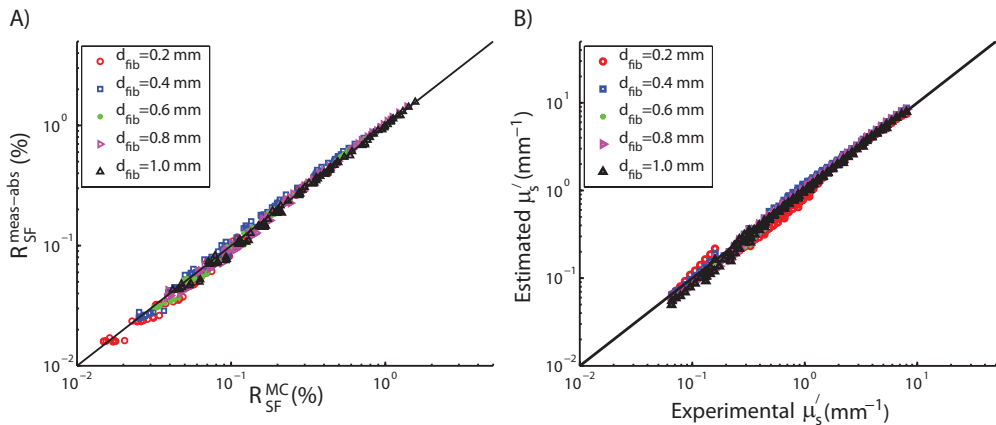


**Figure 2.8:** Comparison of (A) single fiber reflectance intensity from MC simulations with experimental measurements from Intralipid phantoms  $\lambda = [400-900]$  nm; (B)  $\mu'_s$  estimated from  $R_{SF}^{meas-abs}$  vs. known value.

**Table 2.1:** Estimated parameter values and confidence intervals (CI) resulting from fits of single fiber reflectance model Eq. 2.2 - 2.4 to  $R_{SF}$  simulated by Monte Carlo models for HG and MHG phase function (top) and wavelength-dependent phase functions [36] in Intralipid (bottom).

Phase Function	g	$\rho_1$		$\rho_2$		$\rho_3$		r
		Value	CI	Value	CI	Value	CI	
HG	0.9	9.374	0.406	1.152	0.027	2.338	0.851	0.9994
HG	0.8	8.866	0.321	1.120	0.022	2.295	0.667	0.9995
HG	0.7	8.315	0.270	1.086	0.020	2.267	0.561	0.9996
HG	0.5	7.251	0.199	1.018	0.017	2.108	0.405	0.9998
MHG	0.9	5.676	0.383	1.034	0.046	3.125	1.131	0.9987
Phase Function	g	$\rho_1$		$\rho_2$		$\rho_3$		r
		Value	CI	Value	CI	Value	CI	
Intralipid (400nm)	0.818	9.496	0.103	1.245	0.011	2.995	0.362	0.9998
Intralipid (450nm)	0.783	10.001	0.093	1.208	0.010	3.144	0.313	0.9999
Intralipid (500nm)	0.749	9.927	0.124	1.170	0.014	3.072	0.401	0.9997
Intralipid (550nm)	0.715	9.512	0.124	1.127	0.015	2.745	0.375	0.9996
Intralipid (600nm)	0.681	9.014	0.119	1.090	0.017	2.533	0.350	0.9995
Intralipid (650nm)	0.647	8.389	0.091	1.054	0.015	2.170	0.255	0.9996
Intralipid (700nm)	0.613	7.816	0.077	1.021	0.014	2.010	0.218	0.9996
Intralipid (750nm)	0.579	7.361	0.077	0.983	0.016	1.723	0.209	0.9995
Intralipid (800nm)	0.545	6.899	0.077	0.947	0.018	1.437	0.204	0.9994
Intralipid (850nm)	0.511	6.592	0.060	0.935	0.016	1.461	0.168	0.9997
Intralipid (900nm)	0.477	6.323	0.054	0.911	0.016	1.390	0.156	0.9997

Figure 2.8B shows  $\mu'_s$  estimated using  $R_{SF}^{meas-abs}$  and the empirical model vs. the known experimental  $\mu'_s$  value; these data are highly correlated ( $r = 0.997$ ) and show good agreement, with a mean residual of 9%. As observed in the reflectance data, the relative error in  $\mu'_s$  estimates increases as dimensionless scattering decreases.

## Discussion

This paper presents a methodology to quantitatively extract  $\mu'_s$  from the reflectance intensity collected by a single fiber reflectance device ( $R_{SF}$ ). Monte Carlo simulations were used to investigate the dependence of  $R_{SF}$  on the scattering properties of an optically sampled turbid medium. Simulated data were used to identify a relationship between  $R_{SF}$  and  $\mu'_s d_{fib}$ , which showed that  $R_{SF}$  approached phase function independent behavior for  $\mu'_s d_{fib} > 10$ . This theory motivated the construction of a solid optical phantom with a very high reduced scattering coefficient ( $\mu'_s > 200 \text{ mm}^{-1}$ ); such that measurements of  $R_{SF}$  from this phantom are independent of phase function and can be used to calibrate any measured reflectance intensity to an absolute scale. Experimental data show that this methodology can be used to accurately extract  $\mu'_s$  from  $R_{SF}$  measurements

of optical phantoms over a wide range of  $\mu'_s = [0.1 - 8] \text{ mm}^{-1}$  and  $d_{fib} = [0.2 - 1] \text{ mm}$  for a specified phase function. The work presented here provides an approach to quantitative estimation of both  $\mu'_s$  and  $\mu_a$  from turbid media, such as tissue.

Monte Carlo simulations were used to investigate the effect of  $\mu'_s$ ,  $d_{fib}$ , and phase function on  $R_{SF}$ . Inspection of the data showed a relationship between  $R_{SF}$  and  $\mu'_s d_{fib}$ , which was characterized by two regimes: (1) a low dimensionless scattering regime where  $R_{SF}$  depends on phase function, and (2) a high dimensionless scattering regime where  $R_{SF}$  becomes independent of phase function and asymptotically approaches a limit. The transition point between these regimes was observed to be approximately  $\mu'_s d_{fib} \approx 10$ . The low dimensionless scattering regime contains reduced scattering values that are experienced during measurements of tissue (common range  $\mu'_s = [0.5 - 5.0] \text{ mm}^{-1}$ ) by single fibers with diameters commonly used clinically (common range  $d_{fib} = [0.2 - 1.0] \text{ mm}$ ). While the high dimensionless scattering regime will not be experienced in biological tissue, the insensitivity of  $R_{SF}$  to phase function in this region allows measurements of tissue (of any phase function) to be calibrated onto an absolute scale.

The experimental application of this theory motivated the construction of a solid optical phantom with a large concentration of scattering material ( $\text{TiO}_2$ ) that corresponded to  $\mu'_s$  values that were within the high dimensionless scattering (and phase function insensitive) regime. These solid phantoms allow single fiber reflectance intensities measured from different fibers to be calibrated onto the same absolute scale; previously, this was difficult due to the fiber-diameter dependent effect of and variations in probe-spectralon distance utilized in our previous calibration technique. In this study reflectance measurements on the set of phantoms investigated were scaled to a reflectance model to determine the relationship between  $\text{TiO}_2$  wt % and  $\mu'_s$ . We have assumed that this conversion factor is linear. While it is possible that the relation may not be linear, the data shown on Figure 2.6 present a convincing argument that this assumption is appropriate. Uncertainty associated with the  $\mu'_s / \text{TiO}_2$  wt % ratio is not expected to introduce error. This is because the highest scattering phantom (30 wt %  $\text{TiO}_2$ ) was selected for scaling subsequent measurements (on liquid phantoms in this study, or on tissue in future work), and in this dimensionless scattering region, a mis-estimation of  $\mu'_s$  for this phantom are not expected to be significant due to the relatively small changes in  $R_{SF}$  corresponding to changes in  $\mu'_s$  in this regime.

The empirical model function used to describe the relation between  $R_{SF}$  and dimensionless scattering for each investigated phase function contains 3 fitted parameters, given by Eq. 2.2 - 2.4. The development of this mathematical model provided insight into the factors contributing to the collected signal. The model represents the light collected during measurement as a product of the photons contacting the fiber surface ( $\Phi$ ) and the fraction of those photons within the fiber cone of acceptance ( $\eta_c$ ). Figure 2.4B

shows that  $\Phi$  increases with dimensionless scattering, until it saturates as it approaches the 100% limit. This behavior was described using a saturating mathematical expression, which included a phase-function specific fitted power ( $\rho_2$ ) on the dimensionless scattering term; while the fitted values for this parameter were relatively close to unity (range=[1.018 – 1.152], see Table 2.1) the model fit quality was significantly increased by fitting the parameter. Figure 2.4C shows that  $\eta_c$  is large for small dimensionless scattering values and decreases as it approaches a limiting value. This transition can be rationalized by considering the effect of the optical properties of the turbid medium on the angular distribution of remitted light; this concept has been described in detail previously by Bargo *et al.* [33]. In brief, small dimensionless scattering values indicate that photons travel relatively large distances between scattering events. Therefore photons remitted from the medium at the fiber face have a high probability of being scattered from (relatively) deep locations in the medium, and in turn are traveling at angles near normal to the tissue interface. As the dimensionless scattering increases, photons are more likely to be remitted from shallow distances into the medium with remitted light exiting diffusely at all angles. Theoretically,  $\eta_c$  in this regime approaches a diffuse limit defined by the projection of the solid angle of the acceptance cone onto the medium/fiber plane divided by all possible solid angles for light remitted across that plane; the mathematics underlying this theory has been described in detail by Horn *et al.* [41], and applied to single fiber reflectance spectroscopy by Bargo *et al.* [33]. It should be noted that in the highly scattering region ( $\mu'_s d_{fib} > 10$ ), the angular distribution of remitted light calculated by the MC model is not perfectly diffuse; instead, a subcomponent of the light collected by the single fiber device has undergone few scattering events, which causes slight variations (approximately 5%) in  $\eta_c$  for different phase functions. This phenomenon is known to occur for optical devices with overlapping source and detection areas on a medium interface, and has been described in detail previously by Snabre *et al.* [42]. It should also be noted that Equation 2.4 is dependent on the fiber NA. Simulations investigating variations of NA on  $R_{SF}$  showed that the effect could be characterized by adjusting  $\eta_{limit}$  exclusively (without refitting parameters [ $\rho_1, \rho_2, \rho_3$ ]), with  $\approx 5\%$  mean error between estimates of  $R_{SF}$  measured by fibers of NA= [0.22] and NA= [0.1, 0.4] in the biologically relevant scattering range ( $\mu'_s = [0.44 - 4] \text{mm}^{-1}$ ) over a range of phase functions, with increasing deviations associated with decreasing  $\mu'_s d_{fib}$  (data not shown).

This study includes an experimental proof of concept for the extraction of  $\mu'_s$  from experimental measurements of optical phantoms containing Intralipid. As part of that investigation,  $R_{SF}$  was simulated by a MC model that emulated the experimental measurements in optical phantoms. These techniques yielded  $R_{SF}$  values that were highly correlated, as observed in Figure 2.8A and B. However, as noted in the Results,

there was a slight discrepancy between the simulated and the measured  $R_{SF}$  from Intralipid phantoms, with a 4% increase in measured value vs. the corresponding simulated values. One explanation for this slight mismatch is that the probes used for the experimental measurements have the fiber tip polished at an angle of 15 degrees, altering the fiber face from a circle to an elliptical cross-section, and increasing the area by approximately 3%; this mismatch is expected to represent the bulk of the 4% offset. Moreover, it was observed that the relative error in  $R_{SF}$  estimates increased with decreasing dimensionless scattering. This is most likely caused by slight mismatches between the actual phase function of the liquid phantoms and the model approximation utilized in the MC model [36]. Another source of mismatch may be in the specification of the index of refraction of both fiber and sample in the MC simulation, which was assumed wavelength independent. Slight mismatches between experiment and simulation would be observed especially in regions of small dimensionless scattering values where the reflectance signal is most sensitive to phase function.

The goal for performing the absolute  $R_{SF}$  calibration was to extract an absolute value for  $\mu'_s$  within the sampled turbid medium from the measured single fiber reflectance intensity. This was achieved in this study by performing measurements on Intralipid phantoms, calibrating the measured reflectance with measurements on the highly scattering solid calibration phantom, and analyzing the data using a phase-function specific mathematical model describing the dependence of reflectance on dimensionless scattering. The work in this study calculated  $\mu'_s$  for 5 fiber diameters, on Intralipid phantoms of 10 different concentrations at 11 different wavelengths (range [400 – 900] nm), representing a wide range of phase functions and  $\mu'_s = [0.05 - 8] \text{ mm}^{-1}$ . Because this calculation utilized the empirical model fit to MC simulations to analyze measured reflectance data, the measurements were corrected for the observed 4% offset prior to  $\mu'_s$  estimation, as described in detail earlier in this Section. After this correction we were able to accurately extract the reduced scattering coefficient from Intralipid measurements, with a mean residual of 9% over the entire range of  $\mu'_s$ ; this  $\mu'_s$  range is wider than experienced in tissue, and therefore error associated with biologically relevant  $\mu'_s$  values is expected to be < 9%. In this study the empirical model was used in conjunction with measured reflectance on phantoms to provide absolute estimates of  $\mu'_s$ , estimates that have been demonstrated to be accurate for a given phase function. In tissue, the phase function is generally unknown and assumptions about the values for  $\rho_1 - \rho_3$  that feed into the empirical model must be made. Future studies will investigate how the assumed parameter values affect the estimates of  $\mu'_s$ , and whether the parameter values can be expressed in terms of metrics extracted from a known wavelength-dependent phase function profile. Furthermore, we are currently investigating methods to measure the parameter values experimentally for biological tissues.

## References

- [1] K Gall and G Assanto. All-optical diode based on second-harmonic generation in an asymmetric waveguide. *Journal of the Optical Society of America B*, 16(2):267, February 1999.
- [2] K Sokolov, M Follen, and R Richards-Kortum. Optical spectroscopy for detection of neoplasia. *Current Opinion in Chemical Biology*, 6(5):651–8, October 2002.
- [3] R Drezek, M Guillaud, T Collier, I Boiko, A Malpica, C Macaulay, M Follen, and R R Richards-Kortum. Light scattering from cervical cells throughout neoplastic progression: influence of nuclear morphology, DNA content, and chromatin texture. *Journal of Biomedical Optics*, 8:7, 2003.
- [4] I Georgakoudi and J Van Dam. Characterization of dysplastic tissue morphology and biochemistry in Barrett’s esophagus using diffuse reflectance and light scattering spectroscopy. *Techniques in Gastrointestinal Endoscopy*, 7(2):100–105, 2005.
- [5] R L P van Veen, A Amelink, M Menke-Pluymers, C van der Pol, and H.J.C.M. Sterenberg. Optical biopsy of breast tissue using differential pathlength spectroscopy. *Physics in Medicine and Biology*, 50:2573–2581, 2005.
- [6] M Canpolat, M Akyüz, G A Gökhan, E I Güler and R Tuncer. Intra-operative brain tumor detection using elastic light single-scattering spectroscopy: a feasibility study. *Journal of Biomedical Optics*, 14(5):054021, 2009.
- [7] P B Garcia-Allende, V Krishnaswamy, P J Hoopes, K S Samkoe, O M Conde, and B Pogue. Automated identification of tumor microscopic morphology based on macroscopically measured scatter signatures. *Journal of Biomedical Optics*, 14(3):034034, 2009.
- [8] J Q Brown, K Vishwanath, G M Palmer, N Ramanujam. Advances in quantitative UV-visible spectroscopy for clinical and preclinical application in cancer. *Current Opinion in Biotechnology*, 20(1):119–31, March 2009.
- [9] A Wax and V Backman. *Biomedical Applications of Light Scattering*. McGraw-Hill Professional, 2009.
- [10] T J Farrell, M S Patterson, and B Wilson. A diffusion theory model of spatially resolved, steady-state diffuse reflectance for the noninvasive determination of tissue optical properties *in vivo*. *Medical Physics*, 19(4):879–888, 1992.
- [11] A Amelink and H J M C Sterenberg. Measurement of the local optical properties of turbid media by differential path-length spectroscopy. *Applied Optics*, 43(15):3048–3054, 2004.
- [12] A Amelink, H J C M Sterenberg, M P L Bard, and S A Burgers. *In vivo* measurement of the local optical properties of tissue by use of differential pathlength spectroscopy. *Optics Letters*, 29(10):1087–1089, 2004.
- [13] L C L Chin, W M Whelan, and I A Vitkin. Information content of point radiance measurements in turbid media: implications for interstitial optical property quantification. *Applied Optics*, 45(9):2101–14, March 2006.
- [14] J R Mourant, J Boyer, A H Hielscher, and I J Bigio. Influence of the scattering phase function on light transport measurements in turbid media performed with small source-detector separations. *Optics Letters*, 21(7):546–548, 1996.



- [15] A Kienle, F K Forster, and R Hibst. Influence of the phase function on determination of the optical properties of biological tissue by spatially resolved reflectance. *Optics Letters*, 26(20):1571–1573, 2001.
- [16] F Bevilacqua, D Piguet, P Marquet, J D Gross, B J Tromberg, and C Depeursinge. *In vivo* local determination of tissue optical properties: applications to human brain. *Applied Optics*, 38(22):4939–4950, 1999.
- [17] F Bevilacqua and C Depeursinge. Monte Carlo study of diffuse reflectance at source–detector separations close to one transport mean free path. *Journal of the Optical Society of America A*, 16(12):2935–2945, 1999.
- [18] E L Hull and T H Foster. Steady-state reflectance spectroscopy in the P3 approximation. *Journal of the Optical Society of America A*, 18(3):584–599, 2001.
- [19] M Johns, C A Giller, D C German, and H Liu. Determination of reduced scattering coefficient of biological tissue from a needle-like probe. *Academic Radiology*, 8:211–218, 2001.
- [20] R Reif, O A'Amar, and I J Bigio. Analytical model of light reflectance for extraction of the optical properties in small volumes of turbid media. *Applied Optics*, 46(29):7317–7328, 2007.
- [21] A Kim, M Roy, F Dadani, and B C Wilson. A fiberoptic reflectance probe with multiple source-collector separations to increase the dynamic range of derived tissue optical absorption and scattering coefficients. *Optics Express*, 18:5580–5594, 2010.
- [22] S C Kanick, D J Robinson, H J C M Sterenborg, and A Amelink. Monte Carlo analysis of single fiber reflectance spectroscopy. *Physics in Medicine and Biology*, 54:6991–7008, 2009.
- [23] S C Kanick, C der Leest, J G J V Aerts, H C Hoogsteden, S Kaščáková, H J C M Sterenborg, and A Amelink. Integration of single-fiber reflectance spectroscopy into ultrasound-guided endoscopic lung cancer staging of mediastinal lymph nodes. *Journal of Biomedical Optics*, 15:17004, 2010.
- [24] S C Kanick, C van der Leest, R S Djamin, A M Janssens, H C Hoogsteden, H J C M Sterenborg, A Amelink, J G J V Aerts, and P D Md. Characterization of Mediastinal Lymph Node Physiology *In Vivo* by Optical Spectroscopy during Endoscopic Ultrasound-Guided Fine Needle Aspiration. *Journal of Thoracic Oncology*, 5(7):981–987, 2010.
- [25] B W Pogue and G Burke. Fiber-optic bundle design for quantitative fluorescence measurement from tissue. *Applied Optics*, 37(31):7429–7436, 1998.
- [26] T J Pfefer, K T Schomacker, M N Ediger, and N S Nishioka. Light propagation in tissue during fluorescence spectroscopy with single-fiber probes. *IEEE Journal of Selected Topics in Quantum Electronics*, 7(6):1004–1012, 2001.
- [27] K R Diamond, M S Patterson, and T J Farrell. Quantification of fluorophore concentration in tissue-simulating media by fluorescence measurements with a single optical fiber. *Applied Optics*, 42:2436–2442, 2003.
- [28] H Stepp, T Beck, W Beyer, C Pfaller, M Schuppler, R Sroka and R Baumgartner. Measurement of fluorophore concentration in turbid media by a single optical fiber. *Medical Laser Application*, 22(1):23–34, June 2007.
- [29] M Canpolat and J R Mourant. Particle size analysis of turbid media with a single optical fiber in contact with the medium to deliver and detect white light. *Applied Optics*, 40(22):3792–3799, 2001.

- [30] A Amelink, M P L Bard, S A Burgers, and H J C M Sterenborg. Single-scattering spectroscopy for the endoscopic analysis of particle size in superficial layers of turbid media. *Applied Optics*, 42(19):4095–4101, 2003.
- [31] T P Moffitt and S A Prah. Determining the reduced scattering of skin *in vivo* using sized-fiber reflectometry. In *Society of Photo-Optical Instrumentation Engineers (SPIE) Conference Series*, volume 4613, pages 254–263, 2002.
- [32] T P Moffitt and S A Prah. The specular reflection problem with a single fiber for emission and collection. In *Proc. SPIE: Saratov Fall Meeting*, 2002.
- [33] P R Bargo, S A Prah, and S L Jacques. Collection efficiency of a single optical fiber in turbid media. *Applied Optics*, 42(16):3187–3197, 2003.
- [34] S C Kanick, H J C M Sterenborg, and A Amelink. Empirical model of the photon path length for a single fiber reflectance spectroscopy device. *Optics Express*, 17:860–871, 2009.
- [35] L Wang, S L Jacques, and L Zheng. MCML–Monte Carlo modeling of light transport in multi-layered tissues. *Computer Methods and Programs in Biomedicine*, 47(2):131–146, 1995.
- [36] R Michels, F Foschum, and A Kienle. Optical properties of fat emulsions. *Optics Express*, 16:5907–5925, 2008.
- [37] G R Kepner. Saturation behavior: a general relationship described by a simple second-order differential equation. *Theoretical Biology & Medical Modelling*, 7:11, January 2010.
- [38] D W Marquardt. An algorithm for least-squares estimation of nonlinear parameters. *Journal of the Society for Industrial and Applied Mathematics*, 11(2):431–441, 1963.
- [39] A Amelink, D J Robinson, and H J C M Sterenborg. Confidence intervals on fit parameters derived from optical reflectance spectroscopy measurements. *Journal of Biomedical Optics*, 13:54044, 2008.
- [40] D M M de Bruin, R H Bremmer, V M Kodach, R de Kinkelder, J van Marle, T G van Leeuwen, and D J Faber. Optical phantoms of varying geometry based on thin building blocks with controlled optical properties (Journal Paper). *Journal of Biomedical Optics*, 15(02):25001, 2010.
- [41] B K P Horn and R W Sjöberg. Calculating the reflectance map. *Applied Optics*, 18(11):1770–1779, 1979.
- [42] P Snabre and A Arhaliass. Anisotropic scattering of light in random media: incoherent backscattered spotlight. *Applied Optics*, 37(18):4017–4026, 1998.





# Chapter 3

## Method to quantitatively estimate wavelength-dependent scattering properties from multi-diameter single fiber reflectance spectra measured in a turbid medium<sup>2</sup>

### Abstract

This study utilizes experimentally validated Monte Carlo simulations to identify a novel mathematical formulation of the reflectance intensity collected by a single fiber probe expressed in terms of the reduced scattering coefficient ( $\mu'_s$ ), fiber diameter  $d_{fiber}$ , and a property of the first two moments of the scattering phase function ( $\gamma$ ). This model is then utilized to accurately obtain wavelength-dependent estimates of  $\mu'_s(\lambda)$  and  $\gamma(\lambda)$  from multiple single fiber spectral measurements of a turbid medium obtained with different diameters. This novel method returns accurate descriptions (mean residual < 3%) of both  $\mu'_s$  and  $\gamma$  across the biologically relevant range.

---

2 S. C. Kanick, U. A. Gamm, H. J. C. M. Sterenborg, D. J. Robinson, A. Amelink, **Method to quantitatively estimate wavelength-dependent scattering properties from multi-diameter single fiber reflectance spectra measured in a turbid medium**, Opt Lett. 36:2997-2999 (2011).

Quantitative analysis of white-light reflectance measurements provides information about absorption and scattering properties of an optically sampled turbid medium such as tissue. The tissue scattering properties relate to aspects of the tissue morphology and ultrastructure, factors that may have diagnostic value [1]. Recently, our group has investigated fiber optic devices that utilize a single optical fiber to deliver and collect light during measurement, which offers the advantage of having a small probe profile facilitating incorporation into endoscopic and fine-needle based clinical procedures. The single fiber reflectance (SFR) intensity is known to be sensitive to the tissue scattering coefficient ( $\mu_s$ ), which describes the mean free path between scattering events, and the scattering phase function (PF) [2], which describes the angular distribution of scattering events. These properties are often described in terms of the scattering anisotropy  $g_1 = \langle \cos(\theta) \rangle$  and the reduced scattering coefficient  $\mu'_s = \mu_s(1 - g_1)$ . Previous investigations [3, 4, 5] of light transport near the source (*i.e.* in the non-diffuse regime) utilized the Legendre moments of the PF to characterize the effect of large angle scattering events on the collected reflectance signal, introducing a parameter  $\gamma = \frac{1 - g_2}{1 - g_1}$  that includes information about the first two moments of the PF, given as  $g_1$  and  $g_2$ , respectively. However, these approaches are not valid for source-detector distances of  $\leq 0.5$  mm and are not directly applicable to the SFR geometry. Light transport relevant to the SFR measurement, where source and detector spots overlap and light can travel infinitesimally small distances prior to detection, is not adequately described by any existing empirical model or analytical theory.

Quantitative analysis of SFR spectra requires the use of an empirical model that utilizes a background scattering model to describe the wavelength-dependent collected light intensity in the absence of absorption, and applies a Modified Beer-Lambert law to that profile to account for absorption from tissue chromophores, as described in [6]:

$$R_{SF} = R_{SF}^o e^{-\mu_a \langle L_{SF} \rangle}. \quad (3.1)$$

Here  $R_{SF}^o$  is the single fiber reflectance in the absence of absorption and  $\langle L_{SF} \rangle$  is the effective photon path length, which depends on the optical properties as described in [7, 8]. Previously our group has characterized the sensitivity of  $R_{SF}^o$  to the scattering properties of the optically sampled turbid medium, identifying a PF-specific mathematical dependence on dimensionless reduced scattering, defined as the product of  $\mu'_s$  and  $d_{fiber}$  and given as;

$$R_{SF}^o = \eta_{limit} (1 + \rho_3 e^{(-\rho_1 \mu'_s d_{fiber})}) \left[ \frac{(\mu'_s d_{fiber})^{\rho_2}}{\rho_1 + (\mu'_s d_{fiber})^{\rho_2}} \right], \quad (3.2)$$

where  $\eta_{limit}$  is the diffuse limit to the single fiber collection efficiency, which is 2.7% for a single fiber with NA = 0.22 [9]. Here  $[\rho_1, \rho_2, \rho_3]$  are fitted PF-specific parameters, gained from performing Monte Carlo simulations of SFR measurements of a turbid medium with a specified PF over a wide range of values of  $\mu'_s d_{fiber}$ . The resulting mathematical description in Eq. 3.2 lacked a defined input from metrics used to describe the PF distribution; therefore, a set of  $[\rho_1, \rho_2, \rho_3]$  were specific to a given PF, and it was not possible to estimate a different set for a different PF without re-performing the cumbersome simulation and fitting procedure. While Eq. 3.2 provides important insight into the PF-specific behavior of  $R_{SF}^o$  [2], that formulation of the expression has limited applicability to describe  $R_{SF}$  measured from biological tissues, a situation where the wavelength-dependent PF is unknown. This chapter directly addresses that limitation by introducing a form of  $[\rho_1, \rho_2, \rho_3]$  that depends on the PF-specific parameter  $\gamma$ ; this novel expression is then utilized to extract wavelength-dependent  $\mu'_s$  and  $\gamma$  from multiple measurements of the same medium with different  $d_{fiber}$ .

This study utilizes an experimentally validated Monte Carlo (MC) simulation code [2, 8] to emulate single fiber measurements of a homogeneous turbid medium. A range of optical properties were selected to be representative of biological tissue in the ultraviolet-visible wavelength region. Values for  $\mu'_s$  were selected by utilizing Mie theory to describe scattering, given as  $\mu'_s = a_1 (\frac{\lambda}{\lambda_0})^{-a_2}$ , where  $a_1$  and  $a_2$  represent the Mie scattering amplitude and power, respectively, and  $\lambda_0$  represents a normalization wavelength (chosen to be 800 nm in this chapter). Here,  $\mu'_s$  was calculated for  $\lambda \in [400 - 900]$  nm in 50 nm increments with  $a_2 = 1.0$  and  $a_1$  adjusted to calculate three different sets of scattering profiles, such that  $\mu'_s(800\text{nm}) = [0.5, 1.0, 2.0]$  mm<sup>-1</sup> respectively; this yielded 33  $\mu'_s$  values in total. Each individual  $\mu'_s$  value was constructed for three anisotropies ( $g_1 \in [0.8, 0.9, 0.95]$ ), using the Modified Henyey-Greenstein (MHG) expression,

$$p_{MHG}(\theta) = \alpha p_{HG}(\theta, g_{HG}) + (1 - \alpha) \frac{3}{4\pi} \cos^2(\theta), \quad (3.3)$$

where  $p_{MHG}(\theta)$  is the MHG PF, which is modeled [3] as a combination of the Henyey-Greenstein PF ( $p_{HG}(\theta, g_{HG})$ ), and a  $(1 - \alpha)$  fractional contribution of an isotropic scattering component. Eq. 3.3 was constructed such that the second Legendre moment of the PF was within a biologically relevant range, such that  $\gamma \in \{1.4, 1.5, 1.6, 1.7, 1.8, 1.9\}$  [3], by unique selection of  $\alpha$  and  $g_{HG}$ , which is the anisotropy for the HG component of Eq. 3.3. This resulted in 17 independent PFs (each with a unique  $\gamma$ - $g_1$  pair) for each  $\mu'_s$  value; note that a  $g_1 = 0.8, \gamma = 1.9$  combination is not possible with Eq. 3.3 [3]. Measurement of each optical property combination was simulated with  $d_{fiber} \in \{0.2, 0.4, 0.6, 0.8, 1.0\}$  mm. Each MC simulation tracked at least 2 million launched photons and returned the collected

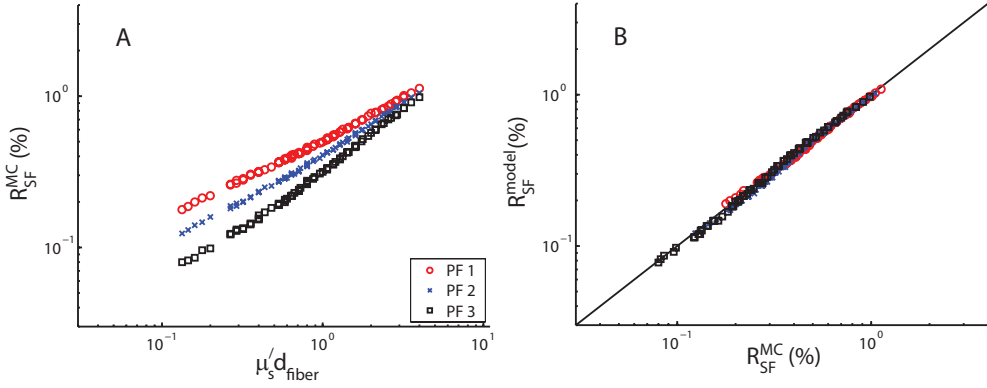


**Figure 3.1:** A)  $R_{SF}^0$  vs.  $\mu'_s d_{fiber}$  for 3 different PFs: PF 1  $g_1 = 0.8$ ,  $\gamma = 1.4$ ; PF 2  $g_1 = 0.9$ ;  $\gamma = 1.6$ ; PF 3  $g_1 = 0.95$ ,  $\gamma = 1.8$ . B) MC simulated  $\mu'_s d_{fiber}$  vs. model estimates.

light intensity. In total 2805  $R_{SF}^0$  values were extracted from the simulations, which yielded 2023 unique combinations of  $\mu'_s d_{fiber}$ ,  $g_1$ , and  $\gamma$ .

Figure 3.1A displays MC estimates of  $R_{SF}^0$  vs.  $\mu'_s d_{fiber}$  for three different PFs (see caption). These data show a PF-specific dependence of  $R_{SF}^0$  on  $\mu'_s d_{fiber}$ , with a stratification of  $R_{SF}^0$  between different PFs. For  $\mu'_s d_{fiber} < 10$ ,  $R_{SF}^0$  is increased for PFs with an increased percentage of large angle backscatter events (a factor associated with smaller  $g_1$  values or smaller  $\gamma$  values); the PF-specific stratification decreases in magnitude as  $\mu'_s d_{fiber}$  increases and approaches PF-independent behavior for  $\mu'_s d_{fiber} > 10$ ; this phenomenon was explained in detail previously [2]. These simulated  $R_{SF}^0$  data were used to identify a set of SF expressions that would replace the PF-specific fitted parameter set  $[\rho_1, \rho_2, \rho_3]$  noted in Eq. 3.2 with parameters expressed in terms of  $\gamma$ . This set was selected empirically from multiple candidates on the basis of fit quality and model simplicity,

$$[\rho_1 = \xi_1 \gamma^2 \quad \rho_2 = \xi_2 \gamma \quad \rho_3 = \xi_3 \gamma^2]. \quad (3.4)$$

Here the parameter set  $[\xi_1, \xi_2, \xi_3]$  represents PF-independent fitted coefficients; incorporation of Eq. 3.4 into Eq. 3.2 allows estimation of  $R_{SF}^0$  for a PF with PF specified  $\gamma$ . This set of equations was fit to minimize the sum squared error between model predictions and all 2805 MC estimates of  $R_{SF}^0$ , yielding fitted parameter values of  $[\xi_1 = 2.308 \pm 0.006, \xi_2 = 0.574 \pm 0.003, \xi_3 = 0.632 \pm 0.021]$ . Figure 3.1B shows the comparison of  $R_{SF}^0$  data estimated by the MC model vs. the corresponding model predictions; the model fit resulted in high quality predictions with a Pearson correlation coefficient of  $R = 0.997$  and a mean residual of  $< 5\%$ . Incorporation of the third and fourth moments of the PF into Eq. 3.4 did not significantly improve the model fit quality (data not shown). This insensitivity to higher order moments of the PF observed in this study is likely to be related to the exact form



of the MHG PF. This insensitivity may not persist for turbid media with a different form of the PF.

The revised formulation of Eq 3.2 accurately describes  $R_{SF}^0$  over a wide range of biologically relevant  $\mu'_s$  and PFs, and allows direct expression of  $R_{SF}^0$  for a PF by inputting  $\gamma$ . However, application of this expression to Eq 3.1 to model  $R_{SF}^0(\lambda)$  spectra measured in tissue is complicated because the PF in biological tissue is not well characterized and therefore difficult to specify *a priori*. While the wavelength-dependence of  $\mu'_s(\lambda)$  is well characterized (e.g. Mie and Rayleigh scattering), the wavelength-dependence of  $\gamma(\lambda)$  in biological tissue is unknown. Hence, a single  $R_{SF}^0(\lambda)$  spectrum measured in a turbid medium does not provide sufficient information to obtain wavelength-dependent estimates of both  $\mu'_s(\lambda)$  and  $\gamma(\lambda)$ ; such a fit is overparameterized and provides a non-unique solution. To address this limitation, we propose a novel approach to extract information about the wavelength-dependent  $\gamma(\lambda)$  values using multiple SFR measurements with different fiber diameters.

Figure 3.2 illustrates the use of such a multi-diameter SFR measurement approach, with the first example shown in the panels on the left column. Figure 3.2A(left) shows MC estimates of  $R_{SF}^0(\lambda)$  sampled by different  $d_{fiber} \in [0.2, 0.4, 0.6, 0.8, 1.0]$  mm in a turbid medium with  $\mu'_s(800) = 1 \text{ mm}^{-1}$ . In this situation,  $\gamma(\lambda)$  is specified to be constant across the full wavelength range as  $\gamma = 1.6$ . Scattering properties  $\mu'_s(\lambda)$  and  $\gamma(\lambda)$  specified in the MC model are visualized in the left panels of Figures 3.2B and C as the black line and symbols, respectively. Analysis of  $R_{SF}^0(\lambda)$  measured using multiple fiber diameters is conducted as a simultaneous multi-parameter fit that (I) estimates the Mie scattering parameters  $a_1$  and  $a_2$ , which provide a description of  $\mu'_s(\lambda)$  across the entire measured wavelength range, and (II) estimates  $\gamma(\lambda)$  at each individual wavelength. This fitting procedure utilizes the Levenberg-Marquardt algorithm to minimize the sum-squared error between measured and model estimated values of  $R_{SF}^0(\lambda)$ . The inset to Figure 3.2A(left) illustrates how the fit procedure generates a  $\gamma$ -specific  $R_{SF}^0(\lambda)$  vs.  $\mu'_s(\lambda)d_{fiber}$  profile at each  $\lambda$ ; these profiles are analogous to the  $\gamma$ -specific relationships displayed on Figure 3.1A. Simultaneous analysis of SFR spectra measured by all fiber diameters on the turbid medium displayed in Figure 3.2A yielded accurate model estimates of all collected reflectance values, as shown by the comparison of model with simulated  $R_{SF}^0(\lambda)$  values in Figure 3.2D(left), resulting in a Pearson correlation coefficient of  $R = 0.999$ . Importantly, the combined approach yields accurate estimates of both  $\mu'_s(\lambda)$  and  $\gamma(\lambda)$ , with a mean residual of each  $< 3.0\%$ ; the individual model estimates are displayed on the left panels of Figures 2B and C, respectively.

The example shown in the left column of Figure 3.2 shows accurate estimates of scattering properties, however,  $\gamma(\lambda)$  was specified to be constant at all wavelengths in the MC simulations. The right column investigates a more challenging scenario of a wavelength-dependent  $\gamma(\lambda)$ . Figure 3.2A(right) shows  $R_{SF}^0(\lambda)$  measured in a turbid

medium where  $\mu'_s(\lambda)$  is the same as given in Figure 3.2B(right), while  $\gamma(\lambda)$  is now specified as  $\gamma = 1.4$  for  $\lambda = [400 - 600]$  nm and  $\gamma = 1.8$  for  $\lambda = [650 - 900]$  nm. The change in  $\gamma(\lambda)$  is easily observable by the 'step' change visualized in the reflectance values displayed in Figure 3.2A(right). Here, a decrease in  $R_{SF}^0(\lambda)$  is associated with an increase in  $\gamma$ , and visa versa. Application of the multi-diameter SFR fitting procedure to these data highlights the wavelength-dependent estimation of  $\gamma(\lambda)$ , visualized by the inset of 3.2A(right), which again shows the PF-specific  $R_{SF}^0(\lambda)$  vs.  $\mu'_s(\lambda)d_{fiber}$  profiles; in this case distinct  $\gamma$ -specific profiles are evident at the 2 selected  $\lambda$  values. Application of the multi-diameter SFR approach again provides an accurate description of  $R_{SF}^0(\lambda)$  ( $R = 0.999$ ) while accurately estimating  $\mu'_s(\lambda)$  and  $\gamma(\lambda)$ , with a mean residual of  $< 3.0\%$  and  $< 1.0\%$ , respectively; agreement is visible in the right panels of Figures 3.2B and C. In this example, the specified 'step-change' of  $\gamma$  vs.  $\lambda$  is an exaggeration of more subtle changes that are expected to occur in the biological environment [5]. This example shows the ability of this method to correctly analyze collected reflectance spectra that contain substantial spectral features attributable to wavelength-variation of the PF.

The fitting procedures outlined in Figure 3.2 were repeated with noise introduced into  $R_{SF}^0(\lambda)$  at levels of [5, 10, 15]%. Analyzing both  $\lambda$ -dependent and  $\lambda$ -independent  $\gamma$  cases, the resulting mean residuals for  $\mu'_s(\lambda)$  were  $< [3.0, 5.0, 7.0]\%$  and for  $\gamma(\lambda)$  were  $< [3.0, 4.0, 6.0]\%$ , respectively; these results support the robustness of the multi-fiber diameter SFR approach in the presence of stochastic measurement noise.

The analysis presented in Figure 3.2 applies to SFR intensity in the absence of absorption,  $R_{SF}^0(\lambda)$ . Spectroscopic measurement of  $R(\lambda)$  allows estimation of  $R_{SF}^0(\lambda)$ , even in the presence of strong absorption, by application of Eq 3.1 and 3.2 in a spectral fitting procedure; this requires the specification of a wavelength-dependent function for  $\mu'_s(\lambda)$  as well as specification of a set of chromophores and their molecular extinction coefficients contributing to  $\mu_a(\lambda)$ .

Our envisioned technical implementation of the multi-fiber diameter SFR approach described in this chapter involves a coherent fiber bundle with an apparatus designed to control the diameter and location of a source-detector spot projected onto the fiber bundle. Such an approach would allow co-localization of SFR measurements with different fiber diameters while maintaining a small probe profile to facilitate incorporation into endoscopic or fine-needle based clinical procedures.

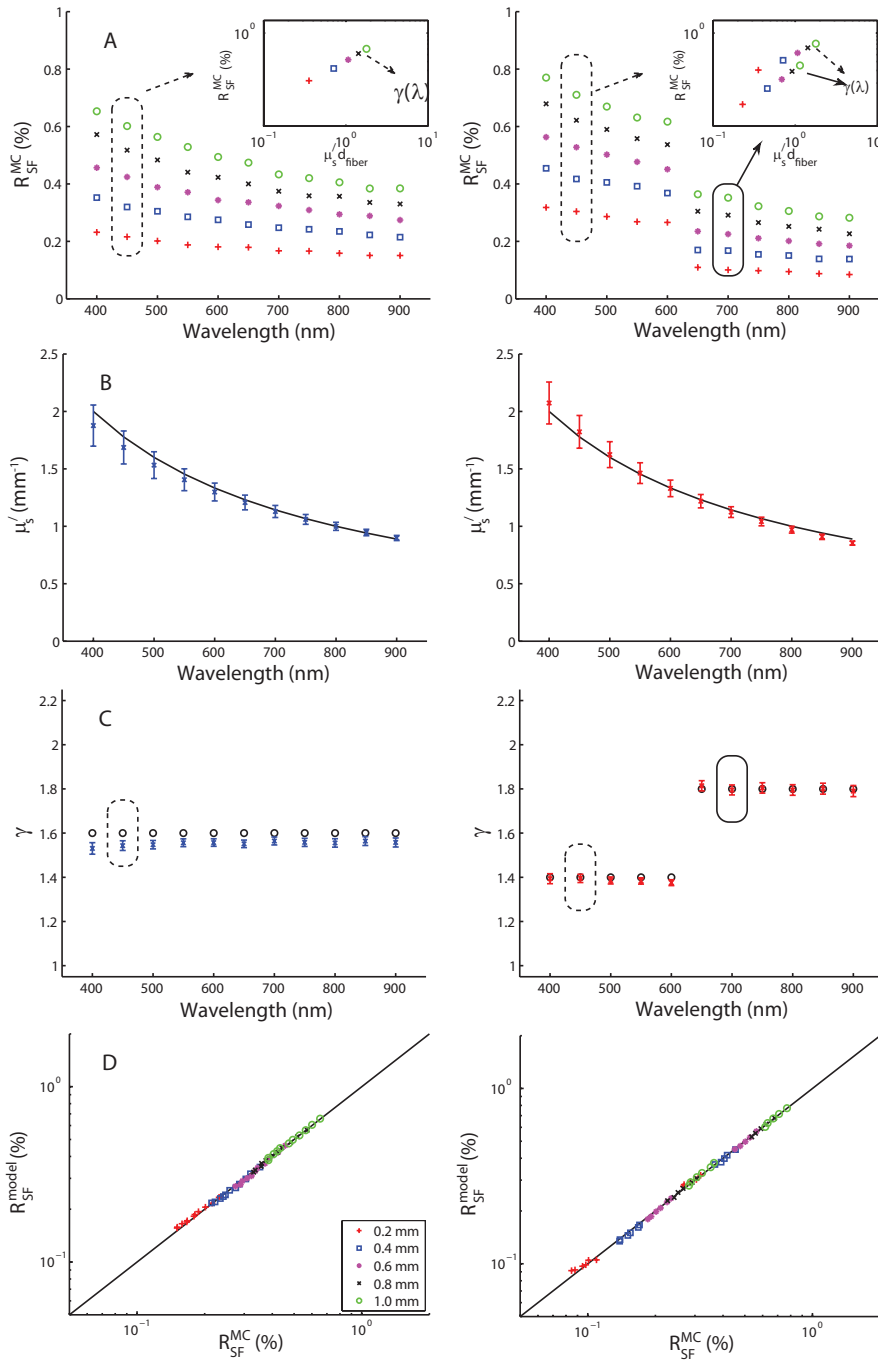


Figure 3.2: A)  $R_{SF}^O(\lambda)$  vs.  $\lambda$  measured by  $d_{fiber} \in [0.2, 0.4, 0.6, 0.8, 1.0]$  mm differentiated by symbols in legend. B)  $\mu'_s(\lambda)$  vs.  $\lambda$  specified in MC simulation and estimated by model. C)  $\gamma(\lambda)$  vs.  $\lambda$  specified in MC simulation and estimated by model. D)  $R_{SF}^O(\lambda)$  estimated by MC simulation vs. estimated by model. Left panels correspond to a wavelength-independent  $\gamma$ . Right panels correspond to wavelength-dependent  $\gamma$ .

## References

- [1] N N Boustany, S A Boppart, and V Backman. Microscopic Imaging and Spectroscopy with Scattered Light. *Annual Review of Biomedical Engineering*, 12:285–314, 2010.
- [2] S C Kanick, U A Gamm, M Schouten, H J C M Sterenborg, D J Robinson, and A Amelink. Measurement of the reduced scattering coefficient of turbid media using single fiber reflectance spectroscopy : fiber diameter and phase function dependence Abstract :. *Biomedical Optics Express*, 2(1):119–131, 2011.
- [3] F Bevilacqua and C Depeursinge. Monte Carlo study of diffuse reflectance at source–detector separations close to one transport mean free path. *Journal of the Optical Society of America A*, 16(12):2935–2945, 1999.
- [4] E L Hull and T H Foster. Steady-state reflectance spectroscopy in the P3 approximation. *Journal of the Optical Society of America A*, 18(3):584–599, 2001.
- [5] P Thueller, I Charvet, F Bevilacqua, M S Ghislain, G Ory, P Marquet, P Meda, B Vermeulen, and C Depeursinge. *In vivo* endoscopic tissue diagnostics based on spectroscopic absorption, scattering, and phase function properties. *Journal of Biomedical Optics*, 8:495, 2003.
- [6] A Amelink, D J Robinson, and H J M C Sterenborg. Confidence intervals on fit parameters derived from optical reflectance spectroscopy measurements. *Journal of Biomedical Optics*, 13:54044, 2008.
- [7] S C Kanick, H J M C Sterenborg, and A Amelink. Empirical model of the photon path length for a single fiber reflectance spectroscopy device. *Optics Express*, 17:860–871, 2009.
- [8] S C Kanick, D J Robinson, H J M C Sterenborg, and A Amelink. Monte Carlo analysis of single fiber reflectance spectroscopy. *Physics in Medicine and Biology*, 54:6991–7008, 2009.
- [9] P R Bargo, S A Prahl, and S L Jacques. Collection efficiency of a single optical fiber in turbid media. *Applied Optics*, 42(16):3187–3197, 2003.





# Chapter 4

## Measurement of tissue scattering properties using multi-diameter single fiber reflectance spectroscopy: *in silico* sensitivity analysis<sup>3</sup>

### Abstract

Multiple diameter single fiber reflectance (MDSFR) measurements of turbid media can be used to determine the reduced scattering coefficient ( $\mu'_s$ ) and a parameter that characterizes the phase function ( $\gamma$ ). The MDSFR method utilizes a semi-empirical model that expresses the collected single fiber reflectance intensity as a function of fiber diameter ( $d_{\text{fiber}}$ ),  $\mu'_s$ , and  $\gamma$ . This study investigated the sensitivity of the MDSFR estimates of  $\mu'_s$  and  $\gamma$  to the choice of fiber diameters and spectral information incorporated into the fitting procedure. The fit algorithm was tested using Monte Carlo simulations of single fiber reflectance intensities that investigated biologically relevant ranges of scattering properties ( $\mu'_s \in [0.4\text{--}4] \text{ mm}^{-1}$ ) and phase functions ( $\gamma \in [1.4\text{--}1.9]$ ) and for multiple fiber diameters ( $d_{\text{fiber}} \in [0.2\text{--}1.5] \text{ mm}$ ). MDSFR analysis yielded accurate estimates of  $\mu'_s$  and  $\gamma$  over the wide range of scattering combinations; parameter accuracy was shown to be sensitive to the range of fiber diameters included in the analysis, but not to the number of intermediate fibers. Moreover, accurate parameter estimates were obtained without *a priori* knowledge about the spectral shape of  $\gamma$ . Observations were used to develop heuristic guidelines for the design of clinically applicable MDSFR probes.

---

3 U. A. Gamm, S. C. Kanick, H. J. C. M. Sterenborg, D. J. Robinson, A. Amelink, **Measurement of tissue scattering properties using multi-diameter single fiber reflectance spectroscopy: *in silico* sensitivity analysis**, Biomed. Opt. Exp., Vol. 2:3150-3166 (2011)

## Introduction

Reflectance spectroscopy is a non-invasive method that is widely used to measure tissue optical properties. Such information can characterize vascular physiology and tissue ultrastructure, factors that may have diagnostic value [1, 2, 3]. Tissue optical properties are characterized by the absorption coefficient ( $\mu_a$ ) and the scattering coefficient ( $\mu_s$ ), which are the inverse of the mean free paths between absorption and scattering events, respectively, as well as the scattering phase function (PF), which describes the angular distribution of scattering events. Light transport at large distances from the light source (in biological tissues this is generally more than 2 mm) can be described by the reduced scattering coefficient, given as  $\mu'_s = \mu_s(1 - g_1)$ , where  $g_1 = \langle \cos(\theta) \rangle$  is the scattering anisotropy; light transport at these length scales in tissue is considered diffuse and is insensitive to the exact shape of the PF. However, reflectance intensities collected by optical devices with small source-detector separations contain contributions from non-diffuse photons, making the collected intensity dependent on both  $\mu'_s$  and the exact form of the PF [4, 5, 6, 7]. Failure to account for PF effects for small source-detector separations will introduce errors into optical property estimates. Previous investigations of light transport near the source [8, 9, 10, 11] utilized the Legendre moments of the PF to characterize the effect of large angle scattering events on the collected reflectance signal, introducing a parameter

$$\gamma = \frac{1 - g_2}{1 - g_1}, \quad (4.1)$$

that includes information about the first two moments of the PF, given as  $g_1$  and  $g_2$ , respectively. These first two moments correspond to the mean and the variance of the distribution of the angular scattering events specified by the PF. These mathematical approaches have been shown to be valid for source-detector separations that are greater than 0.5 mm [9].

Our group has focused on developing quantitative fiber optic devices that utilize a single optical fiber to deliver and collect light during measurement of a turbid medium, such as tissue. Light transport relevant to single fiber reflectance (SFR) measurements, where source and detector spots overlap, is not described by existing analytical models. Recently, our group introduced a semi-empirical model that describes the PF-dependent relationship between the collected SFR intensity and the dimensionless reduced scattering, a term given as the product of the reduced scattering coefficient and the fiber diameter ( $\mu'_s d_{fiber}$ ) [12]; from this relationship it is important to note that variations in  $\mu'_s$  and  $d_{fiber}$  interchangeably affect the collected light intensity. In a subsequent study, our semi-empirical model was further refined to characterize the PF-dependence of



the SFR intensity in terms of  $\mu'_s d_{fiber}$  and  $\gamma$  [13]. The application of this model to analyze SFR spectra measured in tissue is complicated because the tissue PF, and in turn  $\gamma$ , is not well characterized, and have been reported to be wavelength-dependent [10]. Our previous study [13] showed the potential of utilizing multiple SFR spectra measured by different fiber diameter probes to characterize the tissue scattering properties without any *a priori* information about the tissue PF. Specifically, a multi-diameter single fiber reflectance (MDSFR) approach utilizes the SFR intensity vs. fiber diameter profiles to inform independent estimation of the effects of  $\mu'_s$  and  $\gamma$  on the reflectance signal.

In the present study we characterize the sensitivity of MDSFR estimates of  $\mu'_s$  and  $\gamma$  on the fiber diameters included in the MDSFR approach and on constraints within the analysis algorithm. To investigate this, a Monte Carlo model was utilized to simulate SFR measurements over a wide range of scattering coefficients relevant for tissue ( $\mu'_s \in [0.4 - 4] \text{ mm}^{-1}$ ) [14, 15] and biologically relevant phase functions (Modified Henyey-Greenstein phase function with  $g_1 \in [0.8 - 0.95]$  and  $\gamma \in [1.4 - 1.9]$ ) [8], for 7 fiber diameters ( $d_{fiber} \in [0.2, 0.3, 0.4, 0.6, 0.8, 1.0, 1.5] \text{ mm}$ ). Simulated measurements are used to characterize the influence that the number of fibers and the range of fiber diameters included in the MDSFR analysis have on the accuracy of the estimated scattering parameters. Also, this study considers the potential benefit of *a priori* specification of wavelength-dependent scattering constraints on MDSFR accuracy.

## Materials and Methods

### *Single fiber reflectance model*

Figure 4.1 shows a schematic of the SFR spectroscopy setup. During measurement, photons are emitted from a white light source and guided through the single fiber probe to the fiber tip where they enter the medium under investigation. Within the medium photons are scattered and absorbed and a fraction of the photons is reflected back into the single fiber and collected by the spectrometer.

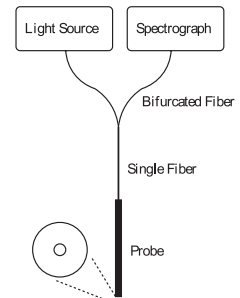


**Figure 4.1:** Single fiber reflectance spectroscopy setup

Quantitative analysis of a measured single fiber reflectance spectrum ( $R_{SF}$ ) requires the use of an empirical model that describes the wavelength-dependent collected light intensity in the absence of absorption ( $R_{SF}^0$ ), and applies a Modified Beer-Lambert law to that profile to account for absorption from tissue chromophores:

$$R_{SF} = R_{SF}^0 e^{-\mu_a \langle L_{SF} \rangle}. \quad (4.2)$$

Here,  $R_{SF}^0$  is the SFR intensity in the absence of absorption, and  $\langle L_{SF} \rangle$  is the effective SFR photon path length, which has a dependence on the sampled optical properties that has been fully characterized previously as [16, 17]:

$$\frac{\langle L_{SF} \rangle}{d_{fiber}} = \frac{C_{PF} 1.54}{(\mu'_s d_{fiber})^{0.18} (0.64 + (\mu_a d_{fiber})^{0.64})}, \quad (4.3)$$

where  $C_{PF}$  is a coefficient that describes the effect of phase function on  $\langle L_{SF} \rangle$ , described previously [16]. Recently, our group introduced a semi-empirical model [12, 13] that describes the relationship between  $R_{SF}^0$  and the dimensionless reduced scattering  $\mu'_s d_{fiber}$  and  $\gamma$ , given as:

$$R_{SF}^0 = \eta_{limit} \left( 1 + 0.63 \gamma^2 e^{-2.31 \gamma^2 (\mu'_s d_{fiber})} \right) \left[ \frac{(\mu'_s d_{fiber})^{0.57 \gamma}}{2.31 \gamma^2 + (\mu'_s d_{fiber})^{0.57 \gamma}} \right] \quad (4.4)$$

Here, the product of the terms preceding the square brackets represents the single fiber collection efficiency, where  $\eta_{limit}$  is the diffuse limit, which approximates to be 2.7% for a single fiber with NA = 0.22 [12, 18]. The term within the brackets describes the saturating relationship between  $R_{SF}^0$  and  $\mu'_s d_{fiber}$  that showed phase function independent behavior for high dimensionless scattering values ( $\mu'_s d_{fiber} \geq 10$ ) [12]. This expression accurately describes  $R_{SF}^0$  over a wide range of  $\mu'_s \in [0.4 - 4] \text{ mm}^{-1}$ , anisotropy  $g_1 \in [0.8 - 0.95]$ , and  $\gamma \in [1.4 - 1.9]$  for the Modified Henyey-Greenstein phase function.

### **Monte Carlo simulations of single fiber reflectance**

The Monte Carlo code utilized in this study is based on the MCML approach to stochastically simulate photon propagation within a turbid medium [19]. The code was adapted to mimic a single fiber measurement of a turbid medium with homogeneously distributed optical properties; this model has previously been described in detail [12, 16] and will here only be introduced briefly. Photons were initialized by selecting a location on the fiber face in contact with the medium and were launched into a direction within the fiber cone of acceptance; both location and direction were sampled from uniform distributions. The index of refraction  $n$  of the medium was set to 1.37 [20, 21] and that of

the fiber to 1.5. Reflection and refraction at the boundary between fiber face and medium were accounted for by using Fresnel's equation and Snell's law. The photons propagated through the medium in discrete steps selected from an exponential distribution that was weighted by the scattering coefficient. Each scattering event resulted in a change in propagation direction that was sampled from the user-specified scattering phase function. Simulations returned collected reflectance intensity (in the absence of absorption) in units of percentage of incident photons.

In this study the Monte Carlo model simulations were performed to mimic measurements of SFR spectra on turbid media that contain biologically-relevant scattering properties. While individual simulations return the equivalent of a measured intensity at a single wavelength, the range of optical properties within the set of simulations was selected such that combinations of individual simulations could be used to represent reflectance spectra measured in a turbid medium. For each group of simulations that represent a measured spectrum, the wavelength dependence of  $\mu'_s(\lambda)$  was assumed to follow Mie scattering, as

$$\mu'_s(\lambda) = a_1 \left( \frac{\lambda}{\lambda_0} \right)^{a_2}, \quad (4.5)$$

where  $a_1$  and  $a_2$  represent the Mie scattering amplitude and scattering power, respectively, and  $\lambda_0$  represents a normalization wavelength (chosen to be 800 nm in this study). Here,  $\mu'_s(\lambda)$  was calculated for  $\lambda \in [400 - 900]$  nm in 50 nm increments with  $a_2 = -1.0$  (which is typical for tissue [22]) and  $a_1$  adjusted to calculate three different sets of scattering profiles, such that  $\mu'_s(800\text{nm}) = [0.5, 1.0, 2.0] \text{ mm}^{-1}$  respectively; this yielded 33  $\mu'_s$  values in total. Figure 4.2 shows the 3 individual scattering sets utilized in this study.

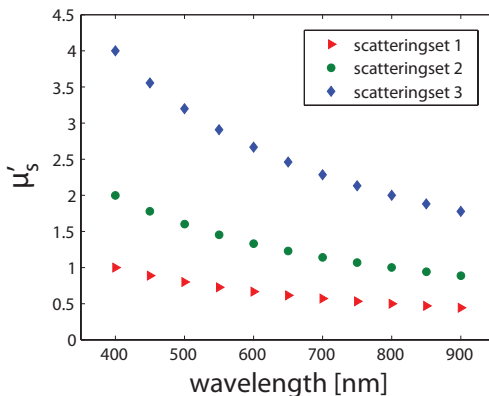


**Figure 4.2:** Wavelength dependent reduced scattering coefficient for the 3 scattering sets considered in simulations

Each  $\mu'_s$  value investigated in this study was constructed independently for 3 different anisotropies ( $g_1 \in [0.8, 0.9, 0.95]$ ) that were derived from the Modified Henyey-Greenstein (MHG) phase function:

$$p_{MHG}(\theta) = \alpha p_{HG}(\theta, g_{HG}) + (1 - \alpha) \frac{3}{4\pi} \cos^2(\theta). \quad (4.6)$$

The MHG phase function is a combination of the Henyey-Greenstein phase function ( $p_{HG}$ ) and an isotropic component that contains the  $\cos^2(\theta)$  term. By choosing specific values for  $g_{HG}$  and the normalization parameter  $\alpha$  the phase functions were constructed in a way that its second Legendre moment,  $g_2$ , led to values of  $\gamma$  that encompassed the biologically relevant range ( $\gamma \in [1.4, 1.5, 1.6, 1.7, 1.8, 1.9]$ ) as reported in previous literature [6]. In total 17 phase functions were implemented for all possible combinations of  $g_1$  and  $\gamma$  with the exception of  $g_1 = 0.8$  and  $\gamma = 1.9$ ; such a combination cannot be obtained with Eq. 4.6. SFR measurements of the 561 combinations of optical properties were each simulated for 7 different fiber diameters ( $d_{\text{fiber}} \in [0.2, 0.3, 0.4, 0.6, 0.8, 1.0, 1.5]$  mm) leading to a total amount of 3927 simulated SFR signals. Each simulation launched at least  $2 \times 10^6$  photons.

### ***Estimation of $\mu'_s$ and $\gamma$ from MDSFR measurements***

As reported previously [13], the MDSFR approach is based on the principle that SFR measurements of a turbid medium by multiple different fiber diameter probes will yield a PF-specific  $R_{SF}^0(\lambda)$  vs.  $d_{\text{fiber}}$  relationship (as visualized in Figure 4.3) that allows the estimation of both  $\mu'_s(\lambda)$  and  $\gamma(\lambda)$ . This theory applies to measurements at a single wavelength, assuming that the measurements are in the absence of absorption such that  $R_{SF}$  approximates to  $R_{SF}^0$ ; the application of Eq. 4.4 to the data will yield estimates of  $\mu'_s(\lambda)$  and  $\gamma(\lambda)$  at one selected wavelength if at least 3 fiber diameters are measured. However, analysis of measurements made in the presence of absorption necessitate the estimation of  $R_{SF}^0$  over the spectral wavelength range prior to application of Eq. 4.4, a calculation that requires specification of a wavelength-dependent function for  $\mu'_s(\lambda)$  as well as specification of a set of chromophores and their molecular extinction coefficients contributing to  $\mu_a(\lambda)$ , as will be discussed extensively in the discussion. One candidate background scattering model in tissue is the Mie scattering relationship given in Eq. 4.5 [23, 24]. Instead of fitting the values for  $\mu'_s$  and  $\gamma$  for each wavelength separately, the introduction of a background scattering model as a spectral constraint allows to fit  $R_{SF}^0(\lambda)$  data measured at multiple wavelengths and multiple fiber diameters simultaneously. In this case, the model Eq. 4.4 can be rewritten in a matrix representation, as:

$$R_{SF}^o(\lambda_i, d_{fiber}^j) = \eta_{limit} \left( 1 + 0.63\gamma_i^2 e^{-2.31\gamma_i^2 \left( a_1 \left( \frac{\lambda_i}{\lambda_0} \right)^{a_2} \right) d_{fiber}^j} \right) \left[ \frac{\left( \left( a_1 \left( \frac{\lambda_i}{\lambda_0} \right)^{a_2} \right) d_{fiber}^j \right)^{0.57\gamma_i}}{2.31\gamma_i^2 + \left( \left( a_1 \left( \frac{\lambda_i}{\lambda_0} \right)^{a_2} \right) d_{fiber}^j \right)^{0.57\gamma_i}} \right], \quad (4.7)$$

where  $i$  and  $j$  represent indices for sampled  $\lambda$  and  $d_{fiber}$ , and  $a_1$ ,  $a_2$  and  $\gamma_i$  are free fit parameters. For example, for a simulated MDSFR tissue measurement comprising 11 wavelengths  $\lambda_i$  and 7 fiber diameters  $d_{fiber}^j$  the data set consists of 77  $R_{SF}^o(\lambda_i, d_{fiber}^j)$  values and the model to which these data are fit (Eq. 4.7) contains 13 free fit parameters ( $a_1$ ,  $a_2$  and 11  $\gamma_i$  values). The MDSFR analysis algorithm estimates  $\mu'_s(\lambda)$  (or  $a_1$  and  $a_2$  in case of a spectrally constrained fit) and  $\gamma(\lambda)$  by minimizing the weighted residual error between the simulated and the model estimated  $R_{SF}^o(\lambda, d_{fiber})$  for all included fiber diameters (and all included wavelengths in case of a spectrally constrained fit) simultaneously. The fitting routine utilized a Levenberg-Marquardt algorithm coded into a Matlab script (version R2009, MathWorks). Confidence intervals of the estimated parameters were calculated from the square root of the diagonal of the covariance matrix, as described previously [25]. Note that an additional practical benefit gained from the spectrally resolved MDSFR analysis, is that the fit only requires 2 fiber diameters, as opposed to a minimum of 3 diameters if  $\mu'_s(\lambda)$  and  $\gamma(\lambda)$  are fitted at a single wavelength.

### ***MDSFR sensitivity analysis to fiber diameter set***

Simulated MDSFR measurements for each of the 561 combinations of scattering properties were utilized to determine the accuracy of  $\mu'_s(\lambda)$  and  $\gamma(\lambda)$  estimated at a single wavelength. In order to guide the design of the number and size of fibers to be included in MDSFR approach, the accuracy of parameter estimates were evaluated by systematically removing reflectance intensities corresponding to individual fibers from each MDSFR measurement at a single wavelength and calculating the resulting introduction of error. The accuracy of the fit was analyzed A) when the range of fiber diameters is decreased by subsequently removing data from larger fibers, B) when the range of fiber diameters is decreased by subsequently removing data from smaller fibers, and C) when intermediate fiber diameters are removed, while maintaining data from the largest and the smallest fiber diameters. In all 3 of the above cases, stochastic noise of 5% was introduced to the measured reflectance intensity data and the fit procedure was repeated 100 times; mean residual errors between model estimates and simulated values of  $\mu_s$  and  $\gamma$  (calculated as  $100\% \cdot \frac{|\mu_s^{sim} - \mu_s^{est}|}{\mu_s^{sim}}$  and  $100\% \cdot \frac{|\gamma^{sim} - \gamma^{est}|}{\gamma^{sim}}$ , respectively) as well as standard deviations calculated from repeated sets of error estimates are reported throughout this paper.

To investigate the application of the MDSFR approach to spectral measurements in tissue, a spectrally resolved MDSFR analysis was conducted in the presence of wavelength-dependent changes in  $\gamma(\lambda)$ . The relationship between  $\gamma$  and wavelength in tissue has not yet been elucidated and therefore cannot be informed by any set of specified spectral constraints; while wavelength-dependent changes are expected [10], the exact form of these changes is unknown. To consider how different wavelength-dependent changes in  $\gamma$  may influence the MDSFR performance, 3 different scenarios were analyzed: I) assuming  $\gamma(\lambda)$  constant over the wavelength range, II) assuming  $\gamma(\lambda)$  monotonically decreasing with wavelength, and III) assuming  $\gamma(\lambda)$  random for each wavelength. In case I analysis was performed for each of the 17 PF-specific scattering constructions of each of the 3 scattering sets, in case II  $\gamma$  was varied from 1.9 to 1.4, and  $g_1$  values varied in the set  $\in [0.95, 0.9, 0.8]$ , across the 400 – 900 nm wavelength range (with a 0.1 step decrease in  $\gamma$  per 100 nm, and a decrease in  $g_1$  introduced every 200 nm), and in case III 10 data sets were constructed with randomly selected  $\gamma$  and  $g_1$  values at each wavelength. These test scenarios were performed using information from all 7 fiber diameters. The influence of reducing fiber diameters on the spectrally resolved calculation (with a specific focus on the error associated with probes containing 2 fiber diameters) was performed with  $\gamma(\lambda)$  constant over the wavelength range.

## Results

### *Accuracy of single wavelength MDSFR analysis*

Figure 4.3a shows the SFR intensity vs. wavelength data for a MDSFR measurement with 7 fiber diameters (range 0.2 – 1.5 mm) on a turbid medium with  $\mu'_s = 1 \text{ mm}^{-1}$  at 800 nm (with the wavelength dependence of  $\mu'_s$  described by scattering set 2), with  $g_1 = 0.8$  and  $\gamma = 1.5$  at all wavelengths. Here, symbols differentiate between measurements made by different fiber diameters. These data represent SFR intensity measured in the absence of absorption ( $R_{SF}^0$ ). The MDSFR method utilizes the  $R_{SF}^0(\lambda)$  vs.  $d_{fiber}$  relationship measured at each individual wavelength to extract estimates for both  $\mu'_s(\lambda)$  and  $\gamma(\lambda)$ . Figure 4.3b shows the  $R_{SF}^0(\lambda)$  vs.  $d_{fiber}$  relationship at 800 nm; simulated data are fit to Eq. 4.4. MDSFR analysis yields estimates of reflectance intensity in good agreement with simulated data (visualized on the graph), and also yields estimates of  $\mu'_s(800\text{nm})$  and  $\gamma(800 \text{ nm})$ , which are respectively given as  $0.99 \text{ mm}^{-1}$  (true value of  $1.0 \text{ mm}^{-1}$ ) and 1.46 (true value of 1.5).

The MDSFR single wavelength analysis was applied to all simulated combinations of scattering properties. Figure 4.4 shows the comparison of estimated vs. simulated values for  $\mu'_s$  and  $\gamma$ ; these calculations utilized all 7 simulated fiber diameters in the MDSFR fitting

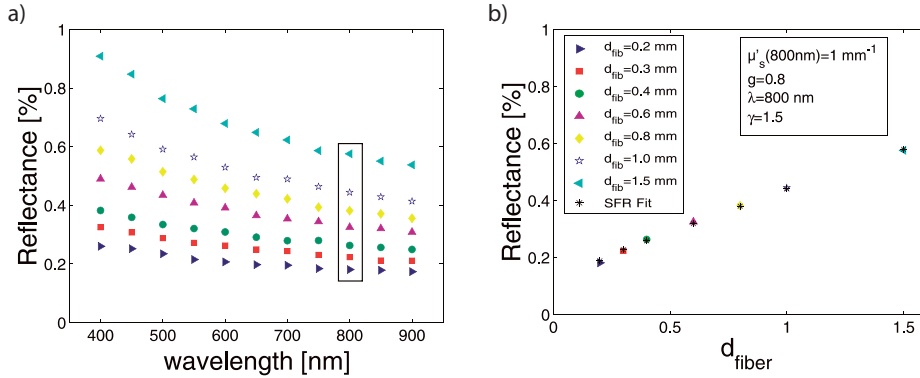


**Figure 4.3:** a) Simulated MDSFR reflectance measurements for 7 fiber diameters as a function of wavelength, and b) simulated and fitted reflectance at a single wavelength (800 nm) as a function of fiber diameter.

procedure. Here, both scattering parameters were accurately estimated over a wide range of reduced scattering coefficients ( $0.4 < \mu'_s < 4 \text{ mm}^{-1}$ ) and for all 17 phase functions and for all 11 wavelength ( $\lambda = [400 - 900 \text{ nm}]$ ) with an average mean residual error for  $\mu'_s$  of 4.9% and for  $\gamma$  of 2.5%.

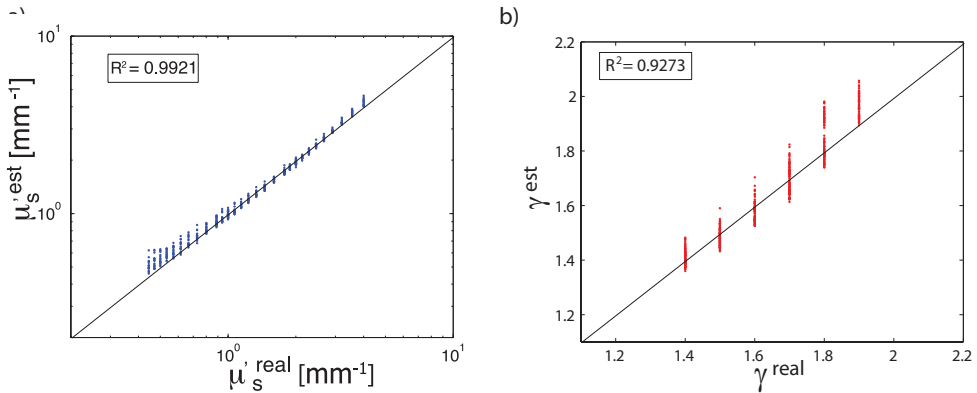


**Figure 4.4:** a) MDSFR estimated vs. simulated  $\mu'_s$ , and b) MDSFR estimated vs. simulated  $\gamma$  for the entire data set for all 11 wavelengths ( $\lambda = 400 - 900 \text{ nm}$ ). Calculations utilized 7 fiber diameters in the fitting procedure in the range  $d_{fiber} \in [0.2 - 1.5] \text{ mm}$ .

### Sensitivity of single wavelength MDSFR analysis to fiber diameter set

This study characterized the sensitivity of scattering parameter estimates to the fiber diameters included in the MDSFR analysis. In Figure 4.5 the abscissa of the graphs denotes the combinations of fiber diameters that contribute to the fitted MDSFR analysis and the ordinate denotes the mean residual error of either  $\mu'_s$  or  $\gamma$ . The four bars for each fiber

diameter combination denote the scattering ranges including scattering set 1 (range  $\mu'_s=[0.4 - 1] \text{ mm}^{-1}$ ), scattering set 2 (range  $\mu'_s=[0.9 - 2] \text{ mm}^{-1}$ ), scattering set 3 (range  $\mu'_s=[1.8 - 4] \text{ mm}^{-1}$ ) and the entire data set (Figure 4.2). The error bars display the standard deviation of the 100 repetitioned fits with a random noise of 5% introduced to the data.

Figures 4.5a and b show the influence of removing large fiber diameters from the 7 fibers included in the full MDSFR data set on the mean residual error in  $\mu'_s$  and  $\gamma$ , respectively. Conversely, Figures 4.5c and d display the effect of removing small fibers. The first set of columns in panels a-f show the case when all fibers are included into the fitting routine. It is observed that the mean residual error of  $\mu'_s$  is highest for scattering set 1 (lowest scattering); the error in  $\mu'_s$  estimation increases substantially for these low scattering coefficients when large fibers are subsequently removed from the dataset, as observed in Figure 4.5a. The effect of fiber removal on estimation of  $\gamma$  follows a similar trend (see Figure 4.5b). Alternatively, when small fibers are removed from the basis set of fibers included in the MDSFR fitting routine, the resulting mean residual error for  $\mu'_s$  approaches 12% for all scattering sets, as shown in Figure 4.5c; this error is substantially less than the case when larger fibers were removed, which depended on the magnitude of  $\mu'_s$  and approached 60% for the low scattering set (set 1). For the removal of small fibers, the mean residual error in  $\gamma$  increased for all data from 3% to 7%, and also showed an increased error associated with high scattering samples, given as scattering set 3; this is visualized in Figure 4.5d. Such a result is consistent with the understanding that measurements of SFR intensity in samples with high  $\mu'_s d_{fiber}$  become independent of  $\gamma$  [12].

Panels e and f of Figure 4.5 describe the influence of removing intermediate fiber diameters from the MDSFR fiber set. In this case each analysis retained fiber diameters of 0.2 and 1.5 mm, while differing quantities of the intermediate fibers were randomly removed. Inspection of panels e-f show a minimal influence of the removal of the intermediate fibers on MDSFR performance, with very minor changes to the mean error observed for either the entire data set or each individual scattering set. This behaviour was maintained when the simulated measurement noise level was increased from 5% to 10% or 20%; in these cases the mean residual error increased similarly for all fiber combinations and scattering sets (data not shown). These results indicate that the accuracy of  $\mu'_s$  and  $\gamma$  estimates are influenced by the range of diameters, and in turn the range of  $\mu'_s d_{fiber}$  included in the MDSFR analysis, and not the quantity of the intermediate fibers.



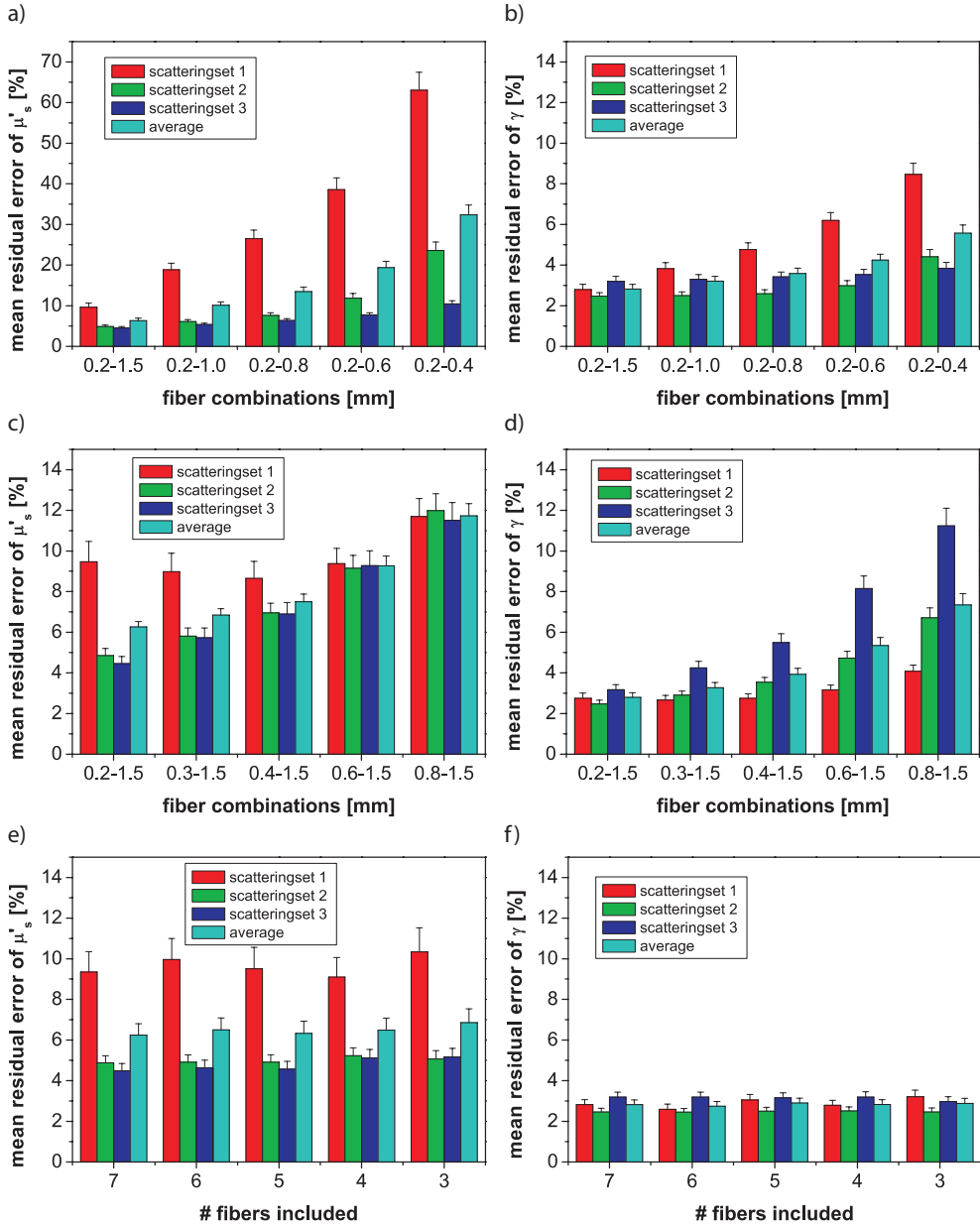


**Figure 4.5:** Effect of different fiber diameter combinations on the mean residual error of  $\mu'_s$  and  $\gamma$  estimated by single wavelength MDSFR analysis. a) and b) shows subsequent removal of large fibers; all remaining smaller fibers were included. c) and d) shows subsequent removal of small fibers; all remaining larger fibers were included. e) and f) shows removal of intermediate fibers; reflectance data from 0.2 mm and 1.5 mm fibers were always included. Note the difference in y-axis scale between panels a and b-f. Scattering set 1:  $\mu'_s = 0.4 - 1.0 \text{ mm}^{-1}$ ; scattering set 2:  $\mu'_s = 0.9 - 2.0 \text{ mm}^{-1}$ ; scattering set 3:  $\mu'_s = 1.8 - 4.0 \text{ mm}^{-1}$ .

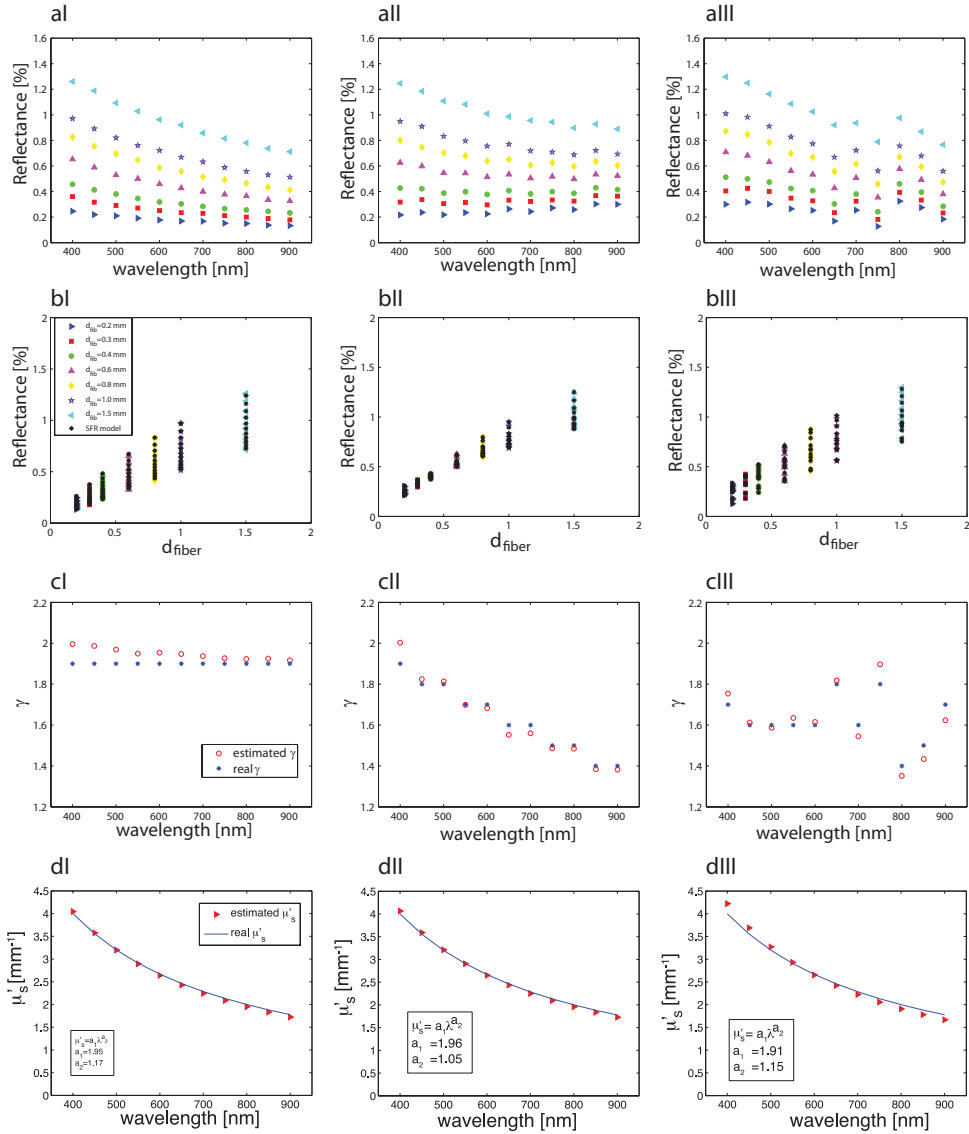


**Figure 4.6:** Example for spectrally resolved MDSFR fitting procedure using data from scattering set 3 ( $\mu'_s(800 \text{ nm}) = 2 \text{ mm}^{-1}$ ): a) simulated MDSFR intensities for 7 fiber diameters ( $d_{\text{fiber}} = [0.2, 0.4, 0.6, 0.8, 1, 1.5] \text{ mm}$ ), b) MDSFR intensity vs. fiber diameter for all wavelengths, c) estimated and simulated  $\gamma$  as a function of wavelength and d) estimated and simulated  $\mu'_s$  as a function of wavelength for I) wavelength independent  $\gamma$  and  $g_1$ , II) wavelength dependent  $\gamma$  and  $g_1$  and III) random  $\gamma$  and  $g_1$

### ***Accuracy of spectrally-resolved MDSFR analysis***

Figures 4.6a-I, -II and -III show  $R_{SF}^0(\lambda)$  vs. wavelength data for MDSFR measurements with 7 fiber diameters (range 0.2–1.5 mm) on a turbid medium with  $\mu'_s = 2 \text{ mm}^{-1}$  at 800 nm (with the wavelength dependence of  $\mu'_s$  described by scattering set 3). In Figure 4.6a-I,  $\gamma$  and  $g_1$  are constant across all wavelengths, with  $g_1 = 0.9$  and  $\gamma = 1.9$ . In Figure 4.6a-II, the specified PF varies across the 400 – 900 nm wavelength range, with  $\gamma$  varied from 1.9 to 1.4 and  $g_1$  values varied in the set  $\in [0.95, 0.9, 0.8]$ . In Figure 4.6a-III,  $g_1$  and  $\gamma$  were randomly selected for each wavelength. Figures 4.6b-I, -II and -III show  $R_{SF}^0$  vs. fiber diameter for these sets of MDSFR measurements. Application of the spectrally resolved MDSFR fitting method to these measurements yields estimates of reflectance intensity in good agreement with simulated data (visualized on the graph), leading to estimates of  $\gamma$  at each analyzed wavelength, and estimates of scattering model parameters  $a_1$  and  $a_2$  from Equation 4.7. The simulated and fitted wavelength profiles of  $\gamma(\lambda)$  and  $\mu'_s(\lambda)$  are displayed in Figures 4.6c and 4.6d, respectively.

To investigate the potential utility of the MDSFR approach to analyze spectral measurements in tissue, it is important to determine the influence that an unknown and potentially wavelength-dependent PF (and  $\gamma$ ) may have on the estimated scattering properties. The spectrally resolved MDSFR approach was evaluated on sets of MDSFR measurements with I)  $\gamma$  and  $g_1$  fixed, II)  $\gamma(\lambda)$  and  $g_1(\lambda)$  decreasing monotonically with wavelength, and III)  $\gamma(\lambda)$  and  $g_1(\lambda)$  completely randomized; details of these sets are described in details of these sets are described in the methods section. The results for these cases are shown in Figure 4.7. For all three cases both  $\mu'_s(\lambda)$  and  $\gamma(\lambda)$  were accurately estimated from the whole dataset, with mean residual errors of  $\leq 5\%$  for  $\mu'_s$  and of  $\leq 3\%$  for  $\gamma$ .

### ***Sensitivity of spectrally-resolved MDSFR analysis to fiber diameter set***

The sensitivity of the spectrally resolved MDSFR approach to the variation in the quantity and combination of fiber diameters was investigated. The error profiles resulting from the analysis, were similar to the error profiles presented for the single-wavelength MDSFR analysis in Figure 4.5 (data not shown). The novel aspect of investigating the sensitivity of the spectrally resolved MDSFR approach to fiber diameter set is the case involving 2 fiber diameters. In this analysis, pairs of fibers were considered with the the smallest fiber diameter specified for all pairs as 0.2 mm and the larger fiber selected from different diameters. The mean residual errors for this analysis are shown in Figure 4.8. Here, combinations of small fiber diameters are associated with increased error; this trend is substantially increased for measurements in the low scattering regime (set 1). Interestingly, measurements of the high scattering case (set 3) yielded accurate estimates

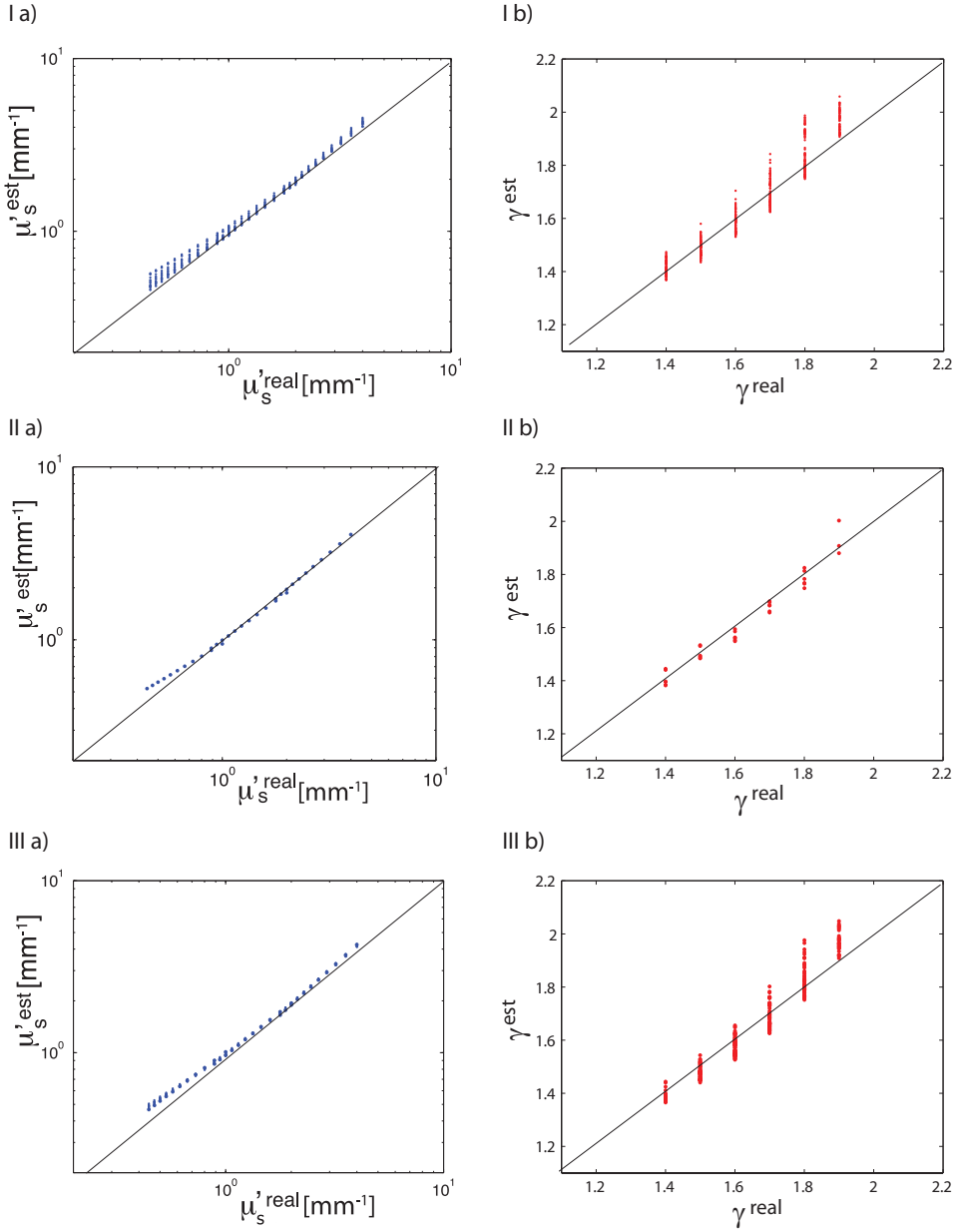


**Figure 4.7:** Spectrally resolved MDSFR fitting procedure: a) estimated vs. real  $\mu'_s$ ; b) estimated vs. real  $\gamma$  for I) wavelength independent  $\gamma$  and  $g_I$ , II) wavelength dependent  $\gamma$  and  $g_I$  and III) random  $\gamma$  and  $g_I$ . The analysis was performed over the whole dataset including all 3 scattering ranges and all 11 wavelengths ( $\lambda = 400 - 900$  nm).

even for measurements with the 0.2 and 0.3 mm fiber combination. These results highlight the finding that error in the estimated scattering properties is dependent on the range of dimensionless reduced scattering values included within the MDSFR analysis.

## Discussion

This study investigated the sensitivity of  $\mu'_s(\lambda)$  and  $\gamma(\lambda)$  estimated by MDSFR to the choice of fibers included in the analysis and to the incorporation of spectral information into the fitting algorithm. Results indicate that  $\mu'_s(\lambda)$  and  $\gamma(\lambda)$  estimates are sensitive to the range of fiber diameters but not the quantity of intermediate fibers. Results also show that the MDSFR approach does not require any *a priori* knowledge of the PF within the sampled medium.

### Influence of fiber diameters included in MDSFR analysis

This study investigated the influence of the number and diameter of fibers included in the MDSFR analysis on the accuracy of estimated scattering parameters. One unique aspect of the MDSFR analysis is that SFR intensity depends on  $\mu'_s d_{fiber}$ , an important factor that indicates that the theory can be applied interchangeably to different sets and combinations of fiber diameters. Results indicated that the accuracy of  $\mu'_s$  and  $\gamma$  estimates depends on the range of fiber diameters included in the analysis; specifically the range of  $\mu'_s d_{fiber}$  is important. This finding is supported by the high degree of accuracy in  $\mu'_s$  and  $\gamma$  estimates obtained from MDSFR analysis that included 7 fibers over the range of diameters [0.2 – 1.5] mm for all 3 scattering sets investigated (as shown in Figure 4.5). It is observed that reduction in the range of fibers introduced error, with substantial increases

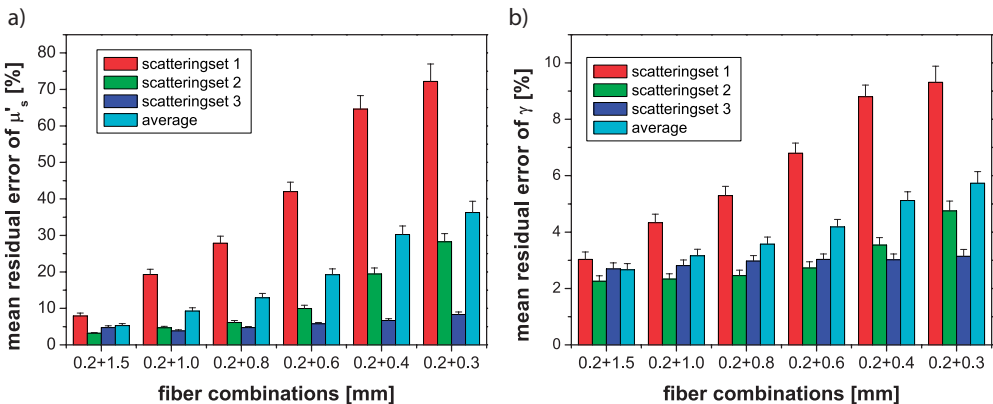


**Figure 4.8:** Sensitivity of spectrally resolved MDSFR estimates of a)  $\mu'_s$  and b)  $\gamma$  to the choice of fiber diameters within a 2 fiber MDSFR probe. Data from all 11 wavelengths ( $\lambda = 400 - 900$  nm) were included.

in error associated with measurement of small scattering coefficients by combinations of small diameter fibers (as evident in Figure 4.5a-b). Interestingly, the presence of intermediate fibers did not alter error in parameter estimates. These observations lead to the following heuristic guidelines: for tissues with medium to high scattering coefficients ( $\mu'_s > 1 \text{ mm}^{-1}$ ), an MDSFR measurement with a relatively limited number of small fiber diameters suffices to accurately extract  $\mu'_s$  and  $\gamma$ , while for tissues with low scattering coefficients ( $\mu'_s < 1 \text{ mm}^{-1}$ ) larger fiber diameter measurements need to be included in the data set to accurately extract  $\mu'_s$  and (to a lesser extent)  $\gamma$ . These heuristic guidelines can be used to evaluate the performance of potential MDSFR devices designed for specific clinical application areas, *e.g.* MDSFR devices compatible with endoscopic applications, where the largest allowable single fiber included in the MDSFR measurement is  $d_{\text{fiber}} < 2 \text{ mm}$ , or MDSFR devices compatible with Fine Needle Aspiration (FNA) procedures, where the MDSFR technique is performed through the lumen of an FNA needle and the largest single fiber included in the MDSFR measurement is  $d_{\text{fiber}} < 0.45 \text{ mm}$ . The sensitivity results indicate that for endoscopic applications,  $\mu'_s$  and  $\gamma$  can be extracted with an accuracy of better than 10% by using 0.2 mm and 1.5 mm fibers while employing a spectrally resolved MDSFR fitting procedure; it is possible to perform a wavelength independent assessment of  $\mu'_s$  and  $\gamma$  if intermediate fiber diameters are included in the MDSFR measurement. For FNA applications,  $\mu'_s$  and  $\gamma$  can be extracted with an accuracy of better than 20% and 10%, respectively, as long as  $\mu'_s > 1 \text{ mm}^{-1}$ . If  $\mu'_s < 1 \text{ mm}^{-1}$ , the accuracy in  $\mu'_s$  estimation reduces dramatically, while retaining the high accuracy of  $\gamma$  estimation. The clinical importance of the reported errors depends on the biology of the intended clinical application, *e.g.* on the difference between the scattering properties of healthy and (pre)malignant tissues.

### ***Assessment of model error***

Inspection of MDSFR estimates of  $\mu'_s$  and  $\gamma$  show increased error in the low dimensionless scattering regime, an increase that is attributable to model error. Inspection of the formulation of Eq. 4.4 shows two potential sources of error: first, the fitted coefficients reported in Eq. 4.4 were informed by a wide range of reduced scattering coefficients ( $[0.1 - 200] \text{ mm}^{-1}$ ), such that SFR data in the low  $\mu'_s d_{\text{fiber}}$  regime, where PF has the greatest influence on the SFR intensity, represented a subset of the total fitted parameter space [12]. Second, the characterization of the PF influence on SFR intensity was expressed concisely in terms of a single parameter  $\gamma$  [13]. While the resulting formulation of Eq. 4.4 yields high quality estimates of  $\mu'_s$  over a wide range of values, it is possible that higher order moments of the PF exclusively contribute to SFR intensity at low  $\mu'_s d_{\text{fiber}}$ . These model errors can be minimized by simulating measurements that resample the SFR intensity at low  $\mu'_s d_{\text{fiber}}$  values and re-evaluate the fitted coefficients in Eq. 4.4. However, such an analysis is beyond the scope of the current paper and will be the focus of future work.

### ***Comparison of MDSFR analysis at a single wavelength or multiple wavelengths: influence of absorption***

This study utilized two approaches to analyze MDSFR measurements: (1) a single wavelength MDSFR analysis, which extracts  $\mu'_s$  and  $\gamma$  independently for each wavelength; (2) a spectrally-resolved MDSFR analysis that utilizes prior knowledge of the wavelength dependence of  $\mu'_s$  as a constraint to fit  $\mu'_s$  and  $\gamma$  over a selected wavelength range. Comparison of sensitivity results from each method showed similar levels of accuracy in estimated parameter values; however, proper application of these methods to measurements of tissue requires careful consideration of the underlying assumptions.

The single-wavelength MDSFR analysis requires the measured reflectance intensity to be made in the absence of absorption; this is important because the influence of absorption on the SFR intensity will affect the reflectance measured by each fiber diameter differently, as SFR photon path length depends on the fiber diameter [16]. Note that the influence of absorption on SFR intensity cannot be resolved at a single wavelength. For measurements in tissue, the single wavelength MDSFR analysis may still be valid if performed at a wavelength where background absorption due to endogenous chromophores (*e.g.* blood) is minimal. Considering MDSFR measurements in tissue, containing vascular parameters of 2% blood volume fraction and 70% microvascular saturation, analysis at a wavelength of 800 nm would introduce only a 0.5% and 2.6% attenuation of the measured reflectance of the 0.2 mm and 1.5 mm fibers, respectively. This would result in only small increases of the error in estimation of  $\mu'_s$  and  $\gamma$  (from 6.0% to 6.2% and 2.57% to 2.63%, respectively). However, the associated error will depend on the actual blood content, oxygenation, wavelength as well as scattering coefficient; factors that cannot be resolved at a single wavelength.

The wavelength constrained MDSFR method can extract  $\mu'_s$  and  $\gamma$  values over the whole wavelength range even in presence of strong absorption. As we have described previously [16, 12, 17], the SFR spectrum in the presence of absorption  $R_{SF}$  in its most general form can be described by combining Eqs. 4.2-4.4:

$$R_{SF} = \eta_{limit}(1 + \rho_3 e^{(-\rho_1 \mu'_s d_{fiber})}) \left[ \frac{(\mu'_s d_{fiber})^{\rho_2}}{\rho_1 + (\mu'_s d_{fiber})^{\rho_2}} \right] e^{(-\mu_a^{tissue} \langle L_{SF} \rangle)}, \quad (4.8)$$

$$\langle L_{SF} \rangle = \frac{d_{fiber} C_{PF} 1.54}{(\mu'_s d_{fiber})^{0.18} (0.64 + (\mu_a d_{fiber})^{0.64})}. \quad (4.9)$$

Note that the general form of Eq. 4.4, which is valid for a wider range of phase functions than the MHG phase function utilized in this paper, contains phase function dependent parameters  $[\rho_1, \rho_2, \rho_3]$  and does not express these parameters in terms of  $\gamma$  [12]. Furthermore, the path length equation (Eq. 4.9) contains a phase function dependent constant  $C_{PF}$ . We have previously reported that substituting the parameter set  $[\rho_1, \rho_2, \rho_3, C_{PF}]$  by the values  $[6.82, 0.97, 1.55, 0.944]$  enables accurate extraction of  $\mu_a^{tissue}$  from SFR spectra measured in turbid media without *a priori* knowledge of either  $\mu'_s$  or phase function [17]. The tissue absorption coefficient  $\mu_a^{tissue}$  is the sum of the absorption coefficients of all the chromophores present in the interrogation volume, which can be written as:

$$\mu_a^{tissue} = \sum_k c_k \epsilon_k. \quad (4.10)$$

Here  $c_k$  and  $\epsilon_k$  are the concentration and extinction coefficient, respectively, of absorbing molecules (index  $k$ ) such as oxyhemoglobin, deoxyhemoglobin, bilirubin, beta-carotene, lipids and water. Note that Eq. 4.10 may be modified to contain correction factors for the inhomogeneous distribution of absorbing molecules such as blood [26]. Application of Eqs. 4.8 and 4.9 to SFR spectra measured by each independent fiber diameter returns estimates of  $c_k$  specific for each sampled fiber. While this calculation requires the specification of a background scattering model, it is important to note that the fit returns  $\mu_a^{tissue}$  independent of fitted scattering parameters. The resulting absorption coefficient estimates can be used to estimate reflectance spectra in the absence of absorption  $R_{SF}^0(d_{fiber})$ , as

$$R_{SF}^0(d_{fiber}) = \frac{R_{SF}(d_{fiber})}{e^{(-\mu_a^{tissue} \langle L_{SF} \rangle)}}. \quad (4.11)$$

Finally, the MDSFR fitting routine as described in the Methods can be applied to  $R_{SF}^0$  to obtain estimates for  $\mu'_s$  and  $\gamma$  over the whole wavelength range.

For the case where absorbers are distributed heterogeneously (e.g., layered tissue), the above calculation will allow fiber diameter specific estimation of  $\mu_a^{tissue}$ , that may be necessary due to slightly different sampled volumes between fiber diameters [16]; it is important to note that the MDSFR calculation assumes that scattering properties do not substantially differ between the sampled volume(s); the validity of this assumption will be investigated in future work.

We would like to emphasize that broadband MDSFR measurements of reflectance spectra of tissue in the ultraviolet-visible (UV-VIS) wavelength range will require spectrally resolved analysis that introduces spectral constraints regarding the form of wavelength-dependent changes in  $\mu'_s$ . Previous investigations that characterized  $\mu'_s$  vs. wavelength in the UV-VIS range in tissue identified the presence of a combination of Mie and Rayleigh



scattering that is sufficiently described by a power-law function. However, the specification of the background model structure is a potential limitation to the general use of the MDSFR technique, as the extracted scattering information is not allowed to deviate from the specified functionality; this constraint may prevent identification of subtle wavelength-dependent influences of scattering on the reflectance signal. The appropriateness of the background scattering model becomes increasingly important for MDSFR measurements made with very small fibers, including diameters smaller than those investigated in the current study, where the collected signal will contain an increasingly dominant non-diffuse component; these issues will be addressed in future studies.

## Conclusion

MDSFR provides a method to accurately determine both  $\mu'_s(\lambda)$  and the parameter characterized by the first two moments of the PF,  $\gamma(\lambda)$ , within a turbid medium; the approach was shown to be valid over a broad range of optical properties that are representative of biological tissue. Results presented in this study identified the sensitivity of MDSFR estimates to the range of optically sampled  $\mu'_s d_{fiber}$  and the insensitivity of model estimates to the quantity of intermediate fibers included in the analysis. Additionally, the MDSFR does not require any *a priori* knowledge of the wavelength-dependent changes in  $\gamma$ . These results indicate that the MDSFR approach can return a local quantitative assessment of  $\mu'_s$  that is independent of the tissue PF. This is a substantive improvement over many previous fiber optic approaches to estimating  $\mu'_s$  at small source-detector separations that did not elucidate the PF-influence on the collected reflectance [27, 28, 29, 30, 31, 32], and therefore, are likely to be less accurate in environments with unknown (or wavelength dependent) PF [4, 9, 7]. The MDSFR approach extracts information about both  $\mu'_s$  and the PF from reflectance intensities measured over multiple length scales, in the form of multiple fiber diameters; the basis of this approach is similar to the spatially-resolved method described previously by Bevilacqua *et al.* [6, 8]. Application of this approach to *in vivo* tissue may yield PF-information that provides novel insight into tissue morphology and ultrastructure; information that may have potential diagnostic utility [10].

This study utilized simulated data to identify heuristic rules to guide the design of MDSFR fiber probes for specific clinical applications. Studies are ongoing that will validate the approach by experimental measurement in optical phantoms. Further work will investigate the effect of inhomogeneous scattering distributions on MDSFR performance, and utilize the technique to characterize scattering properties in tissue *in vivo*.

## References

- [1] N N Boustany, S A Boppart, and V Backman. Microscopic Imaging and Spectroscopy with Scattered Light. *Annual Review of Biomedical Engineering*, 12:285–314, 2010.
- [2] R Drezek, M Guillaud, T Collier, I Boiko, A Malpica, C Macaulay, M Follen, and R R Richards-Kortum. Light scattering from cervical cells throughout neoplastic progression: influence of nuclear morphology, DNA content, and chromatin texture. *Journal of Biomedical Optics*, 8:7, 2003.
- [3] I Georgakoudi and J Van Dam. Characterization of dysplastic tissue morphology and biochemistry in Barrett’s esophagus using diffuse reflectance and light scattering spectroscopy. *Techniques in Gastrointestinal Endoscopy*, 7(2):100–105, 2005.
- [4] J R Mourant, J Boyer, A H Hielscher, and I J Bigio. Influence of the scattering phase function on light transport measurements in turbid media performed with small source-detector separations. *Optics Letters*, 21(7):546– 548, 1996.
- [5] M Canpolat and J R Mourant. High-angle scattering events strongly affect light collection in clinically relevant measurement geometries for light transport through tissue. *Physics in Medicine and Biology*, 45:1127, 2000.
- [6] F Bevilacqua and C Depeursinge. Monte Carlo study of diffuse reflectance at source–detector separations close to one transport mean free path. *Journal of the Optical Society of America A*, 16(12):2935–2945, 1999.
- [7] A Kienle, F K Forster, and R Hibst. Influence of the phase function on determination of the optical properties of biological tissue by spatially resolved reflectance. *Optics Letters*, 26(20):1571–1573, 2001.
- [8] F Bevilacqua, D Piguet, P Marquet, J D Gross, B J Tromberg, and C Depeursinge. *In vivo* local determination of tissue optical properties: applications to human brain. *Applied Optics*, 38(22):4939–4950, 1999.
- [9] E L Hull and T H Foster. Steady-state reflectance spectroscopy in the P3 approximation. *Journal of the Optical Society of America A*, 18(3):584–599, 2001.
- [10] P Thueler, I Charvet, F Bevilacqua, M S Ghislain, G Ory, P Marquet, P Meda, B Vermeulen, and C Depeursinge. *In vivo* endoscopic tissue diagnostics based on spectroscopic absorption, scattering, and phase function properties. *Journal of Biomedical Optics*, 8:495, 2003.
- [11] H Tian, Y Liu, L Wang, X Zhang, and Z Gao. Influence of high-order optical parameters of tissue on spatially resolved reflectance in the region close to the source. *Chinese Optics Letters*, 4(2):105–107, 2006.
- [12] S C Kanick, U A Gamm, M Schouten, H J C M Sterenborg, D J Robinson, and A Amelink. Measurement of the reduced scattering coefficient of turbid media using single fiber reflectance spectroscopy : fiber diameter and phase function dependence Abstract .: *Biomedical Optics Express*, 2(1):119–131, 2011.
- [13] S C Kanick, U A Gamm, H J C M Sterenborg, D J Robinson, and A Amelink. Method to quantitatively estimate wavelength-dependent scattering properties from multidiameter single fiber reflectance spectra measured in a turbid medium. *Optics Letters*, 36(15):2997–9, August 2011.

- [14] W F Cheong, S A Prah, and A J Welch. A review of the optical properties of biological tissues. *Quantum Electronics, IEEE Journal of*, 26(12):2166–2185, 1990.
- [15] E Salomatina, B Jiang, J Novak, and A N Yaroslavsky. Optical properties of normal and cancerous human skin in the visible and near-infrared spectral range. *Journal of Biomedical Optics*, 11:64026, 2006.
- [16] S C Kanick, D J Robinson, H J C M Sterenborg, and A Amelink. Monte Carlo analysis of single fiber reflectance spectroscopy. *Physics in Medicine and Biology*, 54:6991–7008, 2009.
- [17] S C Kanick, D J Robinson, H J C M Sterenborg, and A Amelink. Method to quantitate absorption coefficients from single fiber reflectance spectra without knowledge of the scattering properties. *Optics Letters*, 36(15):2791–3, August 2011.
- [18] P R Bargo, S A Prah, and S L Jacques. Collection efficiency of a single optical fiber in turbid media. *Applied Optics*, 42(16):3187–3197, 2003.
- [19] L Wang, S L Jacques, and L Zheng. MCML–Monte Carlo modeling of light transport in multi-layered tissues. *Computer Methods and Programs in Biomedicine*, 47(2):131–146, 1995.
- [20] A Knüttel and M Boehlau-Godau. Spatially confined and temporally resolved refractive index and scattering evaluation in human skin performed with optical coherence tomography. *Journal of Biomedical Optics*, 5:83, 2000.
- [21] J J J Dirckx, L C Kuypers, and W F Decraemer. Refractive index of tissue measured with confocal microscopy. *Journal of Biomedical Optics*, 10:44014–44018, 2005.
- [22] M Xu and R R Alfano. Fractal mechanisms of light scattering in biological tissue and cells. *Optics Letters*, 30(22):3051–3053, 2005.
- [23] F Bevilacqua, A J Berger, A E Cerussi, D Jakubowski, and B J Tromberg. Broadband absorption spectroscopy in turbid media by combined frequency-domain and steady-state methods. *Applied Optics*, 39(34):6498–6507, 2000.
- [24] J R Mourant, J P Freyer, A H Hielscher, A A Eick, D Shen, and T M Johnson. Mechanisms of light scattering from biological cells relevant to noninvasive optical-tissue diagnostics. *Applied Optics*, 37(16):3586–3593, 1998.
- [25] A Amelink, D J Robinson, and H J C M Sterenborg. Confidence intervals on fit parameters derived from optical reflectance spectroscopy measurements. *Journal of Biomedical Optics*, 13:54044, 2008.
- [26] R L P Van Veen, W Verkruysse, and H Sterenborg. Diffuse-reflectance spectroscopy from 500 to 1060 nm by correction for inhomogeneously distributed absorbers. *Optics Letters*, 27(4):246–248, 2002.
- [27] N Rajaram, T H Nguyen, J W Tunnell. Lookup table-based inverse model for determining optical properties of turbid media. *Journal of Biomedical Optics*, 13(5):050501, 2008.
- [28] G M Palmer and N Ramanujam. Monte Carlo-based inverse model for calculating tissue optical properties. Part I: Theory and validation on synthetic phantoms. *Applied Optics*, 45(5):1062–1071, 2006.
- [29] D Sharma, A Agrawal, L S Matchette, and T J Pfefer. Evaluation of a fiberoptic-based system for measurement of optical properties in highly attenuating turbid media. *Biomedical engineering online*, 5:49, January 2006.
- [30] R Reif, O A’Amar, and I J Bigio. Analytical model of light reflectance for extraction of the optical properties in small volumes of turbid media. *Applied Optics*, 46(29):7317–7328, 2007.

- [31] R H Wilson, M Chandra, J Scheiman, D Simeone, B McKena, J Purdy, and M-A Mycek. Optical spectroscopy detects histological hallmarks of pancreatic cancer. *Optics Express*, 17(20):17502–16, September 2009.
- [32] A Kim, M Roy, F Dadani, and B C Wilson. A fiberoptic reflectance probe with multiple source-collector separations to increase the dynamic range of derived tissue optical absorption and scattering coefficients. *Optics Express*, 18:5580–5594, 2010.





# Chapter 5

## Quantification of the reduced scattering coefficient and phase function dependent parameter $\gamma$ of turbid media using multi-diameter single fiber reflectance (MDSFR) spectroscopy: experimental validation<sup>4</sup>

### Abstract

MDSFR spectroscopy is a method that allows the quantification of  $\mu'_s$  and the phase-function-dependent parameter  $\gamma$  of a turbid medium by utilizing multiple fibers with different diameters. We have previously introduced the theory behind MDSFR and its limitations, and here we present an experimental validation of this method based on phantoms containing a fractal distribution of polystyrene spheres both in the absence and presence of the absorber Evans Blue.

---

4 U. A. Gamm, S. C. Kanick, H. J. C. M. Sterenborg, D. J. Robinson, A. Amelink, **Quantification of the reduced scattering coefficient and phase-function-dependent parameter  $\gamma$  of turbid media using multi-diameter single fiber reflectance spectroscopy: experimental validation**, Opt. Lett., 37:1838-1840 (2012)

Reflectance spectroscopy is a widely used method to measure tissue optical properties, including the absorption coefficient ( $\mu_a$ ) and reduced scattering coefficient ( $\mu'_s$ ), which contain information about the tissue vascular physiology and tissue morphology, respectively. Our group has recently investigated the use of single fiber reflectance (SFR) spectroscopy to quantify tissue optical properties. Previously, we reported a method to quantify  $\mu_a$  of a turbid medium in the absence of prior knowledge of the scattering properties [1]. Furthermore, we reported that the SFR intensity in the absence of absorption ( $R_{SF}^0$ ) follows a phase-function-specific dependence on the dimensionless reduced scattering ( $\mu'_s d_{fib}$ ), where  $d_{fib}$  is the fiber diameter), which is described by the following model equation [2, 3]:

$$R_{SF}^0 = \eta_{limit} \left( 1 + 0.63\gamma^2 e^{-2.31\gamma^2 \mu'_s d_{fib}} \right) \cdot \left[ \frac{(\mu'_s d_{fib})^{0.57\gamma}}{2.31\gamma^2 + (\mu'_s d_{fib})^{0.57\gamma}} \right]. \quad (5.1)$$

Here,  $\eta_{limit}$  is the diffuse limit of the single fiber (SF) collection efficiency, which is approximately 2.7% for an SF with NA=0.22 [2]. The parameter  $\gamma = \frac{1-g_2}{1-g_1}$  is a phase function (PF) dependent parameter that incorporates the first two Legendre moments of the PF,  $g_1$  and  $g_2$ , where  $g_1$  is the anisotropy. This expression accurately describes  $R_{SF}^0$  over a wide range of  $\mu'_s \in [0.4 - 4] \text{ mm}^{-1}$ ,  $g_1 \in [0.8 - 0.95]$ , and  $\gamma \in [1.4 - 1.9]$  for the Modified Henyey-Greenstein (MHG) PF, taken in the literature to be representative for tissue [4].

We recently introduced a new measurement concept called multi-diameter single fiber reflectance (MDSFR) spectroscopy, which allows the extraction of both  $\mu'_s$  and  $\gamma$  from turbid media [3]. In this method, multiple SFR measurements with different fiber diameters are performed sequentially (in a co-localized sampling volume) and the fiber-specific SFR spectra are fitted simultaneously to Eq. 5.1 to yield  $\mu'_s(\lambda)$  and  $\gamma(\lambda)$  over the measured wavelength range, assuming a power-law relationship for  $\mu'_s(\lambda)$ . Recently we investigated the limitations and the sensitivity of the MDSFR method based on an *in silico* analysis [5], which showed that  $\mu'_s$  and  $\gamma$  could be extracted with accuracies of better than 5% and 3%, respectively, for the wide range of scattering parameters investigated. In this chapter, we validate the method experimentally using optical phantoms containing a fractal distribution of polystyrene spheres, both in the absence and presence of an absorber.

Since Eq. 5.1, and therefore the MDSFR method, assumes that tissue PFs are well represented by the MHG PF, we aimed to construct a tissue phantom that features a PF closely mimicking the form of a MHG PF over the investigated wavelength range (400-900 nm). Previous research has shown that tissue-like PFs can be constructed using a fractal distribution of polystyrene spheres [6]. The PF of such a phantom can be calculated using Mie theory and can be controlled by varying the fractal dimension. To construct a phantom featuring a (Mie) PF closely resembling a MHG PF for all wavelengths, the optimal fractal



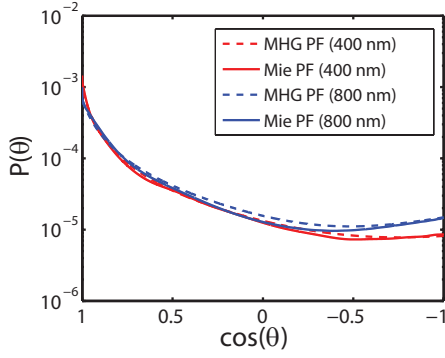


**Figure 5.1:** Calculated Mie PF at 400 nm (solid red) and 800 nm (solid blue) of the phantom containing a fractal distribution of 10 sizes of polystyrene spheres, and best-fit MHG PFs (dashed lines).

dimension of the sphere suspension was calculated by minimizing the sum of the squared error between the MHG PF and the calculated Mie PF of the sphere suspension for all angles, for wavelengths between 400 and 900 nm in 50 nm intervals. We found that for a suspension containing 10 different sphere sizes ( $d_{sphere} = [0.11, 0.15, 0.21, 0.39, 0.50, 0.79, 1.01, 4.76, 10.09, 20.28] \mu\text{m}$ ), a fractal dimension of 4.1 yielded the best correlation between the true (Mie-calculated) PF and best-fit MHG PFs ( $R^2(400\text{-}900 \text{ nm}) = [0.987 - 0.995]$ ). Figure 5.1 shows the Mie PF of the phantom for 2 different wavelengths, along with their best-fit MHG PFs. The resulting polybead phantom had a Mie-calculated anisotropy of  $g_l$  ranging from 0.64 to 0.7, and  $\gamma$  ranging from 1.47 to 1.63 between 400 and 900 nm. The  $g_l$  and  $\gamma$  values of the best-fit MHG PFs did not deviate by more than 5% and 1.7%, respectively, from their Mie-PF counterparts for any wavelength. The concentrations of the spheres were chosen such that  $\mu'_s(\lambda)$  followed a power-law relationship ranging from  $0.4 \text{ mm}^{-1}$  at 900 nm to  $3.0 \text{ mm}^{-1}$  at 400 nm.

SFR measurements of the phantom containing polybeads (Polybead Microspheres, Polysciences, Eppelheim, Germany) were performed with 5 different fiber diameters ( $d_{fiber} = [0.2, 0.4, 0.6, 0.8, 1.0] \text{ mm}$ ). Furthermore, to calibrate the system, measurements were performed in a calibration phantom containing 20%-Intralipid as a scatterer, diluted to yield  $\mu'_s(800 \text{ nm}) = 1.2 \text{ mm}^{-1} (I_{IL}^{cal})$ , and in a dark container filled with water ( $I_{water}$ ). The absolute SFR signals (in % of incident photons) of the phantom were then calculated for each fiber diameter as:

$$R_{SF}^0 = I_{IL}^{sim} \left( \frac{(I_{phantom} - I_{water})}{(I_{IL}^{cal} - I_{water})} \right). \quad (5.2)$$

Here,  $I_{phantom}$  is the signal of the polybead phantom, and  $I_{IL}^{sim}$  is the absolute SFR signal (in % of incident photons) obtained by Monte Carlo (MC) simulations of the Intralipid calibration phantom. The MC simulations were performed as described in detail previously [2,8] for all fiber diameters and for wavelengths ranging from 400 nm to 900 nm in 10 nm

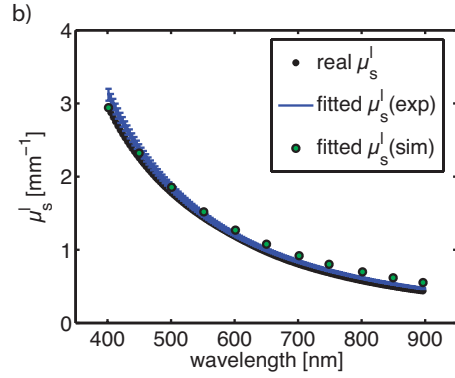
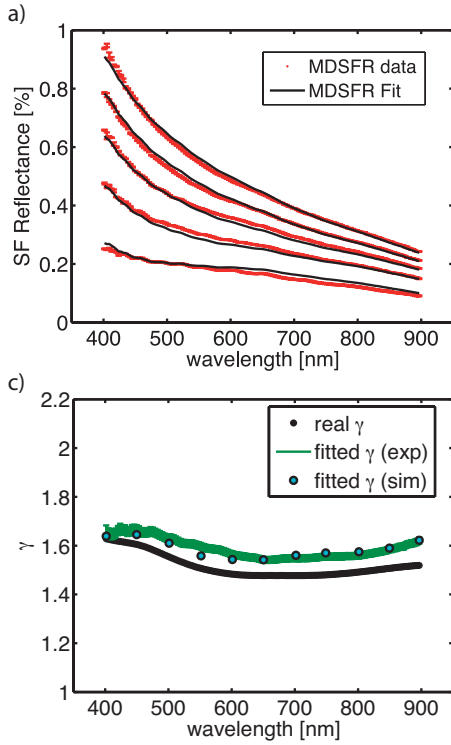


**Figure 5.2:** Results of the MDSFR analysis: a) SFR spectra for 5 fiber diameters (red) and MDSFR fitted reflectance (black). b) real  $\mu'_s$  (black) and estimated  $\mu'_s$  from experimental data (blue) and simulated data (green dots). c) real  $\gamma$  (black) and estimated  $\gamma$  from experimental data (green) and simulated data (light blue dots).

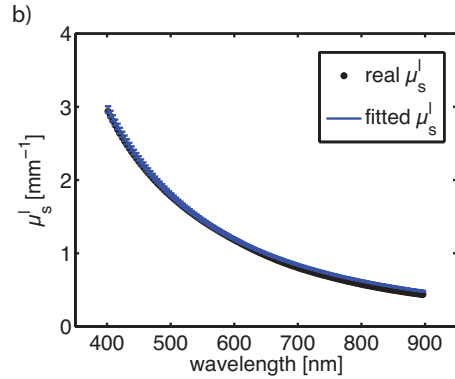
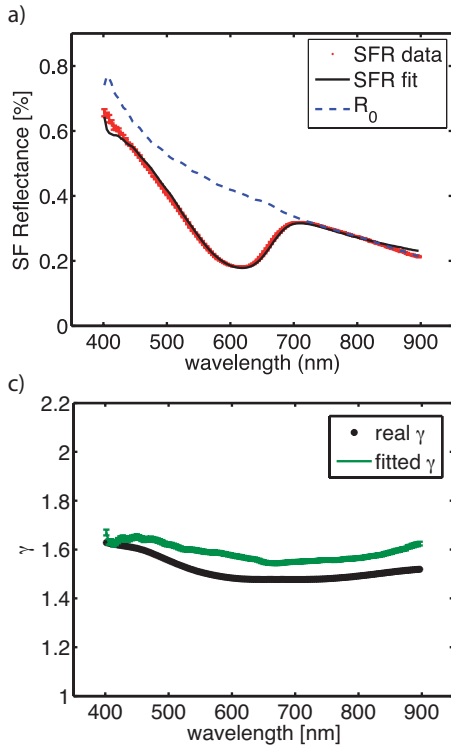


**Figure 5.3:** Results of the MDSFR analysis after adding Evans Blue as absorber. a) SFR spectrum for  $d_{fib} = 0.8$  mm (red), fitted SFR spectrum (black) and calculated  $R_{SF}^0$  spectrum. b) real  $\mu'_s$  (black) and estimated  $\mu'_s$  from experimental data (blue). c) real  $\gamma$  (black) and estimated  $\gamma$  from experimental data (green).

intervals. The refractive index of the medium was set to 1.33 and the wavelength-specific PFs and  $\mu'_s$  values were calculated from Michels *et al.* [7]. Each MC simulation launched 20 million photons. Linear interpolation was used to calculate  $I_{LL}^{sim}$  for wavelengths that were not simulated.

MDSFR analysis of the 5 calibrated SFR spectra was performed as described previously [3, 5]. Figure 5.2a shows the SFR spectra from each of the 5 fiber diameters and the resulting MDSFR fit, which is well-correlated ( $R^2 = 0.996$ ). The MDSFR-fitted values and true values for  $\mu'_s$  and  $\gamma$  are shown as a function of wavelength in Figures 5.2b and c, respectively. It is observed that  $\mu'_s$  is accurately fitted over the entire wavelength range; the mean error between the estimated and real  $\mu'_s$  is 5.5%, which is in good agreement with our previous *in silico* results [5]. Although the mean error in  $\gamma$  is also relatively low (4.8%), it is higher than expected from our *in silico* analysis (3%). Moreover, in contrast to our *in silico* MDSFR results, a systematic overestimation of  $\gamma$  across the wavelength range is observed in our experiment. This systematic overestimation is not caused by an experimental error, but rather by a mismatch in the PF of the polybead phantom compared to the PF used to construct model Eq. 5.1 [2]. Although the polybead Mie PF approximates the shape of a MHG PF very well, the  $g_1$  and  $g_2$  of the polybead Mie PF are much smaller than those of the MHG PFs that were used to construct the model. Specifically, the anisotropy of the simulated MHG PFs used to inform the model Eq. 5.1 were  $g_1 = [0.8, 0.9, 0.95]$ , while the anisotropy of the polybead phantom was much lower with  $g_1$  ranging between 0.6 and 0.7. This discrepancy in PF moments is likely to cause deviations in the estimation of  $\gamma$ . To validate this hypothesis, we performed MC simulations of the polybead phantom and repeated the MDSFR analysis on this *in silico* data set. MC simulations were performed in 50 nm intervals using the Mie-calculated wavelength-specific PFs and  $\mu'_s$  values of the polybead phantom following Gélébart *et al* [6]. The MDSFR-fitted values for  $\mu'_s$  and  $\gamma$  for this simulated data set are overplotted in Figures 5.2b and c, respectively. The systematic overestimation of  $\gamma$ , observed in our experiment, is reproduced in our MC simulated dataset, thus proving our hypothesis.

The goal of the MDSFR method is to measure scattering properties of tissue *in vivo*. Here, absorption of light due to the presence of chromophores may complicate the extraction of  $\mu'_s$  and  $\gamma$  (since the MDSFR method is based on SFR spectra calculated in the absence of absorption). Theoretically, the MDSFR method can extract  $\mu'_s$  and  $\gamma$  even in the presence of strong absorption, following the method described in detail in [5]. In short, this approach assumes that the attenuation of the SFR signals ( $R_{SF}$ ) due to absorption can be described by an exponential term, based on the Lambert-Beer law, as  $R_{SF} = R_{SF}^0 \cdot e^{-\langle L_{SF} \rangle \mu_a}$ . The dependence of SF pathlength  $\langle L_{SF} \rangle$  on optical properties, as well as the fitting routine used to extract  $\mu_a$  from an SFR spectrum without prior knowledge of the scattering properties, are described in detail in previous work [8, 1]. After extracting  $\mu_a$

from each SFR spectrum individually,  $R_{SF}^0$  can be readily calculated using the Lambert-Beer law. The MDSFR method is then applied to the  $R_{SF}^0$  spectra to extract  $\mu'_s$  and  $\gamma$ .

We experimentally validated this approach by adding Evans Blue to the phantom, resulting in a maximum  $\mu_a=1 \text{ mm}^{-1}$  at 611 nm. An example of a single SFR spectrum (measured with  $d_{fb}=0.8 \text{ mm}$ ) in the presence of the absorber,  $R_{SF}$ , is shown in Figure 5.3a (red curve), along with the fit (black line) and the resulting calculated  $R_{SF}^0$  spectrum (dashed blue line). The calculated  $R_{SF}^0$  agrees well with the measured  $R_{SF}^0$  of the 0.8 mm fiber in the absence of absorption, see Figure 5.2a. The estimated  $\mu'_s$  and  $\gamma$  values resulting from MDSFR analysis of the 5 (absorption corrected)  $R_{SF}^0$  spectra are shown in Figure 5.3b and c, respectively. The results are identical to the results of the phantom measurements without the absorber, demonstrating the capability of MDSFR to measure  $\mu'_s$  and  $\gamma$  in the presence of (strong) absorption.

The data presented in this study provide the first experimental validation of the MDSFR method. Results show that  $\mu'_s$  can be extracted accurately from an MDSFR measurement of a turbid medium, even in the presence of strong absorbers. Results also show that the extracted  $\gamma$  values are sensitive to the absolute values of  $g_1$  and  $g_2$ . Unfortunately, we have not found a way to construct a phantom that has a PF that mimicks the MHG PF and has  $g_1$  and  $g_2$  values in the range used to inform the SFR model Eq. 5.1. The accuracy of  $\gamma$  estimation in tissues will also depend on the actual shape of the tissue PF and its first and second (and possibly higher order) moments; information that is currently unknown to the best of our knowledge. Future studies will address this issue by investigating the sensitivity of  $\gamma$  estimation to more complicated PFs than the MHG. In addition, we are currently planning *in vivo* MDSFR experiments to measure differences in  $\mu'_s$  and  $\gamma$  between normal and tumor tissues.

## References

- [1] S C Kanick, D J Robinson, H J C M Sterenborg, and A Amelink. Method to quantitate absorption coefficients from single fiber reflectance spectra without knowledge of the scattering properties. *Optics Letters*, 36(15):2791–3, August 2011.
- [2] S C Kanick, U A Gamm, M Schouten, H J C M Sterenborg, D J Robinson, and A Amelink. Measurement of the reduced scattering coefficient of turbid media using single fiber reflectance spectroscopy : fiber diameter and phase function dependence Abstract :. *Biomedical Optics Express*, 2(1):119–131, 2011.
- [3] S C Kanick, U A Gamm, H J C M Sterenborg, D J Robinson, and A Amelink. Method to quantitatively estimate wavelength-dependent scattering properties from multidiameter single fiber reflectance spectra measured in a turbid medium. *Optics Letters*, 36(15):2997–9, August 2011.
- [4] F Bevilacqua and C Depeursinge. Monte Carlo study of diffuse reflectance at source–detector separations close to one transport mean free path. *Journal of the Optical Society of America A*, 16(12):2935–2945, 1999.
- [5] U A Gamm, S C Kanick, H J M C Sterenborg, D J Robinson, and A Amelink. Measurement of tissue scattering properties using multidiameter single fiber reflectance spectroscopy: *in silico* sensitivity analysis. *Biomedical Optics Express*, 2(11):3150–66, November 2011.
- [6] B Gélébart, E Tinet, J M Tualle, and S Avrillier. Phase function simulation in tissue phantoms: a fractal approach. *Pure and Applied Optics: Journal of the European Optical Society Part A*, 5:377–388, 1996.
- [7] R Michels, F Foschum, and A Kienle. Optical properties of fat emulsions. *Optics Express*, 16:5907–5925, 2008.
- [8] S C Kanick, D J Robinson, H J M C Sterenborg, and A Amelink. Monte Carlo analysis of single fiber reflectance spectroscopy. *Physics in Medicine and Biology*, 54:6991–7008, 2009.



# Chapter 6

## *In vivo* quantification of the scattering properties of tissue using multi-diameter single fiber reflectance spectroscopy<sup>5</sup>

### Abstract

Multi-diameter single fiber reflectance (MDSFR) spectroscopy is a non-invasive optical technique based on using multiple fibers of different diameters to determine both the reduced scattering coefficient ( $\mu'_s$ ) and a parameter  $\gamma$  that is related to the angular distribution of scattering, where  $\gamma = \frac{1-g_2}{1-g_1}$  and  $g_1$  and  $g_2$  are the first and second moment of the phase function, respectively. Here we present the first *in vivo* MDSFR measurements of  $\mu'_s(\lambda)$  and  $\gamma(\lambda)$  and their wavelength dependence. MDSFR is performed on nineteen mice in four tissue types including skin, liver, normal tongue and in an orthotopic oral squamous cell carcinoma. The wavelength-dependent slope of  $\mu'_s(\lambda)$  (scattering power) is significantly higher for tongue and skin than for oral cancer and liver. The reduced scattering coefficient at 800 nm of oral cancer is significantly higher than of normal tongue and liver.  $\gamma(\lambda)$  generally increases with increasing wavelength; for tumor it increases monotonically with wavelength, while for skin, liver and tongue  $\gamma(\lambda)$  reaches a plateau or even decreases for longer wavelengths. The mean  $\gamma(\lambda)$  in the wavelength range 400-850 nm is highest for liver ( $1.87 \pm 0.07$ ) and lowest for skin ( $1.37 \pm 0.14$ ).  $\gamma(\lambda)$  of tumor and normal tongue falls in between these values where tumor exhibits a higher average  $\gamma(\lambda)$

---

5 F. van Leeuwen van Zaane, U.A. Gamm, P.B.A.A. van Driel, T.J.A. Snoeks, H.S. de Bruijn, A. van der Ploeg van den Heuvel, I.M. Mol, C.W.G.M. Lwik, H.J.C.M. Sterenborg, A. Amelink, D.J. Robinson, *In vivo* quantification of the scattering properties of tissue using multidiameter single fiber reflectance spectroscopy, Biomed. Opt. Exp., 4: 696-708 (2013)

$(1.72 \pm 0.09)$  than normal tongue  $(1.58 \pm 0.07)$ . This study shows the potential of using light scattering spectroscopy to optically characterize tissue *in vivo*.

## Introduction

Reflectance spectroscopy is frequently used to determine the absorption and scattering coefficients of biological tissue. A range of fiber-optic devices with different probe geometries have been developed to retrieve these optical properties, within various regimes of tissue-light propagation [1, 2, 3]. The absorption coefficient of tissue is related to physiological parameters such as micro-vascular blood oxygenation, blood volume fraction and microvessel diameter, as well as to the concentration of chromophores such as bilirubin and cytochrome C. Scattering in tissue results from variations in refractive index between the various cell and tissue components and their surroundings. At large source-detector separations, light transport can be considered diffuse and is therefore only dependent on the absorption coefficient ( $\mu_a$ ) and the reduced scattering coefficient ( $\mu'_s$ ), given by  $\mu'_s = \mu_s(1-g_1)$  where  $g_1 = \langle \cos(\theta) \rangle$  is the first moment of the scattering phase function (PF), also called the scattering anisotropy. At these large distances, light transport is insensitive to the exact shape of the PF. However, in device configurations with small source-detector separations, an additional, PF dependent variable  $\gamma$  is necessary to describe the effect of large angle scattering events on the reflectance signal [4, 5, 6, 7]. This parameter  $\gamma$  is defined as

$$\gamma = \frac{1 - g_2}{1 - g_1}, \quad (6.1)$$

where  $g_2$  is the second Legendre moment of the PF [5]. Our group has previously developed single fiber reflectance spectroscopy (SFR), where one fiber serves as both source and detector. One advantage of this geometry is that SFR is sensitive to superficial tissues and their microvasculature, which are susceptible to early changes in morphology caused by (pre-)malignant disease. Furthermore, the diameter of a single fiber probe is such that it can be easily guided through the working channel of an endoscope to sample internal organs. The analysis of SFR spectra is performed using a semi-empirical model (cf. Eq.6.2) that describes the PF-dependent relationship between SFR signal and the dimensionless reduced scattering (which is defined as the product of the reduced scattering coefficient and the fiber diameter  $\mu'_s d_{fib}$ ) [6]. This semi-empirical model was based on Monte-Carlo simulations and validated in tissue mimicking phantoms [8, 9]. SFR spectroscopy allows us to determine tissue absorption without prior knowledge of the scattering coefficient [10]. Recently, SFR has been extended to multi-diameter single fiber reflectance spectroscopy



(MDSFR), in which two fiber diameters can be used to determine  $\mu'_s$  and  $\gamma$  [7, 11, 12]. An MDSFR measurement consists of several co-localized SFR measurements using different fiber diameters [11], which are each individually corrected for absorption [10], resulting in the reflectance in the absence of absorption,  $R_{SF}^0$ , for every SFR measurement. The co-localized, multi-fiber diameter values are then simultaneously fitted to the model described in Eq. 6.2,

$$R_{SF}^0(\lambda, d_{fib}) = \eta_{limit} \left( 1 + \rho_3 e^{(-\rho_1 \mu'_s d_{fib})} \right) \left[ \frac{(\mu'_s d_{fib})^{\rho_2}}{\rho_1 + (\mu'_s d_{fib})^{\rho_2}} \right], \quad (6.2)$$

where  $\eta_{limit}$  is the diffuse limit of the single fiber collection efficiency and  $[\rho_1, \rho_2, \rho_3]$  are  $\gamma(\lambda)$ -dependent coefficients, the values of which are derived from Monte Carlo simulations. The spectral shape of  $\mu'_s(\lambda)$  is constrained according to a biologically realistic power law decay. Solving the equation with two unknown variables for two different fiber diameters allows wavelength dependent quantification of both  $\mu'_s(\lambda)$  and  $\gamma(\lambda)$ . The MDSFR approach has been validated both *in silico* and in optical phantoms containing polystyrene microspheres over a wide range of biologically relevant values for  $\mu'_s(\lambda)$  and  $\gamma(\lambda)$ , with and without the presence of absorbers [7, 12]. In the current study we present, for the first time, differences in the wavelength dependence of  $\mu'_s$  and  $\gamma$  *in vivo*, measured using MDSFR. We have acquired MDSFR spectra *in vivo* from tumor, normal tongue tissue, skin and liver in an orthotopic xenograft model for oral cancer in mice using consecutive SFR measurements of two different fiber diameters (0.4 and 0.8 mm).

## Methods

### MDSFR reflectance model

First, the Beer-Lambert law is used to correct the measured SFR intensities  $R_{SF}(d_{fib})$  for absorption to obtain  $R_{SF}^0(d_{fib})$ :

$$R_{SF}(d_{fib}) = R_{SF}^0(d_{fib}) e^{-(\mu_a, tiss \langle L \rangle)}, \quad (6.3)$$

where  $R_{SF}^0(d_{fib})$  is given by Eq. 6.2,  $\mu_a, tiss$  is the absorption coefficient of tissue and  $\langle L \rangle$  is the effective photon path length, given by [8].

$$\frac{\langle L \rangle}{d_f} = \frac{C_{PF} 1.54}{(\mu'_s d_{fib})^{0.18} (0.64 + \mu_a d_{fib})^{0.64}}. \quad (6.4)$$

The absorption coefficient of tissue is expressed as the sum of the absorption of blood  $\mu_a^{blood}$  and the absorption of bilirubin  $\mu_a^{bil}$ :

$$\mu_{a,tiss}(\lambda) = \mu_a^{blood}(\lambda) + \mu_a^{bil}(\lambda). \quad (6.5)$$

The absorption coefficient of blood can be described as the product of the specific blood absorption coefficients and blood volume fraction:

$$\mu_a^{blood}(\lambda) = C_{cor}(\lambda) bvf [StO_2 \mu_a^{HbO_2}(\lambda) + (1 - StO_2) \mu_a^{Hb}(\lambda)], \quad (6.6)$$

where  $StO_2$  is the blood oxygen saturation,  $bvf$  is blood volume fraction assuming the concentration of hemoglobin in whole blood to be 150 g/L, and  $\mu_a^{HbO_2}$  and  $\mu_a^{Hb}$  are the specific absorption coefficients of oxygenized and deoxygenized blood, respectively.  $C_{cor}$  is the correction factor that accounts for flattening of spectral features resulting from the inhomogeneous distribution of blood in tissue and the confinement of blood in vessels [13, 14]. For whole blood, the correction factor is given by:

$$C_{cor} = \frac{1 - e^{\mu_a^{blood} D_v}}{\mu_a^{blood} D_v}, \quad (6.7)$$

and is related to the average vessel diameter  $D_v$ . The total tissue absorption  $\mu_{a,tiss}$  can then be described as the absorption of blood  $\mu_a^{blood}$ , dependend on blood volume fraction, and the absorption of bilirubin, which is the product of the specific absorption coefficient  $\mu_a^{bil,spec}$  and the bilirubin concentration  $c_{bil}$ :

$$\mu_{a,tiss}(\lambda) = \mu_a^{blood}(\lambda) + c_{bil} \mu_a^{bil}(\lambda). \quad (6.8)$$

The small but distinct GFP fluorescence emission peak present in the white light reflectance spectra of tumor was accounted for using a fit component  $Em_{GFP}(\lambda)$  to be included in the reflectance model:

$$R_{SF}(d_{fib}) = R_{SF}^0(d_{fib}) e^{-(\mu_{a,tiss}(L))} + c_{GFP} Em_{GFP}(\lambda). \quad (6.9)$$

This  $Em_{GFP}$  basis spectrum was previously acquired by fluorescence measurements of the tongue tumors, corrected for optical properties and system transmission. We attempted to include the absorption of GFP (determined from *in-vitro* cells) in the SFR analysis in the same way bilirubin is treated in Eq. 6.5. This did not result in a significant improvement of the fit, and GFP absorption was therefore omitted form the fit procedure.

The aim of this first step of the analysis is to remove the effects of absorption on the individual SFR spectra. It was shown previously that accurate absorption coefficients from individual SFR spectra can be obtained without prior knowledge of the tissue scattering properties [7, 10] if an optimized set  $[\rho_1, \rho_2, \rho_3, \text{CPF}]$  is used, *i.e.*  $\rho_1 = 6.82$ ,  $\rho_2 = 0.969$ ,  $\rho_3 = 1.55$ , and  $\text{CPF} = 0.944$ . The background scattering model used in this first step of individual analysis of each SFR spectrum is based on a 4th order polynomial, *i.e.*

$$\mu'_s = a_1 \left( \frac{\lambda}{\lambda_0} \right)^{-1} + a_2 \left( \frac{\lambda}{\lambda_0} \right)^{-2} + a_3 \left( \frac{\lambda}{\lambda_0} \right)^{-3} + a_4 \left( \frac{\lambda}{\lambda_0} \right)^{-4}. \quad (6.10)$$

This model allows sufficient degrees of freedom to correct for the physically incorrect assumption that  $[\rho_1, \rho_2, \rho_3, \text{CPF}]$  are independent of the wavelength. This aspect of the model will be further addressed in the discussion section. After removal of the effect of absorption on the individual SFR spectra, the MDSFR analysis is performed by solving Eq. 6.2 for multiple fiber diameters simultaneously. Here, the reduced scattering coefficient is modeled using the power law function:

$$\mu'_s = a_1 \left( \frac{\lambda}{\lambda_0} \right)^{-a_2}, \quad (6.11)$$

and Eq. 6.2 and Eq. 6.4 are adapted to yield a wavelength-dependent  $\gamma$ , by replacing the coefficients  $[\rho_1, \rho_2, \rho_3]$  with  $\rho_1 = 2.31\gamma^2$ ,  $\rho_2 = 0.57\gamma$ ,  $\rho_3 = 0.63\gamma^2$  in Eq. 6.2 [11] and  $C_{PF} = 0.68\gamma^{0.6}$  in Eq. 6.4. A Levenberg-Marquart nonlinear fit procedure is used to estimate the variables  $\mu'_s(\lambda)$  and  $\gamma(\lambda)$  from the MDSFR spectra of two different fiber diameters simultaneously. Finally, since the MDSFR analysis yields estimates of  $\mu'_s(\lambda)$  and  $\gamma(\lambda)$ , these values can now be used in the individual SFR fits to re-estimate the absorption coefficient. In the first step, the absorption coefficient was estimated without knowledge of the scattering properties by assuming fixed (wavelength independent) values for  $[\rho_1, \rho_2, \rho_3, \text{CPF}]$  and using a 4th order polynomial for  $\mu'_s(\lambda)$ ; the accuracy of that approach is now verified by using the

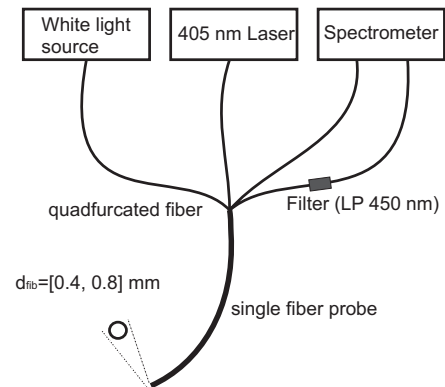


**Figure 6.1:** Schematic diagram of the measurement setup. Reflectance and fluorescence are measured through a single fiber of either 0.4 or 0.8 mm. Two identical setups are used to accommodate 2 fiber diameters

extracted wavelength dependent estimates of  $\gamma$  and using a biologically realistic shape for  $\mu'_s(\lambda)$ , i.e. a power law.

### Experimental setup

The illustration in Figure 6.1 represents a single probe-unit of the MDSFR spectroscopic setup.

During reflectance measurements, white light emitted by a halogen light source [HL-2000-FHSA; Ocean Optics; Duiven, NL] is directed through the first fiber of a quadfurcation into a solid core fiber-optic probe and guided onto the tissue. A small fraction of the light is reflected from the tissue into the acceptance cone of the probe fiber and directed via a second fiber of the quadfurcation into a spectrometer [SD-2000; Ocean Optics; Duiven, NL] for detection and further analysis. After the reflectance measurement, a low power fluorescence measurement is performed, using a 405 nm laser directed into another fiber of the quadfurcation to illuminate the tissue through the same probe. The emitted fluorescence is then guided through the last fiber of the quadfurcation, which leads through a 450 nm long-pass filter into a second spectrograph [QE-65000; Ocean Optics; Duiven, NL]. The fluorescence measurement is incorporated to ensure the presence of tumor cells, retro-virally infected with GFP, in the measurement volume. The complete MDSFR system consists of two identical probe-units containing fiber diameters of 0.4 and 0.8 mm. The fiber probes are sequentially placed in contact with the tissue under investigation. All probes are polished under an angle of 15 to minimize internal specular reflections from the probe tip. A calibration procedure was performed as described previously [7], consisting of a measurement in water in a dark container ( $I_{water}$ ) and a measurement in a liquid phantom containing 20% Intralipid diluted to yield  $\mu'_s(800\text{ nm}) = 1.2\text{ mm}^{-1}$ , ( $I_{IL}^{cal}$ ), where

$$R_{SF}^{meas} = I_{IL}^{sim} \left[ \frac{I_{meas} - I_{water}}{I_{IL}^{cal} - I_{water}} \right], \quad (6.12)$$

and  $I_{IL}^{sim}$  is the absolute SFR signal obtained through Monte Carlo simulations.

### Animal model

The study protocol was approved by the Animal Welfare Committee of the Leiden University Medical Center. Housing of BALB/cByJ nu/nu female mice (aged 4-6 weeks; Charles River Laboratories), the experiments and euthanazation were performed in accordance with the guidelines of this committee. Chlorophyll free food and sterilized water were provided without restriction. A set of 19 mice were injected with OSC19 cells lenti-virally transfected with luc and GFP (6x10<sup>4</sup> cells, Biocat, Heidelberg, Germany) [15,

16]. After an incubation period of 10-13 days, animals were included in the study and anesthetized with 2-3% Isoflurane. Reflectance spectra were acquired from tumor, normal tongue tissue (both 5 measurements), and skin and liver (both 3 measurements). The consecutive measurements were taken by removing and carefully repositioning the fiber between measurements, without imparting undue pressure on each tissue. For tumor, the fiber tip was positioned directly on top of the visible tumor. An additional MDSFR measurement of liver was carried out immediately before animals were sacrificed. After the animals were sacrificed, the tongue was harvested for microscopic tissue analysis.

### ***Data reduction and statistical analysis***

To verify the presence of tumor tissue in the measurement volume with the probe on top of the tumor, co-localized fluorescence spectra are acquired with both the 0.4 and 0.8 mm fiber. Since the quantum yield of CopGFP, incorporated to identify tumor tissue, is high, qualitative analysis of these spectra was sufficient to exclude measurements where tumor tissue was not present in the measurement volume. Two animals did not develop a visual tumor, and lacked GFP fluorescence in all five tumor measurements for both fiber diameters. These animals were excluded from the analysis of optical properties of tumor tissue. Variation in probe pressure and probe location in consecutive measurements may lead to slight variations in outcome, which can interfere with a proper analysis of the averaged MDSFR data. Therefore, all SFR spectra with  $R(800\text{ nm})$  deviating  $>2\sigma$  from the average value of  $R(800\text{ nm})$  of the consecutive measurements on each tissue site, were removed from the analysis after the first analysis step. To account for remaining variations in subsequent SFR measurements, the standard deviation of  $R(800\text{ nm})$  for each fiber diameter was used as a weight factor in the non-linear MDSFR fit procedure. Therefore, SFR fiber measurements with large variations contribute less to the best-fit outcome. Statistical analysis of optical properties for various tissues is done by using a paired Student T-test with  $P < 0.05$  as the level of significance.

## **Results**

After an incubation period of 10-13 days, 17 mice had a visible tumor at the tip of the tongue. Figure 6.2 shows a representative example of a combined confocal fluorescence and white light transmission microscopy image of a frozen section cut vertically through the center of the tongue. In this example the fiber tip was positioned in contact with the surface of the tongue in the upper left region of the image where tumor cells are close to the surface of the tongue. The image shows a thin but variable layer of epithelium

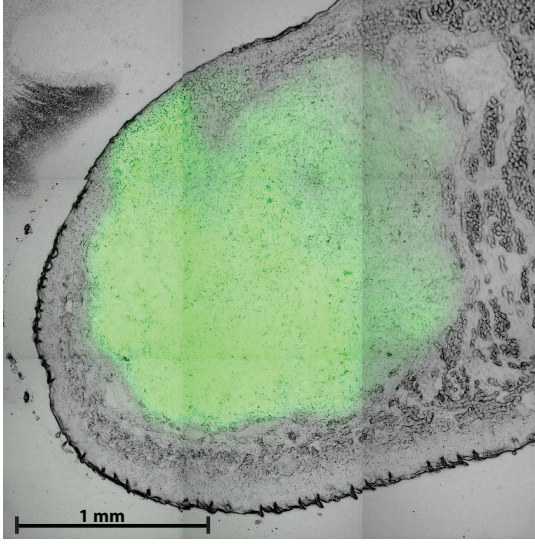


**Figure 6.2:** Confocal fluorescence microscopy image of mouse tongue, using 488 nm excitation and 520-540 nm detection, showing the distribution of GFP- expressing OSC tumor in green and transmitted 488 nm light in grey. Scale bar 1 mm.

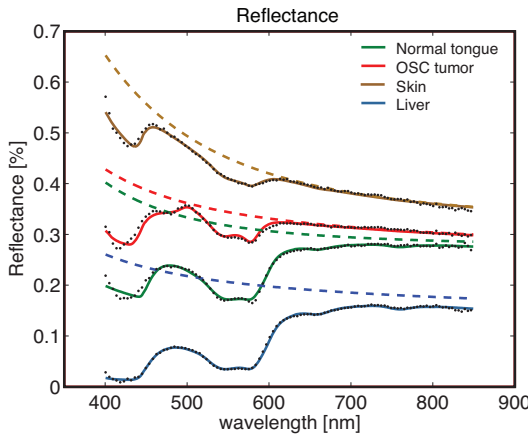


**Figure 6.3:** Typical 0.8 mm SFR data. Plotted are the measured  $R_{SF}$  (black dots), individual SFR fits (solid lines) and calculated (dashed lines) for normal tongue, tumor, skin and liver tissue.

overlying the GFP-fluorescent tumor at the tip of the tongue. A total of 588 reflectance spectra taken from 19 mice were analyzed in this study. Figure 6.3 shows representative reflectance spectra of tumor, tongue, skin and liver tissue, together with their best fits and calculated absorption-corrected reflectance  $R_{SF}^O$  for a 0.8 mm fiber (after the 3rd analysis step, based on power-law scattering and wavelength-dependent  $y$ ). In this example, the spectra taken on skin show a significantly higher reflectance over the whole wavelength range compared to normal tongue and tumor tissue, while reflectance for liver is lowest.  $R_{SF}^O$  spectra (dashed lines in Figure 6.3) of five consecutive co-localized measurements per fiber diameter are averaged, and these averaged spectra and their standard deviations serve as input for the MDSFR analysis. Figure 6.4 shows the average  $R_{SF}^O$  spectra of normal

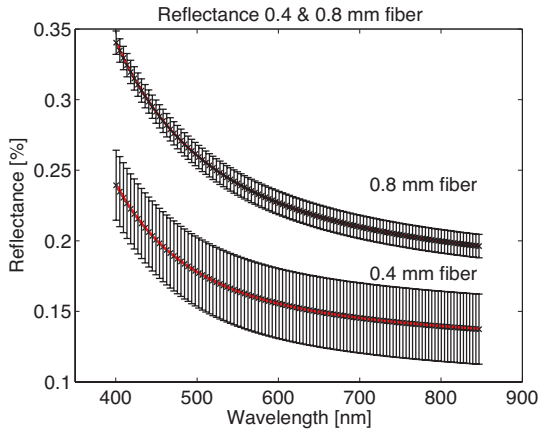


**Figure 6.4:** Averaged SFR spectra of normal tongue tissue; fiber diameters are 0.4 and 0.8 mm.

tongue tissue in a single mouse, fitted with the MDSFR model. As expected, a larger fiber diameter results in a higher reflectance.

Figure 6.5 a) and b) show  $\mu'_s(\lambda)$  and  $\gamma(\lambda)$  resulting from MDSFR fits on different tissues for a representative mouse. For all locations,  $\mu'_s$  decreases with increasing wavelength [17]. It is helpful to describe  $\mu'_s$  in terms of two parameters, the reduced scattering coefficient at 800 nm  $\mu'_s(800\text{nm})$ , and its wavelength dependent slope, which is often termed the scattering power (resp.  $a_1$  and  $a_2$  in Eq. 6.11). It has been shown that the scattering power is related to the refractive index correlation function of the measured tissue, and therefore has a direct relation with tissue structure [18, 19, 20]. In general we can conclude from all measurements that skin is most easily distinguishable from the other tissues by having a higher value for the scattering power. The difference between tumor and normal tongue tissue are more subtle, but tumor tends to have a lower scattering power than normal

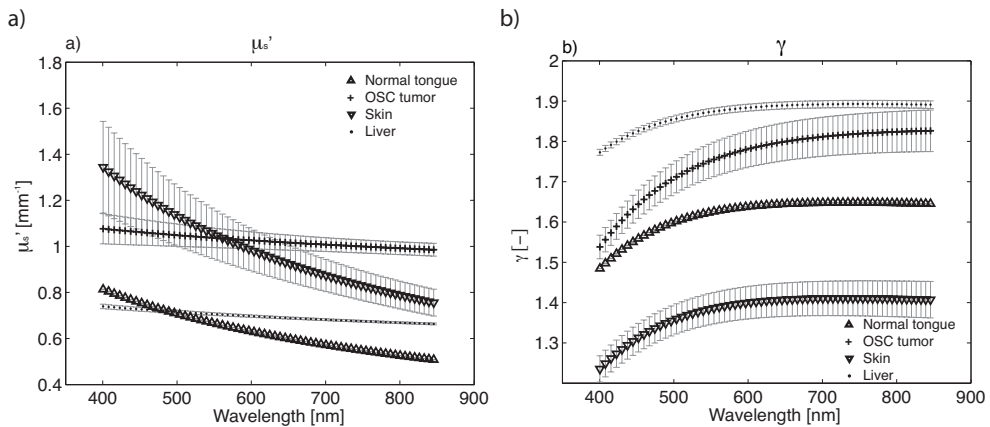


**Figure 6.5:**  $\mu'_s(\lambda)$  and  $\gamma(\lambda)$  for different tissues, measured in one representative mouse.

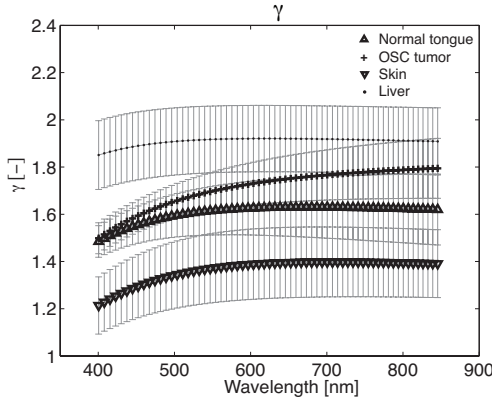


**Figure 6.6:**  $\gamma(\lambda)$  per tissue, averaged over  $n=19$ .

tongue tissue. Liver also shows a very low scattering power. The wavelength dependence of  $\gamma$  Figure 6.5 b) shows an increase with wavelength for the low wavelength region, for all tissue types. For higher wavelengths,  $\gamma$  either plateaus or decreases after reaching a maximum, except for tumor tissue, for which  $\gamma$  continues to increase with wavelength.

In Figure 6.6, we show the average  $\gamma(\lambda)$  for the four different tissue types, based on the measurements on all 19 mice. Figure 6.7 a), b), and c) show the median and quartiles of  $\mu'_s(800\text{nm})$ , the scattering power, and  $\gamma$  averaged over the 400- 850 nm wavelength range, for normal tongue, tumor tissue, skin and liver. Both Figure 6.6 and Figure 6.7 c) clearly show that  $\gamma$  is lowest for skin and highest for liver. Furthermore,  $\gamma$  for tumor increases monotonically with increasing wavelength, and increases more over the measured wavelength range than for normal tissue, although this difference is not significant. Table 1 summarizes the average values for scattering power,  $\mu'_s(800\text{nm})$  and average  $\gamma$  for the four tissue types.

Table 6.1: Scattering power,  $\mu'_s(800\text{nm})$  and average  $\gamma$  for four different tissues

	Scattering power	$\mu'_s(800\text{nm}) [\text{mm}^{-1}]$	$\gamma$
Normal tongue	$0.63 \pm 0.35$	$0.64 \pm 0.25$	$1.58 \pm 0.07$
OSC tumor	$0.13 \pm 0.16$	$0.90 \pm 0.29$	$1.72 \pm 0.09$
Skin	$0.86 \pm 0.49$	$0.81 \pm 0.37$	$1.37 \pm 0.14$
Liver	$0.24 \pm 0.20$	$0.71 \pm 0.08$	$1.87 \pm 0.07$

From Figure 6.7 a) and Table 6.1, it can be seen that the scattering powers of tumor and liver are significantly lower than for normal tongue and skin (Paired t-test,  $P < 0.05$ ). The  $\mu'_s(800\text{nm})$  for tumor is significantly higher than for normal tongue and liver. The average



value for  $\gamma$  of skin differs significantly from all other tissues. An interesting observation is that although the reflectance is highest for skin, the  $\mu'_s(\lambda)$  is not. This suggests that the angular distribution of scattering represented by  $\gamma(\lambda)$  can strongly influence the observed reflectance. The low  $\gamma(\lambda)$  for skin indicates that scattering is more directed backwards for skin than for other tissues, resulting in a higher total reflectance. For liver the opposite occurs; the low reflectance in this tissue is not a result of a low  $\mu'_s(\lambda)$ , but the high  $\gamma(\lambda)$  which indicates that most of the scattered light is directed forward.

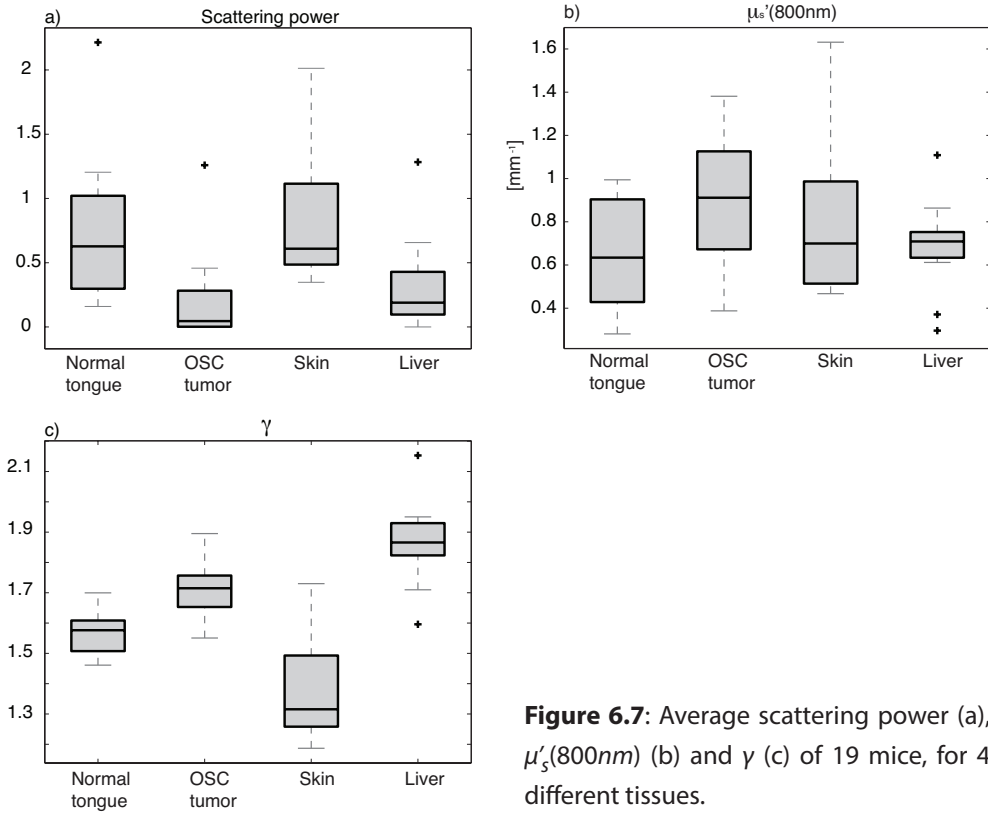


**Figure 6.7:** Average scattering power (a),  $\mu'_s(800nm)$  (b) and  $\gamma$  (c) of 19 mice, for 4 different tissues.

## Discussion and conclusion

In this paper we have presented the first *in vivo* measurements of  $\mu'_s(\lambda)$  and  $\gamma(\lambda)$  obtained using multi-diameter single fiber reflectance spectroscopy. We determined  $\mu'_s(\lambda)$  and  $\gamma(\lambda)$  for 4 different types of mouse tissue, including skin, liver, normal tongue and oral squamous cell carcinoma. Measurements of  $\mu'_s(\lambda)$  and  $\gamma(\lambda)$  show distinct differences between tissue types.

### *Comparison to previous studies: $\mu'_s(\lambda)$*

A number of previous studies have performed measurements to determine the optical (scattering) properties of tissues in *ex vivo* and *in vivo* tissue samples. The often significant limitations of measuring tissue optical properties in *ex vivo* samples is well recognized [21]. The measurement of tissue optical properties *in vivo* has for the most part been based on the use of diffuse reflectance spectroscopy or the measurement of interstitial fluence rate and angularly resolved radiance [21]. A range of tissue types have been investigated, in general for wavelengths above 630 nm. In the wavelength region between 630 and 850 nm the reduced scattering coefficient typically ranges from 0.4 – 1.31 mm<sup>-1</sup>, with tissues such as brain and stomach yielding higher values. These values are well within the range of those found in the present study. Thus far, the only data reported for shorter wavelengths is in the stomach [22] where the absolute value of  $\mu'_s$  is slightly higher than the range we obtained for our investigated tissues, but this is likely to be a consequence of the different tissue type. The scattering power is related to the shape of the refractive index correlation function and has recently been suggested to be an important factor in identifying tissue structure. *Ex vivo* data of various organs have been published [23, 24]. Yi and Backman have reported for rat liver a scattering power of 1.64±0.11, measured by inverse spectroscopic optical coherence tomography on excised organs. Hall *et al.* found the scattering power for fixed muscle tissue slices of mice to be 1.30±0.12 by measuring the angular distribution of light scattered through the sample, and fitting these observations to Monte Carlo simulations to obtain the optical properties of the sample under investigation. Although our *in vivo* scattering powers are low compared to these values, they are still within the range of  $0 < a_2 < 2$ , which is typical for tissue [25]. A recently published paper on *in vivo* measurements of the correlation length in colorectal field carcinogenesis reported scattering powers of  $0.2 < a_2 < 0.5$  [26]. This aligns well with the relatively low  $a_2$  values we have found in the present *in vivo* study. Whether the differences in scattering power are related to differences between *in vivo* and *ex vivo* scattering properties or due to differences in the optical methods remains a topic of investigation.

### Comparison to previous studies: $\gamma(\lambda)$

We observe marked differences when comparing our findings of the wavelength dependence of  $\gamma$  to the *in vivo* data published by Thueler *et al.* [22]. We have extracted  $\gamma$  values between 1.2 and 1.9 with  $\gamma$  generally increasing with wavelength;  $\gamma$  varied between 1.5 and 1.9 for tongue and tumor tissue, and between 1.2 and 1.5 for skin, which are within the range of expected values for tissue [27, 28]. Thueler *et al.* report measurements on stomach epithelium with an approximately constant  $\gamma$  with values around 2.0, and a slight increase in the low wavelength region. Whether these differences in  $\gamma$  are related to differences between tissue types or due to differences in the used optical methods remains to be investigated. It is interesting to consider that the spectral shape of  $\gamma$  can be linked to the correlation function of the refractive index in the tissue under investigation. The spectral shape of  $\gamma$  is determined by the first two Legendre moments of the phase function, which are wavelength dependent. The phase function and its derived metrics anisotropy ( $g_1$ ) and  $\gamma$  are, similar to the (reduced) scattering coefficient, related to the refractive index correlation function [20, 23]. The tissue refractive index correlation function has recently been modeled by the Whittle-Matern correlation function, which contains 3 variables: the deterministic factor  $m$ , the length scale of the correlation  $l_c$ , and the scaling factor  $N_c$ . While the scattering power is directly related to the deterministic factor  $m$ , the length scale of the correlation  $l_c$  is related to both  $\mu'_s$  and  $\gamma$ . In theory it is possible to express  $\gamma$  and its wavelength dependence in terms of  $l_c$ , and use the combined measurements of  $\mu'_s$  and  $\gamma$  to calculate the physical properties of the correlation function,  $m$  and  $l_c$ . However, this is beyond the scope of this paper and will be presented in future work.

### Step-analysis of fit procedure

MDSFR is based on the reflectance in the absence of absorption. In the vast majority of *in vivo* situations, where absorption is present, one first needs to determine the contribution of absorption to the total reflectance intensity using the model that we previously developed for individual SFR measurements. To achieve this, our analysis of tissue absorption and scattering in an individual SFR measurement was based on a background scattering model consisting of a polynomial ( $n=4$ ), together with an optimized set of wavelength-independent coefficients representing  $\gamma$  [10]. The choice of such a non-physical background scattering model is necessary in order to correct for the ill-posed assumption that  $\gamma$  is wavelength independent; the background scattering model needs sufficient freedom in this first step to correct for this assumption. It is important to emphasize that in the first step, we only need to remove the effect of absorption on the individual SFR spectra by implementing the approach reported previously [11]. The

MDSFR analysis itself is then performed with the physically realistic power-law scattering model (that follows from the definition of the Whittle-Matern correlation function), which yields values for the reduced scattering coefficient (defined by the scattering power and  $\mu'_s(800\text{nm})$ ) and  $\gamma$ . To verify that the absorption was correctly estimated in the first step, the extracted values for  $\gamma$  from the MDSFR analysis were used to re-analyse the individual SFR measurements using the power-law scattering model and the extracted wavelength-dependent  $\gamma$ . We found that the absorption spectra extracted in the first step were almost identical to the absorption spectra extracted using the power-law scattering model and the wavelength dependent  $\gamma$ , as indicated by an average Pearson correlation coefficient of  $R^2 = 0.99$  between extracted absorption spectra. Clearly when more information becomes available about the wavelength dependence of  $\gamma$ , that knowledge could be used to spectrally constrain  $\gamma$  and thus complete an MDSFR fit in a single step fitting routine.

### **Limitations**

#### *A - Probe replacement*

A potential limitation of the present study is caused by the fact that multiple fibers with different diameters are used sequentially. Therefore, slight differences in measurement volume are not only due to different fiber diameters but can also occur from measuring a slightly different spot in each measurement. Sequentially measuring the exact same tissue location with the exact same pressure for various fiber diameters is not only time consuming, but also makes the current measurement procedure cumbersome and sensitive to measurement artifacts. Clearly the use of a single measurement probe that is capable of rapidly changing its effective aperture would be a major step forward. New technological developments should overcome this problem in the near future and provide true co-localized measurement positions for various fiber diameters [29]. Despite the uncertainty in probe repositioning, the standard deviations for an individual mouse on the MDSFR fitted values for  $\mu'_s$  and  $\gamma$  (Figure 6.5 a) and b)) are all within 10% of the fitted value (with the exception of  $\mu'_s$  for skin), which is very encouraging.

#### *B- Layered tissue*

It is well known that skin and oral mucosa are comprised of layered tissue. In skin the stratum corneum and epidermis overlay the underlying dermis. In the oral cavity the normal tongue is comprised of a superficial keratinized layer with underlying epithelial layer and deeper lying connective tissue comprised of orthogonal muscle fiber bundles. The two, 0.4 and 0.8 mm, fibers are expected to probe the relatively homogeneous layers of tissue comprising mouse epithelium and dermis in the skin and the tongue epithelium and underlying connective tissue in normal tongue. OSC in the tongue develops beneath

the superficial keratinized layer but can potentially be overlain by a layer of epithelial tissue of variable thickness. Microscope images of sections of OSC in the tongue (Figure 6.2) show variation in thickness of the tissue layer covering the tumor between animals. Although tumor size and position varied somewhat between animals, placing the fiber probe on a position where the tumor was visible minimized the distance between tumor and fiber tip. Since the measurement volume and depth increase with increasing fiber diameter, the smallest fiber diameter was specifically chosen to be 0.4 mm to incorporate tumor within the measurement volume. However, the contribution of the top layer of the tongue epithelium to the total acquired signal will be slightly different for each fiber diameter. Given these concerns we analyzed spectra acquired using each fiber diameter at a single location. This analysis showed consistent values for scattering power between fiber diameters. While this result suggests that the influence of epithelium overlying the tumor is small, it could be a reason why we observe only a relatively small difference in scattering signature between normal tongue and tumor tissue. The potential confounding effect of overlying epithelium could be removed in the future by studying a chemically induced model of oral cancer in animals or interrogating superficial human OSC.

### ***Future developments***

Quantification of tissue optical properties does not only yield direct diagnostic information, it also facilitates the use of quantitative *in vivo* fluorescence measurements. To quantify the concentration of an (exogenous) fluorophore in tissue, for example to monitor photodynamic therapy, knowledge of local tissue optical properties is necessary to correct for the effects of scattering and absorption on the collected fluorescence [30]. Our setup allows for reflectance and fluorescence measurements to be taken with the same probe, providing a method to determine fluorescence corrected for the influence of tissue optical properties, which opens the way to quantitatively compare fluorescence from different tissues and patients.

In conclusion, we have presented the first *in vivo* MDSFR analysis of four different tissue types, based on measurements of 19 animals. Analysis of scattering power, reduced scattering at 800 nm and average  $\gamma$  resulted in significant differences for the four tissue types studied. Future work will address the relation between  $\mu'_s(\lambda)$  and  $\gamma(\lambda)$  and the properties of the tissue refractive index correlation function  $m$  and  $l_c$ .

## References

- [1] R Reif, O A'Amar, and I J Bigio. Analytical model of light reflectance for extraction of the optical properties in small volumes of turbid media. *Applied Optics*, 46(29):7317–7328, 2007.
- [2] A Amelink, H J C M Sterenborg, M P L Bard, and S A Burgers. *In vivo* measurement of the local optical properties of tissue by use of differential path-length spectroscopy. *Optics Letters*, 29(10):1087–1089, 2004.
- [3] G Zonios, L T Perelman, V Backman, R Manoharan, M Fitzmaurice, J Van Dam, and M S Feld. Diffuse reflectance spectroscopy of human adenomatous colon polyps *in vivo*. *Applied Optics*, 38(31):6628–37, November 1999.
- [4] H Tian, Y Liu, and L Wang. Influence of the third-order parameter on diffuse reflectance at small source–detector separations. *Optics Letters*, 31(7):933–935, 2006.
- [5] F Bevilacqua and C Depeursinge. Monte Carlo study of diffuse reflectance at source–detector separations close to one transport mean free path. *Journal of the Optical Society of America A*, 16(12):2935–2945, 1999.
- [6] S C Kanick, U A Gamm, M Schouten, H J C M Sterenborg, D J Robinson, and A Amelink. Measurement of the reduced scattering coefficient of turbid media using single fiber reflectance spectroscopy : fiber diameter and phase function dependence. *Biomedical Optics Express*, 2(1):119–131, 2011.
- [7] U A Gamm, S C Kanick, H J C M Sterenborg, D J Robinson, and A Amelink. Quantification of the reduced scattering coefficient and phase-function-dependent parameter  $\gamma$  of turbid media using multidiameter single fiber reflectance spectroscopy: experimental validation. *Optics Letters*, 37(11):1838–40, June 2012.
- [8] S C Kanick, D J Robinson, H Sterenborg, and A Amelink. Monte Carlo analysis of single fiber reflectance spectroscopy. *Physics in Medicine and Biology*, 54:6991–7008, 2009.
- [9] S C Kanick, H Sterenborg, and A Amelink. Empirical model of the photon path length for a single fiber reflectance spectroscopy device. *Optics Express*, 17:860–871, 2009.
- [10] S C Kanick, D J Robinson, H J C M Sterenborg, and A Amelink. Method to quantitate absorption coefficients from singlefiber reflectance spectra without knowledge of the scattering properties. *Optics Letters*, 36(15):2791–3, August 2011.
- [11] S C Kanick, U A Gamm, H J C M Sterenborg, D J Robinson, and A Amelink. Method to quantitatively estimate wavelength-dependent scattering properties from multidiameter single fiber reflectance spectra measured in a turbid medium. *Optics Letters*, 36(15):2997–9, August 2011.
- [12] U A Gamm, S C Kanick, H J C M Sterenborg, D J Robinson, and A Amelink. Measurement of tissue scattering properties using multi- diameter single fiber reflectance spectroscopy: in silico sensitivity analysis. *Biomedical Optics Express*, 2(11):3150–66, November 2011.
- [13] R L P Van Veen, W Verkruysse, and H Sterenborg. Diffuse-reflectance spectroscopy from 500 to 1060 nm by correction for inhomogeneously distributed absorbers. *Optics Letters*, 27(4):246–248, 2002.
- [14] N Rajaram, A Gopal, X Zhang, and J W Tunnel. Experimental Validation of the Effects of Microvasculature Pigment Packaging on *In Vivo* Diffuse Reflectance Spectroscopy. *Lasers in Surgery and Medicine*, 42:680–688, 2010.

- [15] T Yokoi, A Yamaguchi, T Odajima, and K Furukawa. Establishment and Characterization of a Human Cell Line Derived from a Squamous Cell Carcinoma of the Tongue.pdf. Tumor Research, (23):43–57, 1988.
- [16] F Carlotti, M Bazuine, T Kekarainen, J Seppen, Pognonec, J A Maassen, and R C Hoeben. Lentiviral vectors efficiently transduce quiescent mature 3T3-L1 adipocytes. Molecular therapy : the journal of the American Society of Gene Therapy, 9(2):209– 17, February 2004.
- [17] A E Cerussi, A J Berger, F Bevilacqua, N Shah, D Jakubowski, J Butler, R F Holcombe, and B J Tromberg. Sources of absorption and scattering contrast for near-infrared optical mammography. Academic Radiology, 8(3):211–8, March 2001.
- [18] V Turzhitsky, N N Mutyal, A R Radosevich, and V Backman. Multiple scattering model for the penetration depth of low-coherence enhanced backscattering. Journal of Biomedical Optics, 16(9):097006, September 2011.
- [19] V Turzhitsky, A Radosevich, J D Rogers, A Taflove, and V Backman. A predictive model of backscattering at subdiffusion length scales. Biomedical Optics Express, 1(3):1034–1037, 2010.
- [20] J D Rogers, I R Capoglu, and V Backman. Nonscalar elastic light scattering from continuous media in the Born approximation: erratum. Optics Letters, 35(9):1367, April 2010.
- [21] A J Welch and M van Gemert. Optical-Thermal Response of Laser Irradiated Tissue. Plenum press, New York, 1995.
- [22] P Thueler, I Charvet, F Bevilacqua, M S Ghislain, G Ory, P Marquet, P Meda, B Vermeulen, and C Depeursinge. *In vivo* endoscopic tissue diagnostics based on spectroscopic absorption, scattering, and phase function properties. Journal of Biomedical Optics, 8:495, 2003.
- [23] Ji Yi and Vadim Backman. Imaging a full set of optical scattering properties of biological tissue by inverse spectroscopic optical coherence tomography. Optics Letters, 37(21):4443–5, November 2012.
- [24] G Hall, S L Jacques, K W Eliceiri, ad P J Campagnola. Goniometric measurements of thick tissue using Monte Carlo simulations to obtain the single scattering anisotropy coefficient. Biomedical Optics Express, 3(11):2707–19, November 2012.
- [25] M Xu and R R Alfano. Fractal mechanisms of light scattering in biological tissue and cells. Optics Letters, 30(22):3051–3053, 2005.
- [26] A J Gomes, S Ruderman, M Delacruz, R K Wali, H K Roy and V Backman . *In vivo* measurement of the shape of the tissue-refractive-index correlation function and its application to detection of colorectal field carcinogenesis. Journal of Biomedical Optics, 17(4):047005, April 2012.
- [27] F Bevilacqua, D Piguet, P Marquet, J D Gross, B J Tromberg, and C Depeursinge. *In vivo* local determination of tissue optical properties: applications to human brain. Applied Optics, 38(22):4939–4950, 1999.
- [28] S Chamot, E Migacheva, O Sydoux, P Marquet, and C Deperusinge. Physical interpretation of the phase function related parameter  $\gamma$  studied with a fractal distribution of spherical scatterers. 18(23):23664–23675, 2010.
- [29] C L Hoy, U A Gamm, H J C M Sterenborg, D J Robinson, and A Amelink. Use of a coherent fiber bundle for multi-diameter single fiber reflectance spectroscopy. Biomedical Optics Express, 3(10):2452–64, October 2012.
- [30] B C Wilson, M S Patterson, and L Lilge. Implicit and explicit dosimetry in photodynamic therapy: a new paradigm. Lasers in Medical science, 1997.





# Chapter 7

Measurement of refractive index correlation function properties using fiber-optic reflectance spectroscopy: *in silico* proof of concept<sup>6</sup>

---

6

U.A. Gamm, C.L. Hoy, H.J.C.M. Sterenborg, D.J. Robinson, A. Amelink, Measurement of refractive index correlation function properties using fiber-optic reflectance spectroscopy: *in silico* proof of concept, in preparation (2013)



# Chapter 8

## Discussion

This thesis describes the development of multi-diameter single fiber reflectance spectroscopy, a method which is based on single fiber reflectance measurements and allows the quantification of the tissue scattering properties  $\mu'_s$  and  $\gamma$ . This chapter will discuss the findings presented in the previous chapters and provide an outlook on future work towards the diagnosis of early cancers.

## Development of the MDSFR method

Chapters 2-4 describe *in silico* analysis of single fiber reflectance, which led to the development of an empirical relation for the dependence of the single fiber reflectance signal ( $R_{SF}$ ) on the dimensionless reduced scattering coefficient ( $\mu'_s d_{fb}$ ) and the phase function dependent parameter  $\gamma$ . Based on Monte Carlo simulations, it was shown that collecting spectra from multiple fiber diameters enables the determination of  $\mu'_s$  and  $\gamma$  by fitting the combined reflectance spectra to the  $R_{SF}$  model. The MDSFR method proved to be robust in determining  $\mu'_s$  and  $\gamma$  (errors below 10%) for as little as 2 fiber diameters when  $\mu'_s > 1\text{mm}^{-1}$ . For  $\mu'_s < 1\text{mm}^{-1}$  only the fiber combination of 0.2 and 1 mm showed acceptable results with errors of 20% and 10% for estimation of  $\mu'_s$  and  $\gamma$ , respectively. The feasibility to perform MDSFR with only two fiber diameters offers the possibility to perform clinical measurements through biopsy needles to assess the optical properties of cancer *in vivo* [1].

## Experimental validation of MDSFR

To translate the MDSFR method into an experimental setting, a new calibration method was developed using an Intralipid-based phantom that both corrects the acquired signal for spectral properties of the light source and transmission through the system, and scales the spectrum onto an absolute scale (Chapter 5). MDSFR measurements were then performed on a phantom containing polystyrene beads as a scatterer that was designed such that its phase function would approximate a modified Henyey-Greenstein phase function, which our SFR model is based upon. The new calibration procedure proved to be accurate allowing the experimentally collected data to match up with simulations of the phantom. One drawback of the Intralipid calibration is that the theoretical single fiber reflectance intensities, which are used to scale the data to absolute reflectance values, were acquired by Monte Carlo simulations that use an empirical phase function of Intralipid. This means that the accuracy of our calibration is dependent on the accuracy of the Intralipid phase function used in the simulation [2]. Thus, any errors introduced by

assuming the wrong phase function can lead to errors in the estimation of the scattering properties. Despite this potential risk, the MDSFR analysis estimated  $\mu'_s$  and  $\gamma$  with residual errors around 5%.

### ***In vivo* MDSFR measurements**

The first *in vivo* MDSFR measurements were successfully performed on four different tissue types including skin, liver, tongue and an orthotopic squamous cell carcinoma in a mouse model. Measurements were performed by sequentially measuring the SFR signal with two different fiber diameters (0.4 and 0.8 mm). Values found for  $\mu'_s$  (800 nm) and its scattering power were within the range of published values. Average  $\gamma$  values also correlated with values published by other groups. The spectral shape of  $\gamma$  measured by MDSFR showed a wavelength dependent increase. In literature, spectrally flat  $\gamma$  values were reported for human brain, skull, nerve and tumor tissue [3] and a slight wavelength dependent decrease was reported for  $\gamma$  values measured in the human gastrointestinal tract [4]. These deviations in the spectral shape of  $\gamma$  are likely to be caused by the different tissue types that were measured.

Our MDSFR measurements were performed by taking sequential measurements with two different fibers with different fiber diameters. Here both probes had to be placed onto exactly the same position which introduced an uncertainty to the measurements. However, standard deviations in the estimated values of  $\mu'_s$  and  $\gamma$  did not exceed 10%, showing the feasibility of MDSFR *in vivo*. However, for clinical measurements performing subsequent measurements with different fiber diameters is too time consuming. To address this issue, our group has developed a second generation MDSFR device that uses a fiber bundle, where the illumination of individual fibers can be controlled, leading to three effective fiber diameters ( $d_{fb} = 0.2, 0.6, 1$  mm) [5]. During *in vivo* measurements with the MDSFR method, each different fiber diameter is probing a different volume, ranging from a few hundred cubic micrometers to cubic millimeters, dependent on the choice of fiber diameters and tissue optical properties. Tissue inhomogeneities and layers with different optical properties will therefore affect the SFR signal differently for each fiber diameter. Inhomogeneities in absorption, e.g. blood vessels located at different depths, are not expected to cause a problem because each SFR signal from each fiber diameter is corrected for absorption individually before the MDSFR analysis is performed. Inhomogeneities in scattering, however, will not be corrected and could therefore lead to a wrong estimation of  $\mu'_s$  and  $\gamma$ . It is hard to predict the impact of scattering inhomogeneities on the MDSFR results. It is possible that resulting  $\mu'_s$  and  $\gamma$  values are simply averaged values over the sampled volumes, or that the MDSFR fit would be unable to fit the model to the spectra.

A detailed analysis of the effect of tissue layers and inhomogeneities on the SFR signal would be necessary to detect and correct for errors introduced. This analysis could either be performed with Monte Carlo simulations or on tissue simulating phantoms.

## Tissue as random continuous medium

The last chapter attempts to relate optical parameters to microstructural properties of the tissue by modeling the tissue as a random continuous medium. The refractive index (RI) fluctuations are described by the Whittle-Matérn correlation function, which is dependent on the variance of the RI, a parameter that defines the shape of the correlation function  $m$ , and the correlation length  $l_c$ . Monte Carlo simulations were run with a PF derived from the WM correlation function and the MDSFR method, which incorporated a relationship between  $\gamma$  and  $l_c$ , was applied to the dataset. It was shown that  $\mu'_s$  and  $\gamma$  could be estimated with great accuracy. The shape parameter  $m$ , which is linked to  $\mu'_s = A\lambda^{2m-4}$ , was estimated correctly as well. Estimation of  $l_c$  proved to be complicated by the shape of the relationship between  $\gamma$  and  $l_c$  which led to large errors for  $l_c$  values above  $1\ \mu\text{m}$ . A modified WM PF was discussed which includes an isotropic term. Even a small isotropic contribution showed a dramatic effect on the spectral shape of  $\gamma$ . Specifically, the addition of the isotropic term produced decreasing  $\gamma$  values for a range of  $l_c$ , which matches the spectral shape observed *in vivo*.

A modified WM PF, however, would lose its connection to the WM correlation function which is linking morphological properties to the optical properties. Therefore, it would be better to modify the WM correlation function itself to yield a broader range of PF that allows changes to the spectral shape of  $\gamma$ .

## Limitations of the method

The MDSFR method is based on a semi-empirical model that was derived from investigating Monte Carlo simulations. One limitation of the model is its inability to describe the reflectance for small fiber diameters  $<100\ \mu\text{m}$  where higher order moments are likely to have a larger effect on the  $R_{SF}$  signal. In order to perform MDSFR measurements with smaller fiber diameters, the model has to be adapted. These adaption can be made based on Monte Carlo simulations or based on analytical modeling and is a topic of future research.

Another challenge is the design of optical phantoms to validate the method because the optical properties of the phantom must be fully controllable, with a known phase

function and the optical properties should approximate real tissue optical properties. In the experimental validation of MDSFR, we have already shown for the case of polystyrene spheres that differences in the PF moments caused a slight misestimation in  $\gamma$ . Therefore, it would be crucial that the PF of the phantom approximates a tissue PF. Unfortunately, commonly used scattering substances like Intralipid, titanium dioxide or polystyrene spheres have PFs that are different from tissue. As an alternative approach, living cells might serve as scatters. Cell cultures offer a more controllable environment than live tissues; *e.g.* cells can be grown in relatively homogeneous spheroids of a few hundred  $\mu\text{m}$  diameter, which would allow MDSFR measurements in direct contact [6, 7, 8]. The PF could be measured experimentally in a goniometer setup and the correlation length could be determined from electron microscopy images.

## Outlook

Future work will focus on two closely related aspects: the technological development of the method and the translation of the technology into the clinic. In an ongoing clinical study, our group is investigating the optical properties of healthy and malignant breast tissue on patients undergoing biopsy of a suspicious lesion found during mammographic breast imaging. Measurements are performed during the biopsy procedure with a custom made fiber-optic probe that fits through the biopsy needle allowing measurements in direct contact with the cancerous tissue. The probe incorporates two adjacent fibers of 0.4 and 0.8 mm. Preliminary results showed differences in the scattering slope of  $\mu'_s$  and clear differences in the magnitude of  $\gamma$  between healthy and malignant breast tissue [1].

A second-generation MDSFR device has been developed that uses a fiber bundle with 19 fibers of 200  $\mu\text{m}$  diameter, which can be illuminated individually, leading to three different effective fiber diameters ( $d_{fb}=[0.2, 0.6, 1]$  mm). The device is currently used in the Rotterdam (ERGO) study, which is a large cohort study that investigates the prevalence and incidence of risk factors for diseases in elderly men and women over many years. MDSFR measurements of the skin are taken on face and forearm to investigate whether the scattering signature changes over time in those patients that develop skin cancer. Even though measurements are performed on normal appearing skin and not on lesions, it is hypothesized that normal skin would undergo subtle morphological changes as well, caused by the field effect of carcinogenesis. This means that risk factors, *e.g.* the sunlight, would not lead only to focal lesions but also affect the whole surface of the skin.

An identical device will be used in a clinical study to investigate the scattering signatures of benign and malignant lesions of the skin on 150 patients. Additionally, the group is working on a third-generation MDSFR device that uses a fiber bundle with fiber

cores of only  $7\ \mu\text{m}$  diameter. Here illumination of the fiber bundle is controlled by a DMD mirror, allowing incremental variation in effective fiber diameters between  $7\ \mu\text{m}$  and  $1.45\ \text{mm}$  [9]. Measurements with very small fiber diameters probe less deep into the tissue and are more sensitive to higher order moments of the PF, which could potentially lead to more accurate characterization of tissue morphology. Additionally a coherent fiber bundle can be used for imaging as well, which could lead to the development of a combined setup of spectroscopic measurements and microendoscopic imaging [10, 11].

Finally, quantitative measurement of  $\mu'_s$  form the basis for quantitative single fiber fluorescence spectroscopy. Our group has recently investigated the relationship between the fluorescence intensity collected by a single fiber and the scattering properties and presented a semi-empirical model which allows estimation of the intrinsic fluorescence provided that  $\mu'_s$  is known [12, 13, 5]. Quantitative fluorescence measurements may contribute to diagnostic and clinical applications, *e.g.* the quantification of endogeneous fluorophores NADH and FAD allows to monitor the metabolic state of tissue and the quantification of fluorescent drugs like photosensitizers can support treatment planning for photodynamic therapy.

In conclusion this thesis summarizes the development of MDSFR, which is a cost-efficient and simple method that has the potential to support clinical diagnostics of early cancer.



## References

- [1] U A Gamm, M Heijblom, D Piras, F M Van den Engh, S Manohar, W Steenbergen, H J C M Sterenborg, D J Robinson, and A Amelink. *In vivo* determination of scattering properties of healthy and malignant breast tissue by use of multi-diameter-single fiber reflectance spectroscopy (MDSFR). 8592:85920T–85920T–6, February 2013.
- [2] R Michels, F Foschum, and A Kienle. Optical properties of fat emulsions. *Optics Express*, 16:5907–5925, 2008.
- [3] F Bevilacqua, D Piguet, P Marquet, J D Gross, B J Tromberg, and C Depeursinge. *In vivo* local determination of tissue optical properties: applications to human brain. *Applied Optics*, 38(22):4939–4950, 1999.
- [4] P Thueler, I Charvet, F Bevilacqua, M S Ghislain, G Ory, P Marquet, P Meda, B Vermeulen, and C Depeursinge. *In vivo* endoscopic tissue diagnostics based on spectroscopic absorption, scattering, and phase function properties. *Journal of Biomedical Optics*, 8:495, 2003.
- [5] C L Hoy, U A Gamm, H J C M Sterenborg, D J Robinson, and A Amelink. Method for rapid multi-diameter single fiber reflectance and fluorescence spectroscopy through a fiber bundle. *Journal of Biomedical Optics*, submitted, 2013.
- [6] F Hirschhaeuser, H Menne, C Dittfeld, J West, W Mueller-Klieser, and L A Kunz-Schughart. Multicellular tumor spheroids: an underestimated tool is catching up again. *Journal of Biotechnology*, 148(1):3–15, July 2010.
- [7] R-Z Lin and H-Y Chang. Recent advances in three-dimensional multicellular spheroid culture for biomedical research. *Biotechnology journal*, 3(9-10):1172–84, October 2008.
- [8] P G Layer, A Robitzki, A Rothermel, and E Willbold. Of layers and spheres: the reaggregate approach in tissue engineering. *Trends in neurosciences*, 25(3):131–4, March 2002.
- [9] C L Hoy, U A Gamm, H J C M Sterenborg, D J Robinson, and A Amelink. Use of a coherent fiber bundle for multi-diameter single fiber reflectance spectroscopy. *Biomedical Optics Express*, 3(10):2452–64, October 2012.
- [10] P Sharma, A R Meining, E Coron, C J Lightdale, H C Wolfsen, A Bansal, M Bajbouj, J-P Galmiche, J A Abrams, A Rastogi, N Gupta, J E Michalek, G Y Lauwers, and M B Wallace. Real-time increased detection of neoplastic tissue in Barretts esophagus with probe-based confocal laser endomicroscopy: final results of an international multicenter, prospective, randomized, controlled trial. *Gastrointestinal Endoscopy*, 74(3):465–472, 2011.
- [11] A M Buchner, M W Shahid, M G Heckman, M Krishna, M Ghabril, M Hasan, J E Crook, V Gomez, M Raimondo, T Woodward, H C Wolfsen, and M B Wallace. Comparison of probe-based confocal laser endomicroscopy with virtual chromoendoscopy for classification of colon polyps. *Gastroenterology*, 138(3):834–42, March 2010.
- [12] S C Kanick, D J Robinson, H J C M Sterenborg, and A Amelink. Semiempirical model of the effect of scattering on single fiber fluorescence intensity measured on a turbid medium. *Biomedical Optics Express*, 3(1):137–52, January 2012.
- [13] S C Kanick, D J Robinson, H J C M Sterenborg, and A Amelink. Extraction of intrinsic fluorescence from single fiber fluorescence measurements on a turbid medium. *Optics letters*, 37(5):948–50, March 2012.



# Chapter 9

Summary  
Samenvatting

## Summary

This thesis presents the development of a fiber-optic method, multi-diameter single fiber reflectance (MDSFR) spectroscopy, which allows the quantitative determination of two tissue scattering properties, *i.e.* the reduced scattering coefficient  $\mu'_s$  and a parameter related to the angular distribution of scattering,  $\gamma$ .

In **chapter 2** Monte Carlo simulations are used to investigate the relation between the single fiber reflectance (SFR) intensity and the fiber diameter  $d_{fib}$ , the reduced scattering coefficient  $\mu'_s$  and the phase function (PF). Based on these simulations a relationship between the SFR signal  $R_{SF}$  and the dimensionless reduced scattering coefficient  $\mu'_s d_{fib}$  was identified. The model is accurate both in the low scattering region, where the signal is PF dependent, as well as in the PF-independent high scattering region ( $\mu'_s d_{fib} > 10$ ). Based on this PF-independent behavior for high scattering, we designed a solid optical calibration phantom with a very high reduced scattering coefficient ( $\mu'_s > 200 \text{ mm}^{-1}$ ) that can be used to scale SFR measurements to an absolute scale. Experimental measurements on optical phantoms containing Intralipid as scatterer, were performed using the new calibration method. We found that  $\mu'_s$  could be accurately quantified by fitting the experimental data to the SFR model, if prior knowledge about the PF-dependent model parameters are used from Monte Carlo simulations of SFR in Intralipid.

In **chapter 3**, the relation between the SFR model parameters and the PF-dependent parameter  $\gamma$  is presented. Furthermore, the concept of multi-diameter single fiber reflectance (MDSFR) spectroscopy is introduced. We show that multiple SFR measurements with different fiber diameters allows an accurate determination of  $\mu'_s$  and  $\gamma$  by applying a multi-dimensional curve fit of the SFR model and specifying the wavelength dependence of the reduced scattering coefficient as  $\mu'_s = a\lambda^{-b}$ .

**Chapter 4** investigates the sensitivity and limitations of the MDSFR approach on an extensive set of Monte Carlo simulations following the Modified Henyey-Greenstein PF. It was shown that the MDSFR approach shows good results even when applied to single wavelength, *i.e.* when no prior knowledge about the spectral dependence of  $\mu'_s$  is incorporated into the fitting routine. This method, however, is only applicable in wavelength regions where tissue absorption is weak enough to not affect the reflectance intensity. The effect of using different amounts and ranges of fiber diameters contributing to the MDSFR fit was investigated on simulated SFR data for seven different fiber diameters between 0.2 mm and 1.5 mm, for both the single wavelength and the spectrally resolved MDSFR analysis. For both cases, the MDSFR method was shown to be relatively insensitive to limiting the number of fiber diameters by removing intermediate fiber diameters but incorporating fiber diameters of 0.2 mm and 1.5 mm. When large fiber diameters were removed, the residual error in estimating  $\mu'_s$  and  $\gamma$  increased. Furthermore, low reduced

scattering values are generally estimated with a higher residual error (scattering set  $\mu'_s = 0.4\text{--}1\text{ mm}^{-1}$ ). Finally, the accuracy of the spectrally-resolved MDSFR analysis was tested by varying the dataset such that  $\gamma$  values were either spectrally constant, spectrally decreasing or random over the wavelength range. For all three cases  $\mu'_s$  and  $\gamma$  could be estimated accurately, showing that the MDSFR method is independent of the spectral dependence of  $\gamma$ .

**Chapter 5** describes the experimental validation of the MDSFR method on an optical phantom containing polystyrene spheres in a fractal distribution. The fractal dimension was chosen such that the resulting PF, which can be calculated from Mie theory, would approximate a Modified Henyey-Greenstein PF. A new calibration method is introduced that replaces the calibration on spectralon and the solid high scattering calibration phantom. This new calibration method combines the spectral and absolute calibration by taking SFR measurements on an optical phantom containing Intralipid. The fiber diameter-specific absolute reflectance of that phantom was determined using Monte Carlo simulations of Intralipid. The MDSFR method was applied to the fractal scattering phantom containing polystyrene spheres, and  $\mu'_s$  and  $\gamma$  were determined in absence and in presence of an absorber (Evans Blue).

**Chapter 6** presents the first *in vivo* MDSFR measurements on four different tissue types in mice: skin, liver, normal tongue and an orthotopic oral squamous cell carcinoma. Spectra were taken subsequently with two different fiber diameters ( $d_{fb} = [0.4, 0.8]\text{ mm}$ ). The extracted values for  $\mu'_s$  for the different tissue types were all within the range of  $\mu'_s$  values published in literature. Significant differences in scatter power and  $\mu'_s$  (800 nm) between the different tissue types were found. The extracted  $\gamma$  values for all tissue types showed a monotonic increase with wavelength, were within the range of expected values and showed significant differences between the different tissue types.

Finally, **chapter 7** relates the optically measured parameters  $\mu'_s$  and  $\gamma$  to tissue properties by considering tissue as a medium with random and continuous refractive index fluctuations. A PF that is derived from the Whittle-Matérn refractive index correlation function is used to simulate SFR data that are then analyzed by MDSFR. The MDSFR fit showed excellent results in extracting  $\mu'_s$  and  $\gamma$  for this particular PF. An empirical model that describes the relation between  $\gamma$  and the correlation length ( $l_c$ ) and the shape parameter of the correlation function ( $m$ ) was described. This relation, as well as a lookup table for the  $m$ -dependent fitted parameters of the model, were incorporated into the MDSFR fitting routine, enabling not only determination of  $\mu'_s$  and  $\gamma$  but also of  $m$  and  $l_c$ . Values of  $\mu'_s$ ,  $\gamma$  and  $m$  were extracted with great accuracy. Estimates of  $l_c$ , however, showed increasing errors for large  $l_c$  values which is likely caused by the asymptotic behavior of the  $\gamma$  model.

## Samenvatting

Dit proefschrift presenteert de ontwikkeling van multi-diameter single fiber reflectance (MDSFR) spectroscopie, waarmee de kwantitatieve bepaling van twee weefselverstrooiingseigenschappen -de gereduceerde verstrooiingscoëfficiënt  $\mu'_s$  en een parameter gerelateerd aan de verstrooiingshoek  $\gamma$  - mogelijk gemaakt wordt.

In **Hoofdstuk 2** zijn Monte Carlo simulaties gebruikt om het verband tussen de single fiber reflectance (SFR) intensiteit, de fiberdiameter, de gereduceerde verstrooiingscoëfficiënt en de fasefunctie (PF) te onderzoeken. Gebaseerd op deze simulaties is een verband gevonden tussen het SFR signaal  $RSF$  en de dimensieloze gereduceerde verstrooiingscoëfficiënt. Het model is zowel in een gebied met lage verstrooiing waar het signaal PF-afhankelijk is, als in een PF-onafhankelijk gebied met hoge verstrooiing accuraat. Gebaseerd op dit PF-onafhankelijk gedrag voor hoge verstrooiing, hebben wij een solide optisch fantoom ontworpen voor kalibratie. Dit fantoom heeft een zeer hoge gereduceerde verstrooiingscoëfficiënt en kan gebruikt worden voor het absoluut kwantificeren van SFR metingen. Experimentele metingen op optische fantomen, met Intralipid als verstrooier, werden uitgevoerd met de nieuwe kalibratiemethode. Onze bevinding was dat  $\mu'_s$  accuraat gekwantificeerd kan worden door de experimentele data op het SFR model te fitten wanneer PF-afhankelijke modelparameters van Monte Carlo simulaties van SFR in Intralipid worden gebruikt.

In **Hoofdstuk 3** wordt het verband tussen de SFR-model parameters en de PF-afhankelijke parameter  $\gamma$  aangetoond. Daarnaast wordt het concept van MDSFR spectroscopie geïntroduceerd. We tonen aan dat meervoudige SFR metingen met verschillende fiberdiameters een accurate bepaling van  $\mu'_s$  en  $\gamma$  mogelijk maken. Hierbij wordt de data multidimensionaal gefit naar de curven van het SFR-model en de golflengteafhankelijkheid van de gereduceerde verstrooiingscoëfficiënt is gespecificeerd als  $\mu'_s = a\lambda^{-b}$ .

**Hoofdstuk 4** onderzoekt de sensitiviteit en de beperkingen van de MDSFR aanpak op een uitgebreide set Monte Carlo simulaties volgens de modified Henyey-Greenstein PF. Het wordt aangetoond dat de MDSFR aanpak goede resultaten geeft zelfs wanneer toegepast op een enkele golflengte, dat wil zeggen wanneer geen eerder verkregen gegevens over de spectrale afhankelijkheid van  $\mu'_s$  zijn verwerkt in de fitroutine. Deze methode echter, is alleen toepasbaar in golflengtegebieden waar weefselabsorptie zwak genoeg is om niet de reflectie-intensiteit te beïnvloeden. Het effect van het gebruik van verschillende diametercombinaties en het aantal fiberdiameters dat bijdraagt aan de MDSFR fit is onderzocht op gesimuleerde SFR data van zeven verschillende fiberdiameters tussen 0.2 mm en 1.5 mm. Zowel de enkele golflengte als de spectraal onderbouwde MDSFR analyse zijn onderzocht. Door alleen fiberdiameters van 0.2mm en 1.5 mm over

te houden en tussenliggende fiberdiameters te verwijderen wordt in beide gevallen aangetoond dat de MDSFR methode relatief ongevoelig is voor het beperken van het aantal verschillende fiberdiameters. Wanneer grote fiberdiameters verwijderd werden nam de foutmarge in de bepaling van  $\mu'_s$  en  $\gamma$  toe. Daarnaast werden lage  $\mu'_s$  waarden in het algemeen geschat met een hogere foutmarge (verstrooiingsset  $\mu'_s = 0.4\text{--}1\text{ mm}^{-1}$ ). Ten slotte is de nauwkeurigheid van de spectraal onderbouwde MDSFR analyse onderzocht door middel van het afbakenen van de dataset, zodat  $\gamma$  spectraal constant, spectraal afnemend of willekeurig over het golflengtegebied was. In alle drie de gevallen konden  $\mu'_s$  en  $\gamma$  goed geschat worden, waarmee is aangetoond dat de MDSFR methode onafhankelijk is van de spectrale afhankelijkheid van  $\gamma$ .

**Hoofdstuk 5** beschrijft de experimentele validatie van de MDSFR methode op een optisch fantoom dat polystyreenbolletjes in een fractale distributie bevat. De fractaldimensie is zo bepaald dat de resulterende PF, berekend met Mie theorie, een modified Henyey-Greenstein PF benadert. Een nieuwe kalibratiemethode wordt geïntroduceerd die de kalibratie op Spectralon en het vaste kalibratiefantoom met hoge verstrooiingscoëfficiënt vervangt. Deze nieuwe kalibratiemethode combineert de spectrale en de absolute kalibratie door het nemen van SFR-metingen op een optisch fantoom dat Intralipid bevat. De MDSFR methode is uitgevoerd op het fractalverstrooiingsfantoom dat polystyreenbolletjes bevat en  $\mu'_s$  en  $\gamma$  werden vastgesteld in afwezigheid van een absorber (Evans Blue).

**Hoofdstuk 6** presenteert de eerste *in vivo* MDSFR metingen op vier verschillende weefseltypen van muizen: huid, lever, normaal tongweefsel en een orthotopisch oraal plaveiselcelcarcinoom. Spectra werden genomen opeenvolgend met twee verschillende fiberdiameters ( $d_{fb} = 0.4, 0.8\text{ mm}$ ). De geëxtraheerde waarden voor  $\mu'_s$  voor de verschillende weefseltypen waren allen binnen het bereik van  $\mu'_s$  waarden gepubliceerd in de literatuur. Er werden significante verschillen in de verstrooiingspower en  $\mu'_s$  (800 nm) tussen de verschillende weefseltypen vastgesteld. De geëxtraheerde  $\gamma$  waarden voor alle weefseltypen lieten een continue toename per golflengte zien, waren binnen het bereik van verwachte waarden en lieten significante verschillen zien tussen de verschillende weefseltypen.

Uiteindelijk legt **Hoofdstuk 7** het verband tussen de optisch gemeten parameters  $\mu'_s$  en  $\gamma$  en weefseleigenschappen door weefsel te beschouwen als een medium met willekeurige en continue brekingsindex fluctuaties. Een PF die is afgeleid uit de Whittle-Matérn brekingsindex correlatie functie is gebruikt om SFR data te simuleren, die daarna geanalyseerd is door MDSFR. De MDSFR-fit geeft uitstekende resultaten in het bepalen van  $\gamma$  voor deze specifieke PF. Dit hoofdstuk beschrijft een empirisch model dat de relatie tussen  $\gamma$ , de correlatielengte  $l_c$  en de vormparameter van de correlatiefunctie  $m$  omschrijft. Dit verband is verwerkt in de MDSFR fitroutine, evenals als een overzichtstabel voor de

$m$ -afhankelijke aangepaste parameters van het model. Hierdoor is niet alleen bepaling van  $\mu'_s$  en  $\gamma$  mogelijk, maar ook die van  $m$  en  $l_c$ . De waardes van  $\mu'_s$ ,  $\gamma$  en  $m$  werden met grote nauwkeurigheid bepaald. Schattingen van  $l_c$  daarentegen lieten een afnemende nauwkeurigheid zien bij hoge  $l_c$  waardes, wat mogelijk veroorzaakt wordt door het asymptotisch gedrag van het  $\gamma$  model.







# Appendices

Acknowledgements

Curriculum vitae

List of publications

PhD Portfolio

# Acknowledgements

This thesis wouldn't have been possible without great collaborations and the support and guidance that I received from many people and therefore I would like to express my gratitude.

Arjen, you have been the greatest supervisor and without your guidance and your support I wouldn't have been able to write this thesis. You taught me everything about fiber optic spectroscopy and from the first day on, you involved me in all your projects which gave me a deeper insight into the scientific way of working and allowed me to reach the level at which I am now. I appreciate your encouragement and your cheerful way to always/constantly keeping me motivated.

Dick, you warmly welcomed me in this group and always supported me throughout the years. I greatly appreciate that you were always approachable to discuss science, answer questions and open to share a part of your wisdom with me. I am honored that I was allowed to work in your group.

Chad, you taught me everything about Monte Carlo simulations, and wrote the MC code, which a large part of this thesis is based upon. I also would like to thank you for motivating and helping me when my mind got stuck between phase functions and 5 dimensional matrices.

Floor, you were my "partner in crime"; together we went through the ups and downs of being a PhD student. Thank you for the great collaboration in our shared projects, for helping sorting things out when I arrived and letting me "live" in your house, for enlightening me with your Matlab skills, for practicing Dutch with me, for motivating me with your "yes, we can"-attitude and for being a great friend.

Dom, on your way to discuss things with Floor, you often stopped at my desk and asked me how things are going. You were always open to give advice and help me out with our experiments. Thank you!

Chris, I am deeply grateful that you helped me so much in the last weeks to finish the latest chapters of this thesis. Besides that you were always open to discuss our projects and you gave me great advice during my search for a post-doc position.

Riëtte and Angelique, thank you for being so supportive in all lab-related issues, for showing me how to set up animal studies and for carrying out all the animal work.

I would also like to thank current and former members of the CODT group, Giju, Jan Bonne, Slavka, Bastiaan, Robert, Sander, Zoe and Threes thank you for supportive words, good advices and interesting conversations as well as my B.S. students Matthijs and Laury for their good work.

Michiel and Cees from the department of Experimentele Medische Instrumentatie (EMI), thank you for designing and building the measurement units and customized equipment.

I also appreciated being part time hired by Luminostix; Wouter, thank you for all your support and interesting lunch conversations. Theo, it was a lot of fun to work with you.

I would like to thank IOP photonics devices for funding this research and the partners of the HYMPACT project, Srirang, Michelle, Daniele, Wenfeng and Frank for the productive meetings and interesting conversations. Especially I would like to thank Michelle and Frank for making it possible to include MDSFR measurements into the PAM study and enable our first *in vivo* clinical measurements on breast tissue; which unfortunately could not be part of this thesis.

Meine lieben Eltern, natürlich geht der größte Dank an euch. Ohne eure Unterstützung und Förderung hätte ich niemals diesen Punkt erreicht und dafür möchte ich euch danken. Ihr seid immer für mich da bei größeren und kleineren Problemen und auch wenn die räumliche Distanz zwischen uns immer größer zu werden scheint sollt ihr wissen dass ihr immer in meinen Gedanken seid. Ulrich, Hans Georg und Tine, Ihr habt mich auch immer unterstützt, meine Zweifel zerschlagen und aufgemuntert wenn ich traurig war. Ich bin so froh dass ich so tolle Geschwister habe.

Finally I would like to express my gratitude to the friends I made here in Rotterdam who made my stay in the Netherlands a unique experience. Leonie, Katharina & Katha, Anne, Carol, Anne Elise, Amber and Ragnar, thank you for the good times; may there be yet more to come!

## Curriculum vitae

Ute Alice Gamm was born on June 5th, 1983 in Ludwigshafen am Rhein in Germany. She received her diploma from the Karolinen Gymnasium Frankenthal in 2002 and then decided to study Biophysics at the Technical University of Kaiserslautern, which she started the same year. In 2006, she spent a semester in Tenerife, Spain through the European student exchange program (Erasmus). There she attended courses in Physics and focused on learning Spanish. After returning to Germany, she specialized in Physics and Biomedical Sciences, later joining the Lasers in Medicine research group of Dr. Foth in the Department of Biophysics and Medical Physics to work on her graduation project. The project investigated the feasibility of inactivating bacteria through photodynamic therapy (PDT). She studied pharmacokinetics and pharmacodynamics of two photosensitizers (Chlorin e6 and Aminolevulinic acid (ALA)) on two strands of mycobacteria. Furthermore she monitored oxygen depletion and singlet oxygen generation during laser excitation of the photosensitizers. After receiving her Diploma in Biophysics in September 2008, she was welcomed as a PhD student by Prof. H.J.C. M. Sterenborg at the Center for Optical Diagnostics and Therapy at the Erasmus University Medical Center in Rotterdam in May 2009. Under guidance of Dr. A. Amelink, she contributed to the development of multi-diameter single fiber reflectance spectroscopy, which enables the quantification of tissue scattering properties and is the topic of this thesis. She also carried out clinical measurements of the scattering properties of healthy and malignant breast tissues. Furthermore she was involved in the development of a method that allows the quantification of the intrinsic fluorescence and the fluorescence quantum yield by use of fiber optic spectroscopy.

# List of publications

## Peer reviewed publications

1. U. A. Gamm, C. L. Hoy, H. J. C. M. Sterenborg, D. J. Robinson, A. Amelink, Measurement of refractive index correlation function properties using fiber-optic reflectance spectroscopy: *in silico* proof of concept, to be submitted to Biomed. Opt. Expr, 2013
2. C. Hoy, U. A. Gamm, H. J. C. M. Sterenborg, D. J. Robinson, A. Amelink, Method for rapid multi-diameter single fiber reflectance and fluorescence spectroscopy through a fiber bundle, in press, J. Biomed. Opt., 2013
3. U. A. Gamm, F. v. Leeuwen v. Zaane, S. C. Kanick, H. J. C. M. Sterenborg, D. J. Robinson, A. Amelink. Fully quantitative intrinsic single fiber fluorescence spectroscopy, to be submitted to Biomed. Opt. Expr, 2013.
4. F. van Leeuwen van Zaane, U.A. Gamm, P.B.A.A. van Driel, T.J.A. Snoeks, H.S. de Bruijn, A. van der Ploeg van den Heuvel, I.M. Mol, C.W.G.M. Lwik, H.J.C.M. Sterenborg, A. Amelink, D.J. Robinson, *In vivo* quantification of the scattering properties of tissue using multi-diameter single fiber reflectance spectroscopy, Biomed Opt Exp, 4: 696708 (2013).
5. U. A. Gamm, S. C. Kanick, H. J. C. M. Sterenborg, D. J. Robinson, A. Amelink, Quantification of the reduced scattering coefficient and phase-function-dependent parameter  $\gamma$  of turbid media using multidiameter single fiber reflectance spectroscopy: experimental validation, Opt Lett., 37:1838-1840 (2012).
6. C. Hoy, U. A. Gamm, H. J. C. M. Sterenborg, D. J. Robinson, A. Amelink, Use of a coherent fiber bundle for multidiameter single fiber reflectance spectroscopy, Biomed Opt Exp., 3:2452-2464 (2012).
7. S. C. Kanick, V. Krishnaswamy, U. A. Gamm, H. J. C. M. Sterenborg, D. J. Robinson, A. Amelink, B. Pogue, Scattering phase function spectrum makes reflectance spectrum measured from Intralipid phantoms and tissue sensitive to the device detection geometry, Biomed Opt Exp., 3:1086-1100 (2012).
8. U. A. Gamm, S. C. Kanick, H. J. C. M. Sterenborg, D. J. Robinson, A. Amelink, Measurement of tissue scattering properties using multi-diameter single fiber reflectance spectroscopy: *in silico* sensitivity analysis, Biomed Opt Exp., Vol. 2:3150-3166 (2011), Biomed Opt Exp., Vol. 2:31503166 (2011) .
9. S. C. Kanick, U. A. Gamm, H. J. C. M. Sterenborg, D. J. Robinson, A. Amelink, Method to quantitatively estimate wavelength-dependent scattering properties from multi-diameter single fiber reflectance spectra measured in a turbid medium, Opt Lett. 36:2997-2999 (2011).

10. U. A. Gamm\*, S. C. Kanick\*, H. J. C. M. Sterenborg, D. J. Robinson, A. Amelink. Measurement of the reduced scattering coefficient of turbid media using single fiber reflectance spectroscopy: fiber diameter and phase function dependence. Biomed Opt Exp. 2:1687-1702 (2011) \* indicates both authors contributed equally.

### Conference proceedings

1. U. A. Gamm, M. Heijblom, D. Piras, F. Van den Engh, S. Manohar, H. J. C. M. Sterenborg, D. J. Robinson, A. Amelink. *In vivo* determination of scattering properties of healthy and malignant breast tissue by use of multi-diametersingle fiber reflectance spectroscopy (MDSFR). Proceedings of SPIE Photonics West BiOS (2013), paper: 8592-29.
2. U. A. Gamm, S. C. Kanick, D. J. Robinson, H. J. C. M. Sterenborg, A. Amelink, Measurements of tissue scattering properties using mulit-diameter single fiber reflectance spectroscopy: experimental validation, Proceedings of OSA Biomedical (BIOMED) conference (2012), paper: BW2B.5
3. R. Bruce-Micah, U. A. Gamm, D. Hüttenberger, J. Cullum, H.-J. Foth, Photodynamic inactivation of the models *Mycobacterium phlei* and *Mycobacterium smegmatis* in vitro, Proceedings of SPIE-OSA Biomedical Optics (ECBO) paper: 73731L (2009).



# PhD Portfolio

Name PhD student: U.A. Gamm  
 Erasmus MC department: Center for Optical Diagnostics and Therapy  
 Research School: Postgraduate School Molecular Medicine  
 PhD period: 2009-2013  
 Promotor: Prof. H.J.M.C. Sterenborg  
 Copromotor: Dr. A. Amelink

## PhD Training

### *Courses*

Basic and translational Oncology 2009  
 Animal Imaging Workshop by AMIE 2010  
 Biomedical English Writing and Communication 2010  
 Basiscursus Regelgeving en Organisatie (BROK) 2011  
 Biophotonics 11, Summer school in Ven, Sweden 2011  
 Workshop on Photoshop and Illustrator CS5 2012

### *Seminars and research meetings*

Department research meetings	oral presentations	2009-2013
HYMPACT-Project meetings	oral presentations	2009-2013
MolMedDay 2010	poster presentation	2010
Symposium Sound light	oral presentation	2011
IOP Project afternoon	poster presentation	2011
Biophotonics 11, Summer school in Ven, Sweden	poster presentation	2011
Annual Dutch Meeting on Molecular and Cellular		2012
Biophysics 2012		

***International conferences***

ECBO, Munich, Germany		2009
ECl conference, Naples Florida USA	poster presentation	2011
BIOMED conference, Miami, Florida, USA	oral presentation	2012
Gordon Conference, Holderness, New Hampshire, USA	poster presentation	2012
SPIE, Photonics West, San Francisco, California, USA	oral presentation	2013
ECBO Conference, Munich, Germany	oral presentation	2013

***Teaching***

Supervision of bachelor student in physics	2010
Supervision of bachelor student in physics	2011
Support of guest PhD student	2011